

**Study on Advanced Electrode Materials with  
Graphene-based Composites**

Zhang Feifei

February 2014

Study on Advanced Electrode Materials with  
Graphene-based Composites

Zhang Feifei

Doctoral Program in Materials Science and Engineering

Submitted to the Graduate School of  
Pure and Applied Sciences  
in Partial Fulfillment of the Requirements  
for the Degree of Doctor of Philosophy in  
Engineering

at the  
University of Tsukuba

# Abstract

## Hybrid Graphene Electrodes for Supercapacitors of High Energy Density

Supercapacitors have attracted significant attention recently due to their extraordinary high power density and long cycle life. They also bridge the power and energy gaps between traditional dielectric capacitors (which have high power output but low energy density) and batteries (which have high energy density but low power density). A major challenge for the development of supercapacitors has been to improve their energy density. Supercapacitor study is enhanced by modern graphene based materials. The object of this study is using three dimensional nano-architecture materials to increase the specific capacitance and electrolyte accessibility and usage of ionic liquid electrolyte at high voltage further improve the energy density.

We have studied a novel graphene based hybrid electrode for supercapacitors, and developed a process of co-reduction to reduce mono-dispersed graphene oxide (GO) and single-walled carbon nanotubes (SWNTs) simultaneously, with aid of surfactant functionalization. The role of SWNTs is figured out to be in between the inter-layer space of graphene sheets as a spacer to prevent effectively restacking of graphene that often limits seriously the electrochemical performance of graphene supercapacitors, and also act as conductive binders to improve the electrical conduction of the electrode. The effect of functional groups and structure defects in graphene based supercapacitor is also studied. A high specific capacitance of  $261 \text{ F g}^{-1}$  for a single electrode and specific energy density of  $123 \text{ Wh kg}^{-1}$  in the two-electrode configuration have been obtained in ionic liquid (EMI-TFSI) electrolyte.

## Graphene-based Composites Modified Electrodes for Biosensing

The outstanding sensing properties of graphene based materials are mainly attributed to the presence of more  $sp^2$ -like planes and various edge defects present on the surface and edge of graphene. More importantly, with their three-dimensional nanostructures and adjustable surface chemistry, graphene based composites can interact strongly with other organic and/or inorganic systems with combination and synergistic effects of different components. Hydrothermal synthesis is an efficient and non-toxic method for production of graphene without using any chemical reagents or catalysts. One feasible proposal has been to use spacers to avoid or reduce the restacking and agglomeration of graphene. On the other hand, it would apparently be a better choice if the selected spacers could also contribute to the specific surface area, stability, and reactivity of the electrode material and structure.

In this work, two kinds of graphene-based composites were developed through a hydrothermal reduction process: graphene-carbon nanotube composite aerogel composite (hydrothermal G/S) and  $\alpha$ - $\text{MnO}_2$  nanorods/graphene composite ( $\text{MnO}_2$  NR/RGO), and applied to the selective detection of uric acid.

- We studied the mechanism and processing of graphene and single-walled carbon nanotubes (SWNTs) composite by a hydrothermal method, where the SWNTs are covalently connected with graphene and also inserted into the interlayer space between graphene sheets to reduce restacking of graphene. The hydrothermally synthesized graphene and carbon nanotube composite aerogel has also been developed as a modified electrode for selective detection of UA.

- Manganese oxide is a kind of attractive inorganic material in biosensing application, due to their excellent catalytic oxidation abilities. A novel  $\alpha$ -MnO<sub>2</sub> nanorods (MnO<sub>2</sub> NR) and graphene composite modified electrode was fabricated for the selective detection of uric acid (UA). The mechanism of eliminating effect of MnO<sub>2</sub> to interferences (ascorbic acid) was also studied. The composite were prepared by incorporating MnO<sub>2</sub> nanoparticles, which were synthesized by hydrothermal method, onto the basal plane of reduced graphene oxide (RGO) with the aid of ultrasonication to obtain a composite.

### **Electrochemistry of HOPG Electrodes: Edge and Basal Plane Effect for Supercapacitor and Biosensing**

The molecular engineering of an electrode surface is of paramount importance for the development of electrochemical devices with region-specific electron-transfer capabilities. As it has a unique two-dimensional molecular geometry and excellent electronic properties, graphene has been widely used as functional electrodes in various electrochemical systems, such as chemical sensors, biosensors and supercapacitors. There are many researches demonstrated that the large capacitances achieved demand not only to a larger surface area but also the pore structure or surface chemistry plays a role. In the meanwhile, some studies have suggested that much of the enhanced electrochemical activity and electron-transfer rate at graphene electrodes arises from the surface defects and functional groups load on the basal plane and edge. These situations were further complicated by oxygen-containing groups, often introduced through chemical/electrochemical oxidation of the graphene, which could affect the absorption and reactive kinetics.

In this work, we studied the electrochemistry of the highly oriented pyrolytic graphite (HOPG) basal plane and edge electrodes specifically, by selectively masking regions of HOPG with a nonconducting polymer coating such that the electrolyte has access the basal plane and edge only, described as HOPG-P and HOPG-E electrodes. Depending on the electrochemical species (H<sub>2</sub>SO<sub>4</sub>, Fe<sup>3+</sup>, UA and AA) used we found out that the HOPG basal plane and edge carbon atoms could play a different role in electrochemistry. Furthermore, oxygen-containing surface functionalities induced by electrochemical oxidation, were also demonstrated to regulate electrochemical activities of the HOPG electrode. As all graphite electrodes are made from essentially the same building blocks (graphene sheets) we can expand our conclusions to other carbon materials even nanomaterials such as graphene, carbon fibers, and even carbon nanotubes. And the results should facilitate the design and development of novel graphene-based electrodes of practical significance, especially in the development of supercapacitors and biosensors.

# Content

<b>Abstract</b> .....	I
<b>Chapter 1</b>	
<b>Introduction</b> .....	1
1.1 Properties and Preparation of Graphene.....	1
1.2 Applications of Graphene in Electrochemistry.....	3
1.3 Graphene for Supercapacitor.....	4
1.3.1 Principle of Supercapacitor.....	4
1.3.2 Electrolytes.....	8
1.3.3 Graphene-based Composites as Supercapacitor Electrodes.....	9
1.3.4 Other Carbon Materials.....	11
1.4 Applications of Graphene in Electrochemical Sensors and Biosensors.....	14
1.5 Motivation and Objective.....	16
References.....	17
<b>Chapter 2</b>	
<b>Experimental Technique</b> .....	24
2.1 Electrochemical Methods.....	24
2.1.1 Cyclic Voltammetry.....	24
2.1.2 Constant Current Charge and Discharge.....	26
2.1.3 Electrochemical Impedance Spectroscopy.....	26
2.2 Test Cell Configuration.....	26
2.3 Measurement Procedure.....	27
2.4 Summary of Test Method.....	27
References.....	28
<b>Chapter 3</b>	
<b>Hybrid Graphene Electrodes for Supercapacitors of High Energy Density</b> .....	29
3.1 Introduction.....	29
3.2 Experimental.....	31

3.2.1 Preparation of Co-Reduced SWNT/GO Composites.....	31
3.2.2 Materials Characterization.....	32
3.2.3 Structure and Evaluation of Graphene Supercapacitor.....	32
3.3 Results and Discussion.....	32
3.4 Conclusions.....	40
References.....	40

## Chapter 4

<b>Graphene-Carbon Nanotube Composite Aerogel for Selective Detection of Uric Acid.....</b>	<b>42</b>
4.1 Introduction.....	42
4.2 Experimental.....	43
4.2.1 Hydrothermal Synthesis of Graphene/SWNT Composite.....	43
4.2.2 Characterization.....	44
4.2.3 Electrochemical Measurements.....	44
4.3 Results and Discussion.....	44
4.4 Conclusions.....	49
References.....	49

## Chapter 5

<b>Elimination of Ascorbic Acid and Sensitive Detection of Uric Acid at the MnO<sub>2</sub> Nanorods /Graphene-based Modified Electrode.....</b>	<b>52</b>
5.1 Introduction.....	52
5.2 Experimental.....	53
5.2.1 Reagents and Apparatus.....	54
5.2.2 Synthesis of Reduced Graphene Oxide (RGO).....	54
5.2.3 Fabrication of Modified Electrode.....	54
5.2.4 Electrochemical Measurement.....	55
5.3 Results and Discussion.....	55
5.3.1 Characterization of RGO, MnO <sub>2</sub> NR and MnO <sub>2</sub> NR/RGO Composite.....	55
5.3.2 Electrochemical Behaviors of the MnO <sub>2</sub> NR/RGO Modified Electrodes.....	56
5.3.3 UA Electrochemical Detection Performance on the MnO <sub>2</sub> NR/RGO/GCE.....	58
5.3.4 Analysis of Human Urine Samples.....	58
5.4 Conclusions.....	59

References.....	59
-----------------	----

## **Chapter 6**

<b>Electrochemistry of HOPG Electrodes: Edge and Basal Plane Effect for Supercapacitor and Biosensing.....</b>	<b>62</b>
6.1 Introduction.....	62
6.2 Experimental.....	63
6.2.1 Fabrication of HOPG Edge (HOPG-E) and Basal Plane Electrodes (HOPG-P).....	63
6.2.2 Electrochemical Oxidation of HOPG Edge and Plane Electrodes.....	64
6.2.3 Structural and Electrochemical Characterization.....	64
6.3 Results and Discussion.....	65
6.3.1 Characterizations.....	65
6.3.2 Edge and Basal Plane Effect of HOPG for Supercapacitor.....	71
6.3.3 Edge and Basal Plane Effect of HOPG for Biosensing.....	75
6.4 Conclusions.....	78
References.....	79

## **Chapter 7**

<b>Conclusions and Perspective.....</b>	<b>82</b>
7.1 Conclusions.....	82
7.2 Future Prospects.....	85

## **Chapter 8**

<b>Achievements.....</b>	<b>87</b>
8.1 List of Publications.....	87
8.2 Award.....	87
8.3 Patents.....	87
8.4 Oral Presentation.....	88

<b>Acknowledgements.....</b>	<b>89</b>
------------------------------	-----------

---

# Chapter 1

## Introduction

---

### 1.1 Properties and Preparation of Graphene

Graphene is a one-atom thick layer of the layered mineral graphite with a carbon-carbon bond length of 0.142 nm, in which a two-dimensional (2D) layer of carbon atoms ordered into a honeycomb lattice, and is essentially a very large polyaromatic hydrocarbon.[1-5] Graphene is a basic building block for graphitic materials of all other dimensionalities (Figure 1-1). It can be wrapped up into 0D fullerenes, rolled into 1D nanotubes or stacked into 3D graphite.[6] Since the direct investigation of mechanically exfoliated graphene by Novoselov et al. in 2004 [7], tremendous research efforts have been devoted to the study and applications of graphene as well as graphene-based materials.[8-11] Graphene is a zero-gap semimetal with a small overlap between its valence and conduction bands. It shows a strong ambipolar electric field effect with the high charge carrier mobilities of  $\approx 10\,000\text{ cm}^2\text{ V}^{-1}\text{ s}^{-1}$  at room temperature.[7]

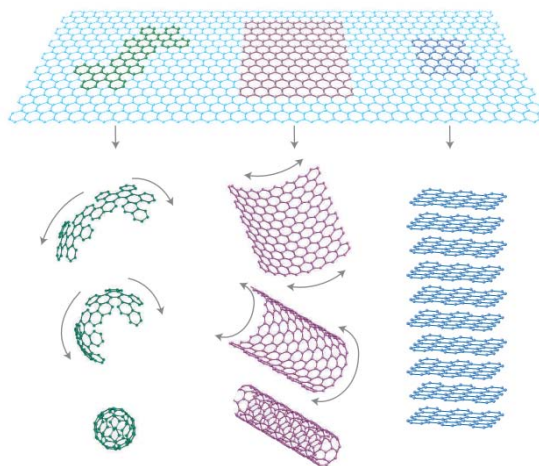


**Figure 1-1** Mother of all graphitic forms. Graphene is a 2D building material for carbon materials of all other dimensionalities. It can be wrapped up into 0D buckyballs, rolled into 1D nanotubes or stacked into 3D graphite.[6]

The suspended graphene reported to exhibits a mobility approaching  $20\,000\text{ cm}^2\text{ V}^{-1}\text{ s}^{-1}$  for the carrier density below  $5 \times 10^9\text{ cm}^{-2}$  at a low temperature.[12] In addition, the white light absorbance of a suspended graphene monolayer is 2.3% (or transmittance of 97.7%) with a negligible reflectance of  $< 0.1\%$ .[13] Moreover graphene exhibits the excellent thermal stability and conductivity ( $3000 \approx 5000\text{ W m}^{-1}\text{ K}^{-1}$ ),[14] high Young's modulus (1 TPa), [15] and large theoretical specific surface area (SSA,  $2630\text{ m}^2\text{ g}^{-1}$ ).[16] All these outstanding properties have thus aroused great research interest from the fundamental study to various applications of graphene in electronics,[17] transparent conducting electrodes,[18, 19] energy storage[20-23]

and biodevices,[24-26] et al. Moreover, only monolayer graphene and, to a good approximation, its bilayer has simple electronic spectra: they are both zero-gap semiconductors with one type of electron and one type of hole. And in three or more layers graphene, the spectra become increasingly complicated for example several charge carriers appear, start notably overlapping and the conduction and valence bands.[6, 27, 28] As the electronic structure of graphene sheet is closely related the number of layers, single-, double- and few- (3 to <10) layer graphene can be distinguished as three different types of 2D crystals ('graphenes'), and thicker structures (over 10) should be considered, to all intents and purposes, as thin films of graphite.

Numerous methods have been employed for synthesis of graphene, such as the dry mechanical exfoliation method[7] (or the "scotch tape" method), thermal decomposition of SiC,[29] chemical vapor deposition (CVD),[30, 31] the exfoliation and reduction of chemically oxidized graphite,[32] exfoliation of graphite and graphite intercalated compounds,[33] solvothermal synthesis,[34] the unzipping of CNTs[35, 36] and so on. Dry mechanical exfoliation has ability to yield the high quality single- and few-layer graphene sheets, suited ideally for the investigation of graphene's physical properties, but is difficult to massively produce graphene for the practical application. The CVD method, on the other hand, has been recognized as one of the most promising processes to reliably generate high-quality graphene films, particularly used for electronic and optoelectronic devices. Since Kong et al. reported the CVD growth of few-layer graphene films on the polycrystalline Ni substrate in 2008,[37] tremendous efforts have been made to produce the uniform graphene films with controllable layer number and minimized defects. For example, Li et al. successfully demonstrated the growth of large-area, monolayer graphene single crystals were grown by low-pressure chemical vapor deposition in copper foil enclosures using methane as a precursor with dimensions of up to 0.5 mm on a side.[38] Recently, the further development in CVD growth of graphene has been achieved, including the near room temperature (25-160°C) synthesis of graphene films on the nonconducting substrates,[31] The of millimeter-size single crystal graphene grains was synthesis on the noble metals substrate,[39, 40] and the growth of strictly single-layer graphene on the Ni-Mo alloy with 100% surface coverage.[41] All these advances are expected to enable more possibilities for use of CVD- graphene in various electronic and optoelectronic applications.

Because of the relatively high cost and low throughput of the CVD process, the large-quantity fabrication of graphene and its derivatives from the bulk graphite has also been subject to intensive investigation for their potential applications in touch screens, energy storage devices, electrochemical sensors, fuel cells and so on, where the extremely high conductivity of graphene film is not required. Thermal exfoliation has proven to be a very efficient method for the preparation of graphene.[42-45] Although the sheets produced by thermal exfoliation of graphite oxide exhibit a wrinkled and defective structure, this process allows recovering some of the electrical conductivity lost by oxidation. Various heating sources, temperatures and assistive strategies have been employed, leading to great variance in the degree of exfoliation between methods. The exfoliation of expanded graphite and graphite intercalation compounds, which yielded high quality graphene sheets with ordered and defect free structures promising[33]

Intercalation techniques have been widely combined with thermal treatments and have proven effective in increasing exfoliation yields.

In the meanwhile, an alternative strategy, probably one of the mostly explored and applied methods, is the reduction of highly oxidized graphene oxide (GO) sheets from the exfoliated graphite oxide, to yield the reduced GO (rGO), functionalized graphene sheets (FGSs) or the chemically converted graphene (CCG).[32] The graphite oxide is obtained based on the Hummers method by reacting graphite with potassium permanganate ( $\text{KMnO}_4$ ) and concentrated sulfuric acid ( $\text{H}_2\text{SO}_4$ ).[46-48] Hence, the GO sheets are highly oxidized with abundant residual epoxide, carbonyl, hydroxide and carboxylic acid groups anchoring on their surface. [32] Until now, many reduction methods have been reported to obtain rGO sheets, such as the chemical reagent reduction, thermal reduction, photochemical reduction, photothermal reduction, microwave-assisted reduction and electrochemical reduction. [32] Recently, a KOH-activated method has also been applied to prepare graphene from thermal-exfoliated graphite oxide (TEGO) and microwave-exfoliated graphite oxide (MEGO), which gives rise to a porous graphene network containing mostly single layers of  $\text{sp}^2$ -bonded carbon, together with an ultrahigh specific surface area up to  $3100 \text{ m}^2 \text{ g}^{-1}$ . [49] This type of porous graphene-based material is ready for fabrication of electrodes used for high-performance energy storage devices. And a fascinating laser reduced graphene oxide supercapacitor electrodes were made by a standard DVD writer. The electrodes are composed of an expanded network of graphene that shows excellent mechanical and electrical properties (10-100 times that of activated carbon and previous graphene electrodes) as well as exceptionally high surface area of 1,520 square meters per gram - about a third of an acre, and 3-5 times the surface area of activated carbon electrodes.[20]

## 1.2 Applications of Graphene in Electrochemistry

Carbon materials have been widely utilized in both analytical and industrial electrochemistry, where in many areas they have out-performed the traditional noble metals. This diversity and success stems largely from carbons structural polymorphism, chemical stability, low cost, wide potential windows, relatively inert electrochemistry, rich surface chemistry and electro-catalytic activities for a variety of redox reactions.[1] Most recently though the classical carbon materials based on graphite, glassy carbon, diamond and carbon black have been outperformed by the distinctive properties of micro-fabricated carbon structures, such as CNTs, enabling novel applications in sensing, electro-catalysis, and electronics. Until now CNTs have fore-fronted innovation and dominated the field, however, with the introduction of graphene, which is reported to offer more advanced properties and is likely to exhibit fewer of the weaknesses that plagued CNTs, enormous progress in this field is underway, led mainly because the relevant research concerning graphene can be built on the wealth of techniques and knowledge available from decades of research on graphite and CNTs, where it can possibly outperform them at each opportunity.[1] Due to graphene's unique properties it has been speculated that graphene can carry a super-current,[50] and it is clear that its rates are superior to that of graphite and CNTs. The fast charge carrier properties of graphene were found not only to

be continuous, but to exhibit high crystal quality, in which importantly for graphene charge carriers can travel thousands of inter-atomic distances without scattering. These isolated graphene crystallites demonstrate exceptional electronic qualities, and graphene has exhibited the fastest electron mobilities when compared to all other possible materials, ‘theoretically’ meaning that in many applications graphene based electrodes react much faster.[2]

## 1.3 Graphene for Supercapacitor

### 1.3.1 Principle of Supercapacitor

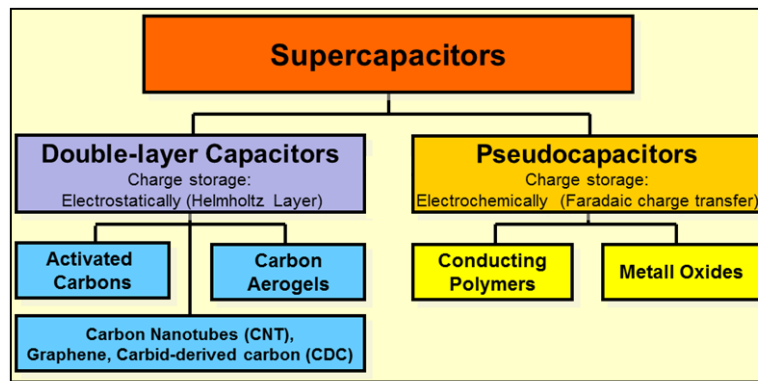


**Figure 1-2** Classification of supercapacitor

The capacitance of the majority of capacitors used in electronic circuits is generally several orders of magnitude smaller than the farad. However, specially made supercapacitors can be much larger (as much as hundreds of farads), and parasitic capacitive elements can be less than a femtofarad. Capacitance can be calculated if the geometry of the conductors and the dielectric properties of the insulator between the conductors are known. For example, the capacitance of a parallel-plate capacitor constructed of two parallel plates both of area  $A$  separated by a distance  $d$  is approximately equal to the following:

$$C = \frac{\epsilon_r \epsilon_0 A}{d} \quad (1-1)$$

where  $C$  is the capacitance, in Farads;  $A$  is the area of overlap of the two plates, in square meters;  $\epsilon_r$  is the relative static permittivity (sometimes called the dielectric constant) of the material between the plates (for a vacuum,  $\epsilon_r = 1$ );  $\epsilon_0$  is the electric constant ( $\epsilon_0 \approx 8.854 \times 10^{-12}$  F/m); and  $d$  is the separation between the plates, in meters;

Supercapacitor can be divided into two categories based on the energy storage mechanism (Figure 1-2). One kind is electrochemical double-layer capacitor (EDLC). Supercapacitor based on electrochemical double layer capacitance (EDLC) are electrical energy storage devices that store and release energy by nanoscopic

charge separation at the electrochemical interface between an electrode and an electrolyte. While the charge storage mechanism of EDLCs is based on the interfacial double-layer of high specific area carbons, another class of capacitors is based on pseudocapacitance, and thus associated with electrosorption and surface redox processes at high surface area electrode materials such as metal oxides and conducting polymers. The principles of the two types of supercapacitor will be discussed in detail below.

### Electrochemical double-layer capacitor (EDLC)

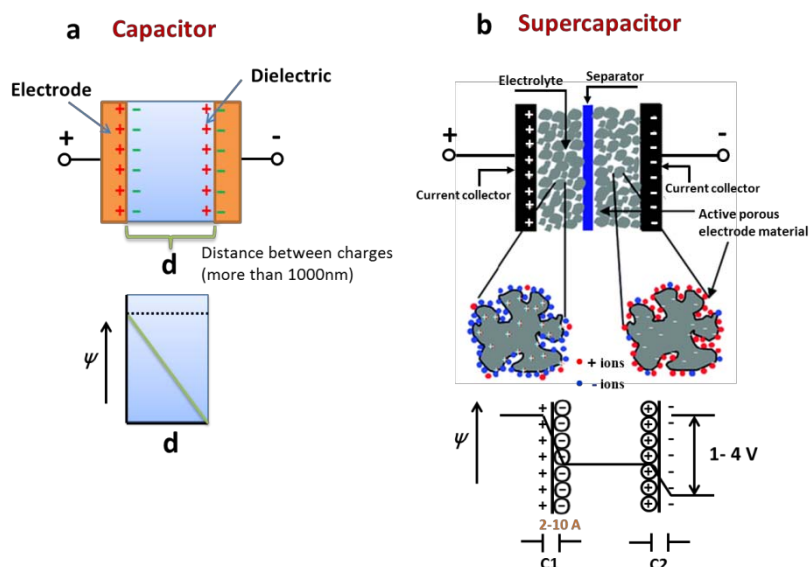


**Figure 1-3** Comparison of construction diagrams of the capacitors of (a) conventional capacitor and (b) supercapacitor

EDLC is a kind of electrochemical capacitors that store charges electrostatically using reversible adsorption of ions of the electrolyte onto active materials that are electrochemically stable and have a high accessible surface area.[51] There are some modes to describe the electrochemical double-layer. A comparison of construction of conventional capacitor and supercapacitor is shown in [Figure 1-3](#).

### Helmholtz Model

Helmholtz model of electrochemical double-layer (DL) was firstly proposed by Helmholtz in 1853. In his model, Helmholtz treated the DL mathematically as a simple capacitor, based on a physical model in which a single layer of ions is adsorbed at the surface.[52]

### Gouy-Chapman Model

Later Louis Georges Gouy[53, 54] and David Chapman[55] introduced a diffuse model of the electrical DL, in which the electric potential decreases exponentially away from the surface to the fluid bulk due to the thermal motion of ions. The capacitance was not a constant and that it depended on the applied potential and the ionic concentration. To formulate this model the Poisson equation was used to relate potential to charge

density, and Boltzmann equation was used to determine the distribution of ions. Gouy's theory results in a differential capacitance described by [Equation 1-2](#).

$$C_G = \frac{\varepsilon k}{4\pi} \cos \frac{z}{2} \quad (1-2)$$

Where  $z$  is the valence of the ions and  $\kappa$  is the reciprocal Debye-Hückel equation length defined by [Equation 1-3](#).

$$k = \sqrt{\frac{8\pi n e^2 z^2}{\varepsilon k T}} \quad (1-3)$$

$n$  is the number of ions per cubic centimeter,  $T$  is the absolute temperature, and  $k$  is the Boltzmann constant. The capacitance  $C_G$  resulting from the diffuse charge distribution is therefore no longer a constant. This model was also worked on by D.C. Chapman, and also referred to as the Gouy-Chapman model.

### Stern and Grahame Model

Gouy-Chapman model fails for highly charged DLs and treats the adsorbed ions as mobile. In order to resolve this problem Otto Stern in 1924 suggested the combination of the Helmholtz and Gouy-Chapman models. In Stern's model, some of the ions adhere to the electrode as suggested by Helmholtz, giving an internal Stern layer and some form a Gouy-Chapman diffuse layer.[\[56\]](#) The Stern layer accounted for ions' finite size and consequently ions have a closest approach to the electrode on the order of the ionic radius. The Stern model too had limitations, effectively modeling ions as point charges, assuming all significant interactions in the diffuse layer are Coulombic, assuming dielectric permittivity to be constant throughout the double layer, and that fluid viscosity is constant above the slipping plane.[\[57\]](#) Thus, D. C. Grahame modified Stern in 1947. [\[58\]](#) He proposed that some ionic or uncharged species can penetrate the Stern layer, although the closest approach to the electrode is normally occupied by solvent molecules. This could occur if ions lost their solvation shell when the ion approached the electrode. Ions in direct contact with the electrode were called "specifically adsorbed ions". This model proposed the existence of three regions. The inner Helmholtz plane (IHP) passing through the centers of the specifically adsorbed ions. The outer Helmholtz plane (OHP) passes through the centres of solvated ions at their distance of closest approach to the electrode. Finally the diffuse layer is the region beyond the OHP. The three models were summarized in [Figure 1-4](#).

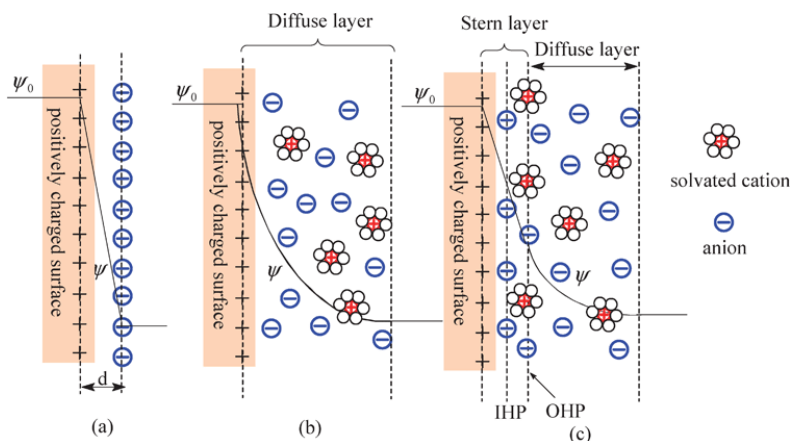


**Figure 1-4** Models of the electrical double layer at a positively charged surface: (a) the Helmholtz model, (b) the Gouy–Chapman model, and (c) the Stern model, showing the inner Helmholtz plane (IHP) and outer Helmholtz plane (OHP). The IHP refers to the distance of closest approach of specifically adsorbed ions (generally anions) and OHP refers to that of the non-specifically adsorbed ions. The OHP is also the plane where the diffuse layer begins.  $d$  is the double layer distance described by the Helmholtz model.  $\Psi_0$  and  $\Psi$  are the potentials at the electrode surface and the electrode/electrolyte interface, respectively.

The capacitance in the EDL ( $C_{dl}$ ) can be treated as a combination of the capacitances from two regions, the Stern type of compact double layer capacitance ( $C_H$ ) and the diffusion region capacitance ( $C_{diff}$ ). Thus,  $C_{dl}$  can be expressed by Equation 1-4:

$$\frac{1}{C_{dl}} = \frac{1}{C_H} + \frac{1}{C_{diff}} \quad (1-4)$$

Equation 1-4 becomes invalid if specific adsorption of ions occurs, however, and if this is the case, the capacitance is equated by Equation 1-5:

$$\frac{1}{C_{dl}} = \frac{1}{C_H} + \frac{1}{C_{diff}} \left(1 + \frac{\partial \sigma_A}{\partial \sigma}\right) \quad (1-5)$$

$\sigma$  is charge density on the electrode, and  $\sigma_A$  is the surface charge of the adsorbed ions. This model has not been significantly improved upon since its formulation, but any capacitive effects that may result from dipoles interacting with the charged electrode surface are not considered in the model.

### Pseudo-capacitance

Pseudo-capacitance arises for thermodynamics reasons and is due to charge acceptance ( $\Delta q$ ) and a change in potential ( $\Delta V$ ). The derivative  $C = d(\Delta q)/d(\Delta V)$  corresponds to a capacitance, which is referred to as the pseudo-capacitance. Three types of faradaic processes occur at FS electrodes: reversible adsorption (for example, adsorption of hydrogen on the surface of platinum or gold), redox reactions of transition metal oxides (*e.g.*  $\text{RuO}_2$ ), and reversible electrochemical doping-dedoping in conductive polymer based electrodes.

[59] The main difference between pseudo-capacitance and EDL capacitance lies in the fact that *pseudo*-capacitance is faradic in origin, involving fast and reversible redox reactions between the electrolyte and electro-active species on the electrode surface. The most commonly known active species are ruthenium oxide,[60] manganese oxide[61], vanadium nitride,[62] electrically conducting polymers such as polyaniline,[63] and oxygen- or nitrogen- containing surface functional groups.[16] Generally in double layer carbon capacitors, there is about 1-5% pseudo-capacitance due to the functional groups on the surface, but there is also 5-10% double layer capacitance in a battery.[64] While pseudo-capacitance can be higher than EDL capacitance, it suffers from the drawbacks of a low power density (due to poor electrical conductivity), and lack of stability during cycling. The accumulation of electrons at the electrode of this kind of supercapacitor is a Faradaic process where the electrons produced by the redox reaction are transferred across the electrolyte-electrode interface. The theoretical pseudo-capacitance of metal oxide can be calculated in Equation 1-6:

$$C = \frac{n \times F}{M \times V} \quad (1-6)$$

where n is the mean number of the electrons transferred in the redox reaction, F is the Faraday constant, M is the molar mass of the metal oxide and V is the operating voltage window.

The energy density (E) of a supercapacitor is expressed as Equation 1-7,

$$E = \frac{CV^2}{2} \quad (1-7)$$

And, the maximum power density of a supercapacitor is determined by Equation 1-8:

$$P_{max} = \frac{V^2}{4R} \quad (1-8)$$

where R is the equivalent series resistance of all the components in the device.

Pseudo-capacitance often happens at the surface of the electrode use completely different charge storage mechanism applies from EDLC. The moving of charge across the double layer to the inside of active materials is like the reactions of battery.[65, 66] Metal oxides, especially transition metal oxides show excellent pseudo-capacitance performance. They are being investigated as the alternative materials for supercapacitor electrodes, including RuO<sub>2</sub>, MnO<sub>2</sub>, NiO, Co<sub>3</sub>O<sub>4</sub>, SnO<sub>2</sub>, ZnO, TiO<sub>2</sub>, V<sub>2</sub>O<sub>5</sub>, CuO, Fe<sub>2</sub>O<sub>3</sub>, etc.[65, 67-69] Both electrical double layer capacitor (EDLC) and pseudo-capacitance can be simultaneously generated in a single supercapacitor to form a hybrid supercapacitor. Hybrid supercapacitors can utilize both Faradaic and non- Faradaic processes to store charges to achieve higher energy and power densities while keeping good cycling stability. For example, the redox reaction takes place on one of the electrodes and the non-Faradaic charge-discharge process occurs on another electrode in a single supercapacitor. Such a supercapacitor is called an asymmetric hybrid super-capacitor. Other two types of hybrid supercapacitors are battery-like hybrids and composite hybrids. In practice, various types of supercapacitors have been developed to combine different electrode materials in order to improve the device performance.

### 1.3.2 Electrolytes

Electrolytes are a central element of capacitors. Two electrodes are interconnected by an electrolyte that determines charge transport. In general, there are three types of electrolytes: 1) aqueous electrolytes, 2) organic electrolytes, and 3) ionic liquids (ILs).[70] All three types of electrolytes have their own advantages and disadvantages when used in capacitors. Aqueous electrolytes have smaller solvated ions and higher dielectric constants, both of which promote capacitance. Whereas higher dielectric values promote storage, at the same time smaller solvated ions provide access to different pores. Aqueous electrolytes have higher conductivities than those of organic electrolytes, which results in a better power delivery. Conversely, aqueous electrolytes are limited to operations below 1.2 V because water molecules start to decompose above this voltage. The energy density is proportional to the square of the voltage, giving rise to a lower energy density. Due to this, organic electrolytes with higher operating voltages up to 2.5-3.0 V have been used, which gives rise to energy densities six to nine times that of the aqueous solution. However, the solvated ion size is supposedly larger than that of protons and generally leads to a smaller capacitance. Thus, control of the pore sizes of the electrodes is a key factor for achieving a high capacitance. Another drawback is the poor stability of organic electrolytes in air. Whereas aqueous solutions are free of environmental constraints, most organic electrolytes are hygroscopic, which means that they are sensitive to moisture, and, in particular, lithium-containing electrolytes are flammable when exposed to air, which is dangers in actually usage.

ILs, also called room temperature ionic liquids, are organic salts that are liquid at, or close to, room temperature. These salts have been the subject of considerable interest due to their very low volatility and their ability to dissolve a wide variety of compounds; this combination of properties makes ionic liquids useful as “green” solvents for energy applications and industrial processes.

ILs has broad window of electrochemical stability, which can be as large as 6.0 V.[71] This window makes these ionic liquids promising candidates for use as electrolytes for electrochemistry. While materials with large voltage windows are desirable, they may also possess unacceptably high viscosities and insufficient conductivities for use as electrolytes. High viscosities often result in higher oxidation potentials (due to decreased mass transport rates) and longer reaction times.[72] The further increase in operating voltage can be realized with the use of an IL; a potential window of 3.7 V has been obtained in our work when using an IL (EMI-TFSI) along with a very high specific energy density of 123 Wh kg<sup>-1</sup>. [73] Although a wider potential window can be obtained, ILs suffer from their highly viscous nature. High viscosity provides good wettability of the electrode material, but at the same time it prevents smooth ion transfer.

### **1.3.3 Graphene-based Materials as Supercapacitor Electrodes**

A supercapacitor, is a kind of electrochemical device that stores and releases energy at high rate (in seconds) with high power density (10 kW kg<sup>-1</sup>) and long cycling life.[59] However, the energy density of supercapacitor (e.g., 4-5 Wh kg<sup>-1</sup> for those based on the porous activated carbon) is generally lower than that of batteries (e.g., 26-34 Wh kg<sup>-1</sup> for lead acid batteries).[74] Improving the energy density of supercapacitors

while maintaining their high power density and long cycle life has been the key issue in developing future energy storage systems.

Carbon-based materials, such as activated carbon (AC), CNTs, ~~carbon~~ fibers, and graphene, are electrical double layer capacitors (EDLCs), which function through the accumulation of charges at the electrode/electrolyte interface. Therefore, large specific surface area (SSA) and good electrical conductivity are the two critical requirements for the high performance EDLCs. In this regard, graphene-based materials derived from the GO nanosheets, which can be prepared on a ton scale, are promising candidates for EDLCs. Ruoff and coworkers demonstrated the first rGO-based EDLC, which showed a specific capacitance of 135 F g<sup>-1</sup> and 99 F g<sup>-1</sup> in the aqueous and organic electrolyte, respectively.[75] After that, a great amount of work has been devoted to optimize the performance of supercapacitors made of graphene-derivatives, leading to improved specific capacitance values of ~200, 120, and 75 F g<sup>-1</sup> in aqueous, organic, and ionic liquid electrolyte, respectively.[76-78] However, the graphene-derived materials usually show a smaller SSA than the theoretical value of graphene monolayer, i.e., 2630 m<sup>2</sup> g<sup>-1</sup>. Recently, a simple but effective method to prepare the KOH-activated, microwave exfoliated graphite oxide(MEGO) or thermal exfoliated graphite oxide (TEGO). The obtained materials, which contain mostly single layers of sp<sup>2</sup>-bonded carbon, are highly porous (0.5- 6 nm sized pores) and exhibit an ultrahigh SSA value up to 3100 m<sup>2</sup> g<sup>-1</sup>, as well as a low oxygen and hydrogen content and a high electrical conductivity ( ~ 500 S m<sup>-1</sup>).[21] The KOH activation process was performed by heating a mixture of filtered MEGO/KOH or TEGO/KOH in a tube furnace at 800 ° C for 1 hour under flowing argon. At a current density of 5.7 A g<sup>-1</sup>, the activated-MEGO electrode showed an exceptionally high energy density of ~70 Wh kg<sup>-1</sup> and power density of ~250 kW kg<sup>-1</sup>. Recently, laser irradiation has been applied as an effective reduction method to prepare rGO electrodes.[20, 79] El-Kady et al. developed a simple strategy to produce graphene-based supercapacitors by laser-irradiation of a GO film coated on a flexible substrate mounted in a commercial CD/DVD drive.[20] After laser irradiation, the initially stacked GO sheets in the film were reduced and simultaneously exfoliated to give the laser -scribed graphene (LSG) sheets, which showed high electrical conductivity (1738 S m<sup>-1</sup>), large SSA of 1520 m<sup>2</sup> g<sup>-1</sup>, and good mechanical flexibility. Moreover, the LSG films can be directly used as electrodes, functioning as both the active material and current collector in a capacitor, that is, a device can be simply made by separating two LSG electrodes with an ionic porous separator. These LSG electrochemical capacitors (LSG-ECs) exhibited competitive electrochemical energy storage capability with both ultrahigh power and energy density.

It has been shown that graphite oxide can be used as a solid-electrolyte, and becomes ionic conductive and electrical insulating when a substantial amount of water is trapped in it, which makes it an ideal electrolyte and electrode separator.[80, 81] Taking advantage of this, Gao and coworkers prepared graphene-based supercapacitors by using the laser reduction method to write rGO-GO-rGO patterns with different configurations, in which the rGO regions serve as electrodes and hydrated-GO regions act as the electrolyte/separator membrane. This approach is facile and scalable, and the resulting micro-patterned

supercapacitors exhibited good energy storage capacities and cycling stability, which are comparable with the existing thin film supercapacitors. [79]

In addition to the specific surface area (SSA) and electrical conductivity, the structure and morphology of carbon-based electrodes also play a crucial role in controlling their performance.[82] Miller and coworkers deposited vertically oriented graphene nanosheets on a heated Ni substrate, using radio frequency plasma-enhanced chemical vapor deposition (PECVD).[83] The thus made electrode showed an SSA of about  $1100 \text{ m}^2 \text{ g}^{-1}$ , and efficient filtering of 120Hz current with a resistance capacitance time constant of less than 0.2 ms. Moreover, the film made of these vertically aligned graphene nanosheets with exposed edge planes exhibited greatly increased charge storage as compared to the control device relying on flat graphene sheets. Similar to this work, Yoo et al.[84] developed “in-plane” ultrathin supercapacitors comprised of CVD-grown graphene or multilayer rGO sheets. This design enables the enhanced interaction between the electrolyte and carbon layers, maximizing the interface area by fullyutilizing the surface of graphene layers. The “in-plane” capacitor made of as-grown single- to double-layer graphene sheets exhibited high specific capacity up to  $80 \mu \text{ F cm}^{-2}$ , and that made of rGO sheets showed even higher capacity of  $394 \mu \text{ F cm}^{-2}$ .

Moreover, the hybrid electrodes produced from graphene and the other types of carbon materials, such as CNTs, have also been developed by physical mixing rGO sheets and CNTs, [85] or CVD-growth of CNTs on graphene sheets.[86] In these reports, one of the key contributions of CNTs is that they provide highly conductive pathways between graphene layers, since the spacing between the stacked graphene layers can cause an increase of the series resistance along the stacked direction. The incorporation of CNTs can also enlarge the SSA of the hybrid electrode, and enhance the cycling stability by preventing the restacking of graphene sheets. In addition to CNTs, the three dimensional (3D) carbon architectures can also prepared by inserting mesoporous carbon spheres between graphene sheets.[87] The fabrication process involves the self-assembly of positively charged mesoporous silica spheres (MSS) and negatively charged GO sheets, followed by the simultaneous reduction of GO and CVD-growth of porous carbon on the MSS templates. The silica templates are subsequently removed, leaving the mesoporous carbon spheres intercalated between rGO sheets with a high SSA of  $1496 \text{ m}^2 \text{ g}^{-1}$ . The obtained electrodes based on this 3D carbon architecture, as compared to those made from hydrazine-reduced rGO sheets, showed a lower O/C ratio, lower series resistance, higher power capability, and excellent cyclability with 94% retention of capacitance after 1000 cycles of charge-discharge.

### 1.3.4 Other Carbon Materials

#### Activated carbon

A typical example of an EDLC material is ACs. They have been commercially used as supercapacitor electrode materials. However, their applications are still restricted to only certain niche markets due to the limited energy storage and rate capability. A full understanding of the charge-storage mechanism in AC electrodes is very important due to the complexity of its pore structures. The capacity depends on several mutually interlinked parameters, that is, total specific surface area, normally referred to as the Brunauer-

Emmet-Teller (BET) surface area; the nature of the porosity of the electrode; the pore size distribution; and the conductivity of the electrode material. ACs have highly porous surface areas consisting of different types of pores. Porous electrodes can be divided into three main categories based on the dimension of their diameters: 1) micro- (< 2 nm), 2) meso- (2-50 nm), and 3) macropores (> 50 nm).<sup>[59]</sup> An electrode, in general, consists of these three types of pores. Because different types of pores interact with ions in electrolytes in different ways,<sup>[88]</sup> the capacitance performance of an electrode is affected by the relative amount of pores with different sizes present in the electrode. Although ACs have a high specific surface area (>1000 m<sup>2</sup> g<sup>-1</sup>), the symmetric supercapacitors made with ACs have a relatively low specific capacitance, which is mainly due to their low mesoporosity and, in turn, low electrolyte accessibility. The root cause for the low electrolyte accessibility is often attributed to the mismatch of the ion size of an electrolyte and pore size of an electrode material. In order to solve this problem, the pore size of the electrode must be suitable for the ion size of the electrolyte, so the ions in the electrolyte can be fully utilized to form the double layer and contribute to the energy storage.<sup>[89, 90]</sup> Several researchers have pointed out the discrepancy between the capacitance of the ACs and their specific surface area. With a high surface area up to 3000 m<sup>2</sup> g<sup>-1</sup>, only a relatively small specific capacitance of 10 mF cm<sup>2</sup> was obtained, much smaller than the theoretical EDL capacitance (15-25 mF cm<sup>2</sup>),<sup>[59]</sup> indicating that not all pores are effective in charge accumulation.<sup>[91]</sup>

Efforts have been made to search for the relationship between the nanoporous structure of ACs and their capacitance performance in different electrolytes. In general, the capacitance of ACs is higher in aqueous electrolytes (ranging from 100 F g<sup>-1</sup> to 300 F g<sup>-1</sup>) than in organic electrolytes (less than 150 F g<sup>-1</sup>). One reason for this is believed to be the larger effective size of the electrolyte ions in organic solutions when compared with those in water. Organic electrolytes increase the number of pores that are smaller than the ions, and therefore increase the number not contributing to the charge storage. The wettability of the carbon surface by the organic electrolyte, which is determined by the chemical affinity between the two, may be another reason.<sup>[92, 93]</sup> Besides the porous structure of ACs, the surface functionalities also play important roles on the carbon electrode performance, as they will affect the wettability of the carbon surface by the electrolyte ions and give additional pseudo-capacitance.<sup>[51, 94, 95]</sup> However, most commercial supercapacitors use organic electrolytes because of the higher operating voltages, which offer a higher energy density. Pandolfo and Hollenkamp have given an overview of ACs with various types of functional groups and pointed out that the presence of some active surface oxides and a trace amount of water result in instability of the electrode, an increase of series resistance and the decomposition of the organic electrolyte. Some other studies also showed the aging of AC electrodes in organic electrolytes due to the active surface of carbon.<sup>[96]</sup> Therefore, surface functionality and porosity of ACs should be optimized for improved long-term performance. Pure ACs without heteroatoms and water might be better for use in an organic electrolyte.

### **Carbon nanotubes (CNTs)**

The discovery of CNTs has significantly advanced the science and engineering of carbon materials. As discussed previously, the major factor that determines the power density is the overall resistance of the components in a supercapacitor. Carbon nanotubes, due to their unique pore structure, superior electrical

properties, and good mechanical and thermal stability, have attracted a great deal of attention for supercapacitor electrode applications.[97-99] CNTs can be categorized as single-walled carbon nanotubes (SWNTs) or multi-walled carbon nanotubes (MWNTs), both of which have been widely explored as energy storage electrode materials. CNTs are usually regarded as the choice of a high-power electrode material because of their good electrical conductivity and readily accessible surface area. Moreover, their high mechanical resilience and open tubular network make them a good support for active materials. The energy density is, however, a concern due to their relatively small specific surface area (generally  $\sim 500 \text{ m}^2 \text{ g}^{-1}$ ) as compared to ACs. Of greater importance is the difficulty in retaining the intrinsic properties of individual CNTs on a macroscopic scale[97] and the high purity and electrolyte-dependent capacitance performance.[98]

It should be taken into account that recent studies have shown that entangled CNTs are less efficient in facilitating fast ionic transportation when compared to aligned CNTs, due to the irregular pore structures and high entanglement of the CNT structure in the former.[100] Hence, the use of aligned CNT seems to be more advantageous in terms of power performance. Futaba and co-workers have presented a method to fabricate a densely packed aligned SWNT solid by using the zipping effect of liquids, which allowed the bulk materials to retain the intrinsic properties of the SWNTs.[97] The energy density of the obtained SWNT solid was about  $35 \text{ Wh kg}^{-1}$  (normalized to a cell consisting of two identical electrode materials) in organic electrolyte, and the rate capability was better than that of ACs. These studies showed the importance of the aligned tubular structures and preserved intrinsic CNT properties on the electrochemical performance of the electrode materials. Research has been undertaken to improve the energy density of CNTs by increasing their specific surface area via chemical activation (KOH activation).[51] However, a proper balance between the porosity and the conductivity must be achieved in order to have both high capacitance and good rate performance.

An interesting CNT-aerogel composite material was synthesized by uniformly dispersing a carbon aerogel throughout the CNT host matrix without destroying the integrity or reducing the aspect ratio of the CNT.[99] A high specific surface area of  $1059 \text{ m}^2 \text{ g}^{-1}$  and extremely high specific capacitance of  $524 \text{ F g}^{-1}$  were obtained, but at the expense of a tedious preparation pathway. Another way to enhance the specific capacitance is by modification of CNTs with active materials to realize pseudo-capacitance through faradic processes.[61, 101] In spite of having excellent properties, the limited surface area of CNTs restricted their use as high energy performance EDLCs. In addition, the present difficulty in purification and high cost of production still hinder their practical applications.

### **Activated carbon fibers (ACFs), carbon aerogels (CAGs) and templated carbons**

Other carbon structures such as activated carbon fibers (ACFs), carbon aerogels (CAGs) and templated carbons have also been studied for supercapacitor applications. The general rules for the selection of supercapacitor electrode materials are a high and accessible specific surface area with good electrical conductivity. ACFs typically have high specific surface areas, up to  $3000 \text{ m}^2 \text{ g}^{-1}$ , and a more or less controllable pore size distribution.[102] They are usually produced from the carbonization of pre-formed fibrous carbon precursors followed by activation processes. A high capacitance value of  $371 \text{ F g}^{-1}$  in KOH

electrolyte solution was reported recently. However, such a high specific surface area together with the presence of surface functional groups may cause a long term stability problem.[89] In addition, the cost of ACF production is generally higher than AC.

Carbon aerogels (CAGs) are another interesting material suitable for use as a supercapacitor electrode. They are ultralight, highly porous materials, predominantly with mesopores, and have the possibility of usage without binding substances. CAGs are typically fabricated through a sol-gel process with subsequent pyrolysis of the organic aerogels. The special porosity of a CAG is based on the interconnection of colloidal-like carbon nanoparticles. Due to the dominance of mesopores ( $>2$  nm), the EDL capacitance is not so effective in CAG-based electrode materials. Hence, an additional activation process was employed to further increase the specific surface area by introducing microporosity. Despite a large increase in the total surface area (from 592 to 2371  $\text{m}^2 \text{g}^{-1}$ ), the improvement on the charge storage capacity was relatively small, especially at high discharge rates, which is primarily due to the inaccessibility of the micropores produced during the activation and the relatively high internal resistance of the CAG matrix.[103]

The preparation procedure of template carbons is infiltration of a carbon precursor into the pores of the template, followed by a carbonization treatment and finally the removal of the template to leave behind a porous carbon structure. Various carbon structures with well controlled micropores, mesopores and/or macropores produced from different types of template and carbon precursors have been studied for supercapacitor applications.[104-108] For example, a functionalized microporous carbon material was obtained by using zeolite Y as a template and the resultant carbon material possessed a high gravimetric capacitance of about 340  $\text{F g}^{-1}$  in aqueous electrolyte with good cycling ability (over 10 000 cycles).[104] Compared to ACs, whose micropores are essentially disordered and broad in pore size distribution, the template microporous carbons with a narrow pore size distribution, well adapted pore size to the electrolyte ions and the ordered straight pore channels are better for use as high-energy-density electrode materials. The templating method has been shown to be one of the most suitable techniques to control the preparation of porous materials, especially ordered porous solids. Through careful selection of the template materials as well as the carbon precursors, and with good control over the carbonization process, nanoporous template carbons with desirable physical and chemical properties can be obtained. In view of their relatively high cost of production, development of a simple, economical and environmentally benign template route would be advantageous for their future application. Despite the cost, template carbons are good materials to study, which provide valuable information about the effect of pore size, pore shape, channel structures and other parameters on the ion diffusion and charge storage in the nano-confined system.[109]

## 1.4 Applications of Graphene in Electro-chemical Sensors and Biosensors

Ever since its discovery, graphene has quickly become a material under spotlight for development of new electro-chemical sensors because of its unique electrochemical and structural properties (extremely high surface-to-volume ratio, theoretically, 2600  $\text{m}^2 \text{g}^{-1}$ ). Since graphene has a large electro-chemical potential

window (approximately 2.5 V in 0.1mM phosphate buffer saline solution), detection of molecules that have high oxidation or reduction potential (e.g., nucleic acids) become feasible. In addition, edges and defects on graphene provide a high electron transfer rate, suggesting that reduced graphene oxide (RGO) sheets or small flakes of pristine graphene are superior for electrochemical detection. [110] It has been demonstrated that the electron transfer rate of  $\text{Fe}^{3+/2+}$  on RGO is more than an order of magnitude higher than that on a glassy carbon electrode (GCE) due to the unique electronic structure of RGO, especially the high density of the electronic states over a wide energy range.[1, 111] Electron transfer can be enhanced also because small graphene flakes are able to provide direct electrical wiring between the electrode and the active centers of the redox enzymes. The “electro-catalytic” behavior and enhanced analytical performance of graphene and related structures has been widely reported, for example RGO has intrinsic catalytic activity towards some small enzymatic products such as  $\text{H}_2\text{O}_2$  and NADH, making it attractive for enzyme-based sensors.[25] and also towards the detection of bisphenol A,[112] cadmium,[113] dopamine (DA),[114] hydrazine,[115] to name a few.

The majority of graphene used in electrochemistry is produced through the reduction of GO, which results in partially functionalized graphene sheets or chemically reduced GO. Graphene produced in this manner usually has abundant structural defects (edge plane like-sites/defects),[116, 117] and remaining functional groups which have been shown to greatly influence the electrochemical performance of the graphene fabricated device in terms of heterogeneous electron transfer rates and can be either advantageous or detrimental towards the sensing of a target analyte.[1, 118-120]

Nevertheless, Brownson, et al[121] investigated the full-implications of employing pristine graphene in the electrochemical context. HOPG electrode substrates that exhibited either fast or slow electron transfer kinetics (Edge Plane Pyrolytic Graphite (EPPG) or Basal Plane Pyrolytic Graphite (BPPG) electrodes respectively) were modified with well characterised commercially available graphene, had not been chemically treated and had an extremely low oxygen content (<5%). Interestingly, it was observed that the graphene modified electrodes exhibited a reduced analytical performance in terms of sensitivity, linearity and the respective detection limits towards each of the analytes studied when comparison to the unmodified underlying electrode substrates (constructed from graphite) was sought; as for the case of DA detection, where increments in the over-potential are evident at the graphene modified electrodes when compared to the graphite alternatives and significantly lower peak heights (currents) reside. This “reduced performance” is clearly contradictory to the majority of current literature reports which claim that the application of graphene leads to an enhancement in the electroanalytical response in many instances.[112-115] Further studies have demonstrated that single-, few-, and multi-layer graphene does not provide a significant advantage over graphite micro-particles in terms of sensitivity, linearity and repeatability towards the electro-analytical detection of UA, where sensitivities of 4.65 and 5.11mA  $\text{mM}^{-1}$  were recorded for graphene and graphite modified electrodes respectively.[122] These findings were later extended with regards to the electrochemical detection of 2,4,6-trinitrotoluene (TNT) where a graphite microparticle modified electrode

was shown to provide enhanced electro-analytical sensitivity when compared to the performance of single-, few-, and multi-layer graphene alternatives.[123]

It is evident that due to graphene's structural composition, there appears to be no advantages of employing pristine graphene in this electroanalytical context, that is, in the case of the analytes covered here or where fast electrode kinetics are imperative with respect to enhanced analytical performances. It must be noted that within these select studies the EPPG electrode consistently exhibited the best performance owing to its favourable orientation of the graphite planes resulting in optimum edge plane coverage (and in certain cases the presence of oxygenated species), [121, 124, 125] which questions the need to modify electrodes with graphene for the electroanalysis of target analytes in the place. However, it should be remembered that graphene-based nanomaterials can differ significantly if different methods of preparation are used or even if small variations of a single method are employed.[126] Therefore, any graphene nanomaterial should be thoroughly characterized to avoid potential misinterpretation.[127] Furthermore, this allows the effective manipulation and tailoring of the electrochemical properties of graphene for specific applications. Thus if the orientation of graphene was controlled/manipulated to give rise to a large degree of accessible edge plane like-sites/defects, one would expect to observe an improved performance in terms of electroanalysis.

## 1.5 Motivation and Objective

Graphene and chemical reduced graphene oxide (CRGO) sheets have high surface area, high conductivity, and outstanding mechanical properties are promising materials for supercapacitor. In the meanwhile, the cost is low and it can be mass product. The specific capacitance of single layer graphene is 2630 m<sup>2</sup>/g, which is bigger than that of activated carbon and carbon nanotubes. The theoretical specific capacitance is 526 F/g at most in an aqueous electrolyte. However, the current reported data could only obtained around 40% of its theoretical specific capacitance. The main problem is the restacking of graphene sheets, which obviously reduce the specific surface area of the electrode. So in this work, we would like to tailor a microstructure of the graphene based composite, introducing surfactant derived single-walled carbon nanotube as spacer and conductive binder, to increase the accessibility to the electrode. And usage of ionic liquid electrolyte at high voltage, further improve the energy density.

The application of graphene based materials are closely related its preparation method. Among all the preparation methods, hydrothermal process is an efficient and non-toxic method for production of graphene without using any chemical reagents or catalysts. Moreover besides the high surface area, this method introduces more functional groups and structure defects to the graphene based materials, which is significant in graphene based biosensor. In this work, hydrothermal graphene based composites were applied to biosensor electrode for detection of biomolecule uric acid.

And in order to figure out the effect of the position (edge and basal) and oxygen groups of graphene in electrochemistry, we selectively masking regions of the highly oriented pyrolytic graphite (HOPG) with a

nonconducting polymer coating such that the electrolyte has access the basal plane and edge only, to study their respective electrochemical performance in supercapacitors and electrochemical biosensors.

## References

1. McCreery RL. Advanced Carbon Electrode Materials for Molecular Electrochemistry. *Chemical Reviews* 2008,108:2646-2687.
2. Geim AK, Novoselov KS. The rise of graphene. *Nat Mater* 2007,6:183-191.
3. Yang W, Ratinac KR, Ringer SP, Thordarson P, Gooding JJ, Braet F. Carbon Nanomaterials in Biosensors: Should You Use Nanotubes or Graphene? *Angewandte Chemie International Edition* 2010,49:2114-2138.
4. Pumera M. Electrochemistry of Graphene: New Horizons for Sensing and Energy Storage. *Chemical Record* 2009,9:211-223.
5. Chen D, Tang L, Li J. Graphene-based materials in electrochemistry. *Chem Soc Rev* 2010,39:3157-3180.
6. Geim AK, Novoselov KS. The rise of graphene. *Nature Materials* 2007,6:183-191.
7. Novoselov KS, Geim AK, Morozov SV, Jiang D, Zhang Y, Dubonos SV, et al. Electric field effect in atomically thin carbon films. *Science* 2004,306:666-669.
8. Huang X, Qi X, Boey F, Zhang H. Graphene-based composites. *Chem Soc Rev* 2012,41:666-686.
9. Huang X, Yin Z, Wu S, Qi X, He Q, Zhang Q, et al. Graphene-Based Materials: Synthesis, Characterization, Properties, and Applications. *Small* 2011,7:1876-1902.
10. He Q, Wu S, Yin Z, Zhang H. Graphene-based electronic sensors. *Chemical Science* 2012,3:1764-1772.
11. Huang X, Zeng ZY, Fan ZX, Liu JQ, Zhang H. Graphene-Based Electrodes. *Advanced Materials* 2012,24:5979-6004.
12. Du X, Skachko I, Barker A, Andrei EY. Approaching ballistic transport in suspended graphene. *Nat Nano* 2008,3:491-495.
13. Nair RR, Blake P, Grigorenko AN, Novoselov KS, Booth TJ, Stauber T, et al. Fine Structure Constant Defines Visual Transparency of Graphene. *Science* 2008,320:1308.
14. Balandin AA, Ghosh S, Bao W, Calizo I, Teweldebrhan D, Miao F, et al. Superior Thermal Conductivity of Single-Layer Graphene. *Nano Letters* 2008,8:902-907.
15. Lee C, Wei X, Kysar JW, Hone J. Measurement of the Elastic Properties and Intrinsic Strength of Monolayer Graphene. *Science* 2008,321:385-388.
16. Stoller MD, Park SJ, Zhu YW, An JH, Ruoff RS. Graphene-Based Ultracapacitors. *Nano Letters* 2008,8:3498-3502.
17. Torrisi F, Hasan T, Wu W, Sun Z, Lombardo A, Kulmala TS, et al. Inkjet-Printed Graphene Electronics. *Acs Nano* 2012,6:2992-3006.
18. Eda G, Fanchini G, Chhowalla M. Large-area ultrathin films of reduced graphene oxide as a transparent and flexible electronic material. *Nat Nano* 2008,3:270-274.
19. Wu J, Agrawal M, Becerril HA, Bao Z, Liu Z, Chen Y, et al. Organic Light-Emitting Diodes on Solution-Processed Graphene Transparent Electrodes. *Acs Nano* 2009,4:43-48.
20. El-Kady MF, Strong V, Dubin S, Kaner RB. Laser Scribing of High-Performance and Flexible Graphene-Based Electrochemical Capacitors. *Science* 2012,335:1326-1330.

21. Zhu YW, Murali S, Stoller MD, Ganesh KJ, Cai WW, Ferreira PJ, et al. Carbon-Based Supercapacitors Produced by Activation of Graphene. *Science* 2011,332:1537-1541.
22. Radhakrishnan G, Cardema JD, Adams PM, Kim HI, Foran B. Fabrication and Electrochemical Characterization of Single and Multi-Layer Graphene Anodes for Lithium-Ion Batteries. *Journal of the Electrochemical Society* 2012,159:A752-A761.
23. Yao F, Gunes F, Ta HQ, Lee SM, Chae SJ, Sheem KY, et al. Diffusion Mechanism of Lithium Ion through Basal Plane of Layered Graphene. *Journal of the American Chemical Society* 2012,134:8646-8654.
24. Xu MS, Fujita D, Hanagata N. Perspectives and Challenges of Emerging Single-Molecule DNA Sequencing Technologies. *Small* 2009,5:2638-2649.
25. Kuila T, Bose S, Khanra P, Mishra AK, Kim NH, Lee JH. Recent advances in graphene-based biosensors. *Biosens Bioelectron* 2011,26:4637-4648.
26. Shao YY, Wang J, Wu H, Liu J, Aksay IA, Lin YH. Graphene Based Electrochemical Sensors and Biosensors: A Review. *Electroanalysis* 2010,22:1027-1036.
27. Partoens B, Peeters FM. From graphene to graphite: Electronic structure around the K point. *Physical Review B* 2006,74:075404.
28. Morozov SV, Novoselov KS, Schedin F, Jiang D, Firsov AA, Geim AK. Two-dimensional electron and hole gases at the surface of graphite. *Physical Review B* 2005,72:201401.
29. Emtsev KV, Bostwick A, Horn K, Jobst J, Kellogg GL, Ley L, et al. Towards wafer-size graphene layers by atmospheric pressure graphitization of silicon carbide. *Nat Mater* 2009,8:203-207.
30. Sutter PW, Flege J-I, Sutter EA. Epitaxial graphene on ruthenium. *Nat Mater* 2008,7:406-411.
31. Kwak J, Chu JH, Choi J-K, Park S-D, Go H, Kim SY, et al. Near room-temperature synthesis of transfer-free graphene films. *Nat Commun* 2012,3:645.
32. Pei S, Cheng H-M. The reduction of graphene oxide. *Carbon* 2012,50:3210-3228.
33. Cai M, Thorpe D, Adamson DH, Schniepp HC. Methods of graphite exfoliation. *Journal of Materials Chemistry* 2012,22:24992-25002.
34. Choucair M, Thordarson P, Stride JA. Gram-scale production of graphene based on solvothermal synthesis and sonication. *Nat Nano* 2009,4:30-33.
35. Wei D, Xie L, Lee KK, Hu Z, Tan S, Chen W, et al. Controllable unzipping for intramolecular junctions of graphene nanoribbons and single-walled carbon nanotubes. *Nat Commun* 2013,4:1374.
36. Xie L, Wang H, Jin C, Wang X, Jiao L, Suenaga K, et al. Graphene Nanoribbons from Unzipped Carbon Nanotubes: Atomic Structures, Raman Spectroscopy, and Electrical Properties. *Journal of the American Chemical Society* 2011,133:10394-10397.
37. Reina A, Jia X, Ho J, Nezich D, Son H, Bulovic V, et al. Large Area, Few-Layer Graphene Films on Arbitrary Substrates by Chemical Vapor Deposition. *Nano Letters* 2008,9:30-35.
38. Li X, Magnuson CW, Venugopal A, Tromp RM, Hannon JB, Vogel EM, et al. Large-Area Graphene Single Crystals Grown by Low-Pressure Chemical Vapor Deposition of Methane on Copper. *Journal of the American Chemical Society* 2011,133:2816-2819.
39. Gao L, Ren W, Xu H, Jin L, Wang Z, Ma T, et al. Repeated growth and bubbling transfer of graphene with millimetre-size single-crystal grains using platinum. *Nat Commun* 2012,3:699.

40. Iwasaki T, Park HJ, Konuma M, Lee DS, Smet JH, Starke U. Long-Range Ordered Single-Crystal Graphene on High-Quality Heteroepitaxial Ni Thin Films Grown on MgO(111). *Nano Letters* 2010,11:79-84.
41. Dai B, Fu L, Zou Z, Wang M, Xu H, Wang S, et al. Rational design of a binary metal alloy for chemical vapour deposition growth of uniform single-layer graphene. *Nat Commun* 2011,2:522.
42. Gu W, Zhang W, Li X, Zhu H, Wei J, Li Z, et al. Graphene sheets from worm-like exfoliated graphite. *Journal of Materials Chemistry* 2009,19:3367-3369.
43. Li X, Wang X, Zhang L, Lee S, Dai H. Chemically Derived, Ultrasoft Graphene Nanoribbon Semiconductors. *Science* 2008,319:1229-1232.
44. Li X, Zhang G, Bai X, Sun X, Wang X, Wang E, et al. Highly conducting graphene sheets and Langmuir-Blodgett films. *Nat Nano* 2008,3:538-542.
45. Dhakate SR, Chauhan N, Sharma S, Tawale J, Singh S, Sahare PD, et al. An approach to produce single and double layer graphene from re-exfoliation of expanded graphite. *Carbon* 2011,49:1946-1954.
46. Hummers WS, Offeman RE. Preparation of Graphitic Oxide. *Journal of the American Chemical Society* 1958,80:1339-1339.
47. Cao X, He Q, Shi W, Li B, Zeng Z, Shi Y, et al. Graphene Oxide as a Carbon Source for Controlled Growth of Carbon Nanowires. *Small* 2011,7:1199-1202.
48. Liu J, Yin Z, Cao X, Zhao F, Lin A, Xie L, et al. Bulk Heterojunction Polymer Memory Devices with Reduced Graphene Oxide as Electrodes. *Acs Nano* 2010,4:3987-3992.
49. Zhu Y, Murali S, Stoller MD, Ganesh KJ, Cai W, Ferreira PJ, et al. Carbon-Based Supercapacitors Produced by Activation of Graphene. *Science* 2011,332:1537-1541.
50. Sato S, Harada N, Kondo D, Ohfuchi M. Graphene-Novel Material for Nanoelectronics. *Fujitsu Scientific & Technical Journal* 2010,46:103-110.
51. Pandolfo AG, Hollenkamp AF. Carbon properties and their role in supercapacitors. *Journal of Power Sources* 2006,157:11-27.
52. Helmholtz HPA. LXXXIX 1853,211.
53. Gouy LG. *comptes Rendus Chimie* 1909,149.
54. Gouy M. Sur la constitution de la charge électrique à la surface d'un électrolyte. *J. Phys. Theor. Appl.* 1910,9:457-468.
55. Chapman DL. LI. A contribution to the theory of electrocapillarity *Philosophical Magazine Series 6* 1913,25:475-481.
56. Stern OZ. *Electrochemistry*; 1924.
57. Sparnaay MJ. *Electric Double Layer*: Pergamon Press; 1972.
58. Grahame DC. The Electrical Double Layer and the Theory of Electrocapillarity. *Chemical Reviews* 1947,41:441-501.
59. Conway BE. *Electrochemical Supercapacitors: Scientific Fundamentals and Technological Applications*; 1999.
60. Hu C-C, Chang K-H, Lin M-C, Wu Y-T. Design and Tailoring of the Nanotubular Arrayed Architecture of Hydrous RuO<sub>2</sub> for Next Generation Supercapacitors. *Nano Letters* 2006,6:2690-2695.
61. Zhang H, Cao G, Wang Z, Yang Y, Shi Z, Gu Z. Growth of Manganese Oxide Nanoflowers on Vertically-Aligned Carbon Nanotube Arrays for High-Rate Electrochemical Capacitive Energy Storage. *Nano Letters* 2008,8:2664-2668.

62. Choi D, Blomgren GE, Kumta PN. Fast and Reversible Surface Redox Reaction in Nanocrystalline Vanadium Nitride Supercapacitors. *Advanced Materials* 2006,18:1178-1182.
63. Lee T, Yun T, Park B, Sharma B, Song HK, Kim BS. Hybrid multilayer thin film supercapacitor of graphene nanosheets with polyaniline: importance of establishing intimate electronic contact through nanoscale blending. *Journal of Materials Chemistry* 2012,22:21092-21099.
64. Jiang H, Ma J, Li CZ. Mesoporous Carbon Incorporated Metal Oxide Nanomaterials as Supercapacitor Electrodes. *Advanced Materials* 2012,24:4197-4202.
65. Wei W, Cui X, Chen W, Ivey DG. Manganese oxide-based materials as electrochemical supercapacitor electrodes. *Chem Soc Rev* 2011,40:1697-1721.
66. Snook GA, Kao P, Best AS. Conducting-polymer-based supercapacitor devices and electrodes. *Journal of Power Sources* 2011,196:1-12.
67. Lang X, Hirata A, Fujita T, Chen M. Nanoporous metal/oxide hybrid electrodes for electrochemical supercapacitors. *Nat Nano* 2011,6:232-236.
68. Duan BR, Cao Q. Hierarchically porous Co<sub>3</sub>O<sub>4</sub> film prepared by hydrothermal synthesis method based on colloidal crystal template for supercapacitor application. *Electrochimica Acta* 2012,64:154-161.
69. Yan D, Guo Z, Zhu G, Yu Z, Xu H, Yu A. MnO<sub>2</sub> film with three-dimensional structure prepared by hydrothermal process for supercapacitor. *Journal of Power Sources* 2012,199:409-412.
70. Ghosh A, Lee YH. Carbon-Based Electrochemical Capacitors. *Chemsuschem* 2012,5:480-499.
71. Galiński M, Lewandowski A, Stepniak I. Ionic liquids as electrolytes. *Electrochimica Acta* 2006,51:5567-5580.
72. Pringle JM, MacFarlane DR, Forsyth M. Solid state NMR analysis of polypyrrole grown in a phosphonium ionic liquid. *Synthetic Metals* 2005,155:684-689.
73. Zhang F, Tang J, Shinya N, Qin L-C. Hybrid graphene electrodes for supercapacitors of high energy density. *Chemical Physics Letters* 2013,584:124-129.
74. Burke A. R&D considerations for the performance and application of electrochemical capacitors. *Electrochimica Acta* 2007,53:1083-1091.
75. Stoller MD, Park S, Zhu Y, An J, Ruoff RS. Graphene-Based Ultracapacitors. *Nano Letters* 2008,8:3498-3502.
76. Wang Y, Shi Z, Huang Y, Ma Y, Wang C, Chen M, et al. Supercapacitor Devices Based on Graphene Materials. *The Journal of Physical Chemistry C* 2009,113:13103-13107.
77. Lv W, Tang D-M, He Y-B, You C-H, Shi Z-Q, Chen X-C, et al. Low-Temperature Exfoliated Graphenes: Vacuum-Promoted Exfoliation and Electrochemical Energy Storage. *Acs Nano* 2009,3:3730-3736.
78. Vivekchand SRC, Rout C, Subrahmanyam KS, Govindaraj A, Rao CNR. Graphene-based electrochemical supercapacitors. *Journal of Chemical Sciences* 2008,120:9-13.
79. Gao W, Singh N, Song L, Liu Z, Reddy ALM, Ci L, et al. Direct laser writing of micro-supercapacitors on hydrated graphite oxide films. *Nat Nano* 2011,6:496-500.
80. Gilje S, Han S, Wang M, Wang KL, Kaner RB. A Chemical Route to Graphene for Device Applications. *Nano Letters* 2007,7:3394-3398.
81. Cerveny S, Barroso-Bujans F, Alegría An, Colmenero J. Dynamics of Water Intercalated in Graphite Oxide. *The Journal of Physical Chemistry C* 2010,114:2604-2612.
82. Dillon AC. Carbon Nanotubes for Photoconversion and Electrical Energy Storage. *Chemical Reviews* 2010,110:6856-6872.

83. Miller JR, Outlaw RA, Holloway BC. Graphene Double-Layer Capacitor with ac Line-Filtering Performance. *Science* 2010,329:1637-1639.
84. Yoo JJ, Balakrishnan K, Huang J, Meunier V, Sumpter BG, Srivastava A, et al. Ultrathin Planar Graphene Supercapacitors. *Nano Letters* 2011,11:1423-1427.
85. Cheng Q, Tang J, Ma J, Zhang H, Shinya N, Qin LC. Graphene and carbon nanotube composite electrodes for supercapacitors with ultra-high energy density. *Physical Chemistry Chemical Physics* 2011,13:17615-17624.
86. Fan Z, Yan J, Zhi L, Zhang Q, Wei T, Feng J, et al. A Three-Dimensional Carbon Nanotube/Graphene Sandwich and Its Application as Electrode in Supercapacitors. *Advanced Materials* 2010,22:3723-3728.
87. Lei Z, Christov N, Zhao XS. Intercalation of mesoporous carbon spheres between reduced graphene oxide sheets for preparing high-rate supercapacitor electrodes. *Energy & Environmental Science* 2011,4:1866-1873.
88. Shi H. Activated carbons and double layer capacitance. *Electrochimica Acta* 1996,41:1633-1639.
89. Simon P, Gogotsi Y. Materials for electrochemical capacitors. *Nat Mater* 2008,7:845-854.
90. Huang J, Sumpter BG, Meunier V. A Universal Model for Nanoporous Carbon Supercapacitors Applicable to Diverse Pore Regimes, Carbon Materials, and Electrolytes. *Chemistry – A European Journal* 2008,14:6614-6626.
91. Kierzek K, Frackowiak E, Lota G, Gryglewicz G, Machnikowski J. Electrochemical capacitors based on highly porous carbons prepared by KOH activation. *Electrochimica Acta* 2004,49:515-523.
92. Raymundo-Piñero E, Kierzek K, Machnikowski J, Béguin F. Relationship between the nanoporous texture of activated carbons and their capacitance properties in different electrolytes. *Carbon* 2006,44:2498-2507.
93. Largeot C, Portet C, Chmiola J, Taberna P-L, Gogotsi Y, Simon P. Relation between the Ion Size and Pore Size for an Electric Double-Layer Capacitor. *Journal of the American Chemical Society* 2008,130:2730-2731.
94. Seredych M, Hulicova-Jurcakova D, Lu GQ, Bandosz TJ. Surface functional groups of carbons and the effects of their chemical character, density and accessibility to ions on electrochemical performance. *Carbon* 2008,46:1475-1488.
95. Raymundo-Piñero E, Leroux F, Béguin F. A High-Performance Carbon for Supercapacitors Obtained by Carbonization of a Seaweed Biopolymer. *Advanced Materials* 2006,18:1877-1882.
96. Azaïs P, Duclaux L, Florian P, Massiot D, Lillo-Rodenas M-A, Linares-Solano A, et al. Causes of supercapacitors ageing in organic electrolyte. *Journal of Power Sources* 2007,171:1046-1053.
97. Futaba DN, Hata K, Yamada T, Hiraoka T, Hayamizu Y, Kakudate Y, et al. Shape-engineerable and highly densely packed single-walled carbon nanotubes and their application as super-capacitor electrodes. *Nat Mater* 2006,5:987-994.
98. Frackowiak E, Jurewicz K, Delpeux S, Béguin F. Nanotubular materials for supercapacitors. *Journal of Power Sources* 2001,97-98:822-825.
99. Bordjiba T, Mohamedi M, Dao LH. New Class of Carbon-Nanotube Aerogel Electrodes for Electrochemical Power Sources. *Advanced Materials* 2008,20:815-819.
100. Hao Zhang GC, Yusheng Yang, and Zhennan Gu. Comparison Between Electrochemical Properties of Aligned Carbon Nanotube Array and Entangled Carbon Nanotube Electrodes *Journal of the Electrochemical Society* 2008,155:K19-22.
101. Zhang H, Cao G, Wang Z, Yang Y, Shi Z, Gu Z. Tube-covering-tube nanostructured polyaniline/carbon nanotube array composite electrode with high capacitance and superior rate performance as well as good cycling stability. *Electrochemistry Communications* 2008,10:1056-1059.

102. Xu B, Wu F, Chen R, Cao G, Chen S, Zhou Z, et al. Highly mesoporous and high surface area carbon: A high capacitance electrode material for EDLCs with various electrolytes. *Electrochemistry Communications* 2008,10:795-797.
103. Fang B, Binder L. A modified activated carbon aerogel for high-energy storage in electric double layer capacitors. *Journal of Power Sources* 2006,163:616-622.
104. Ania CO, Khomenko V, Raymundo-Piñero E, Parra JB, Béguin F. The Large Electrochemical Capacitance of Microporous Doped Carbon Obtained by Using a Zeolite Template. *Advanced Functional Materials* 2007,17:1828-1836.
105. Wang D-W, Li F, Liu M, Lu GQ, Cheng H-M. 3D Aperiodic Hierarchical Porous Graphitic Carbon Material for High-Rate Electrochemical Capacitive Energy Storage. *Angewandte Chemie International Edition* 2008,47:373-376.
106. Frackowiak E. Carbon materials for supercapacitor application. *Physical Chemistry Chemical Physics* 2007,9:1774-1785.
107. Stein A, Wang Z, Fierke MA. Functionalization of Porous Carbon Materials with Designed Pore Architecture. *Advanced Materials* 2009,21:265-293.
108. Li W, Chen D, Li Z, Shi Y, Wan Y, Wang G, et al. Nitrogen-containing carbon spheres with very large uniform mesopores: The superior electrode materials for EDLC in organic electrolyte. *Carbon* 2007,45:1757-1763.
109. Zhao XS, Su F, Yan Q, Guo W, Bao XY, Lv L, et al. Templating methods for preparation of porous structures. *Journal of Materials Chemistry* 2006,16:637-648.
110. Zhou M, Zhai Y, Dong S. Electrochemical Sensing and Biosensing Platform Based on Chemically Reduced Graphene Oxide. *Anal Chem* 2009,81:5603-5613.
111. Tang L, Wang Y, Li Y, Feng H, Lu J, Li J. Preparation, Structure, and Electrochemical Properties of Reduced Graphene Sheet Films. *Advanced Functional Materials* 2009,19:2782-2789.
112. B. Ntsendwana BBM, S. Sampath, O.A. Arotiba. Electrochemical Detection of Bisphenol A Using Graphene. *Int. J. Electrochem. Sci.* 2012,7.
113. Li J, Guo S, Zhai Y, Wang E. High-sensitivity determination of lead and cadmium based on the Nafion-graphene composite film. *Anal Chim Acta* 2009,649:196-201.
114. Kim Y-R, Bong S, Kang Y-J, Yang Y, Mahajan RK, Kim JS, et al. Electrochemical detection of dopamine in the presence of ascorbic acid using graphene modified electrodes. *Biosensors and Bioelectronics* 2010,25:2366-2369.
115. Wang Y, Wan Y, Zhang D. Reduced graphene sheets modified glassy carbon electrode for electrocatalytic oxidation of hydrazine in alkaline media. *Electrochemistry Communications* 2010,12:187-190.
116. Park S, Ruoff RS. Chemical methods for the production of graphenes. *Nat Nano* 2009,4:217-224.
117. Shao Y, Wang J, Wu H, Liu J, Aksay IA, Lin Y. Graphene Based Electrochemical Sensors and Biosensors: A Review. *Electroanalysis* 2010,22:1027-1036.
118. Brownson DAC, Banks CE. Graphene electrochemistry: an overview of potential applications. *Analyst* 2010,135:2768-2778.
119. Banks CE, Davies TJ, Wildgoose GG, Compton RG. Electrocatalysis at graphite and carbon nanotube modified electrodes: edge-plane sites and tube ends are the reactive sites. *Chemical Communications* 2005:829-841.
120. Kumar SP, Manjunatha R, Nethravathi C, Suresh GS, Rajamathi M, Venkatesha TV. Electrocatalytic Oxidation of NADH on Functionalized Graphene Modified Graphite Electrode. *Electroanalysis* 2011,23:842-849.

121. Brownson DAC, Foster CW, Banks CE. The electrochemical performance of graphene modified electrodes: An analytical perspective. *Analyst* 2012,137:1815-1823.
122. Goh MS, Pumera M. Single-, Few-, and Multilayer Graphene Not Exhibiting Significant Advantages over Graphite Microparticles in Electroanalysis. *Anal Chem* 2010,82:8367-8370.
123. Goh M, Pumera M. Graphene-based electrochemical sensor for detection of 2,4,6-trinitrotoluene (TNT) in seawater: the comparison of single-, few-, and multilayer graphene nanoribbons and graphite microparticles. *Analytical and Bioanalytical Chemistry* 2011,399:127-131.
124. Brownson DAC, Munro LJ, Kampouris DK, Banks CE. Electrochemistry of graphene: not such a beneficial electrode material? *RSC Advances* 2011,1:978-988.
125. Brownson DAC, Gorbachev RV, Haigh SJ, Banks CE. CVD graphene vs. highly ordered pyrolytic graphite for use in electroanalytical sensing. *Analyst* 2012,137:833-839.
126. Brownson DAC, Banks CE. The electrochemistry of CVD graphene: progress and prospects. *Physical Chemistry Chemical Physics* 2012,14:8264-8281.
127. Pumera M. Graphene-based nanomaterials and their electrochemistry. *Chem Soc Rev* 2010,39:4146-4157.

---

## Chapter 2

### Experimental Technique

---

This chapter provides necessary background information of the experimental methods used throughout this dissertation. These techniques will be referred to in the subsequent chapters.

#### 2.1 Electrochemical Methods

##### 2.1.1 Cyclic Voltammetry

Cyclic voltammetry (CV) is one of the most extensively used electrochemical techniques to study electroactive and conjugated polymers as well as metal oxides due to its simplicity and versatility. It provides both quantitative and qualitative information about the system under study. In this technique, the current at the working electrode is monitored as a function of the potential, while the potential is being swept over a specified voltage range at a constant rate. This dynamic parameter, rate of the potential cycling can be variable accordingly for different reactions and is expressed in mV/s units. The obtained voltammograms reveal information regarding the electrochemical potentials at which the oxidation and reduction processes occur, how fast these processes occur, the potential range over which the electrochemical system is stable and the degree of reversibility of the electrode reactions under study. The scan rate, switching potentials, as well as the magnitudes of the anodic peak current, cathodic peak current, anodic peak potential and cathodic peak potential are the most important parameters of cyclic voltammetry. Furthermore, CV reveals information regarding the stability of the product during multiple redox cycles.

In the dissertation, CV is used for two different purposes. First, CV is used to determine the redox for detective molecules. Second, this technique is used to study electrochemical supercapacitor properties of graphene based material. [Figure 2-1](#) shows the CV curves for (a) EDLS and redox reactions.

Cyclic voltammetry measures current with regard to applied voltage at a constant sweep rate, ( $v=dV/dT$ ), and is therefore a means of evaluating capacitance. As explained in Chapter I of this dissertation, the capacitance of a capacitor is defined by the relation  $C= dQ/dV$ , where V the voltage difference between the associated with accommodation of charge Q on the each plate. Since the charge actually is the integration of current over time range and can be calculates with the following [Equation 2-1](#):

$$Q = \int I dt \quad (2-1)$$

Where the current  $I$  is expressed in amperes (A), the charge Q is in coulombs(C) and time t is in seconds.

The capacitance can then be calculated through incorporating Equation 2-2 into the capacitance equation as follows;

$$C = \frac{dQ}{dV} = \int I \frac{dt}{dV} = I \frac{\Delta t}{\Delta V} = \frac{I}{v} \quad (2-2)$$

where  $I$  is the average current density (A) and  $v$  is the scan rate in V/s.

Ideally, a perfect capacitor response would be a rectangular shaped voltammogram. However, the resistance is unavoidable in real systems so most experimental data takes the shape of a parallelogram with irregular peaks. The plots obtained at different scan rates are often displayed on the same graph to demonstrate the rate of charging and discharging and discharging characteristics which corresponds to different power levels. Faster sweep rates indicate higher power levels. As expected, capacitance decreases with higher discharging frequencies. Voltammograms that depicts mirror images represents reversible and discharging profile while an irreversible process will have two separate charge and discharge profiles.

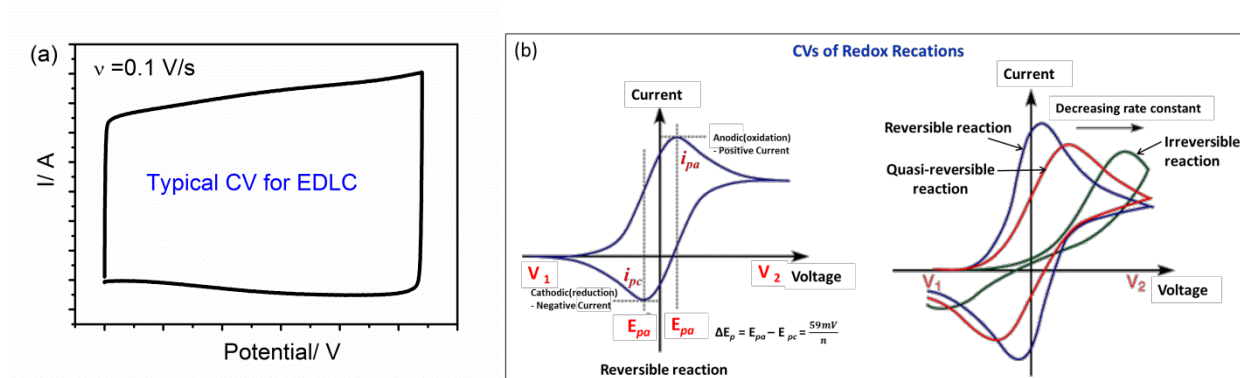


**Figure 2-1** The typical CV curves for (a) EDLS and (b) redox reactions.

The typical cyclic voltammograms recorded for a single electrode transfer reaction is shown in Figure 2-1(b), with the important peak parameters. Again the solution contains only a single electrochemical reactant. If a redox system remains in equilibrium throughout the potential scan, the redox process is said to be reversible (equilibrium requires that the surface concentrations of O and R, are maintained at the values required by the Nernst equation). The following parameter values are used to characterize the cyclic voltammogram of a reversible process[1]:

- the peak potential separation  $\Delta E_p (= E_{pc} - E_{pa}) = \frac{59mV}{n}$  at all scan rates at 25°C;
- the peak current ratio  $= i_{pa}/i_{pc} = 1$  at all scan rates;
- the peak current function  $i_p/v^{1/2}$  ( $v$  = scan rate) is independent of  $v$  (see equation for peak current)

The peak current is given by the equation:

$$i_p = (2.69 \times 10^5)n^{3/2}ACD^{1/2}v^{1/2} \quad (2-3)$$

where  $n$  is number of electrons transferred/molecule,  $A$  is electrode surface area ( $\text{cm}^2$ ),  $C$  is concentration ( $\text{mol cm}^{-3}$ ) and  $D$  is diffusion coefficient ( $\text{cm}^2 \text{s}^{-1}$ ). For a reversible process,  $E^o$  is given by the mean of the peak potentials. Departures from reversible behavior for a redox process are shown by variations of the above parameters from the values observed for reversible processes.

### 2.1.2 Constant Current Charge and Discharge

Another method to evaluate supercapacitor's specific capacitance is ESR through constant current charge and discharge technique. Charging or discharging the cell at constant results in a voltage response. The current integral,  $\int I dt$ , is therefore a measure of charge delivery, and power is then determined by the product  $I \times V$ , and energy by  $\frac{1}{2} Q \times V$ . If the EDLC is assumed to be a capacitance in series with an ESR can be determined by the ratio of voltage change to current change. This procedure is only accurate at low currents, however, and there is a significant departure from predicted behavior at higher currents.

### 2.1.3 Electrochemical Impedance Spectroscopy[2]

The use of complex-plane plot, or Nyquist plot, to represent the impedance behavior as a function of frequency has often been used to evaluate the frequency response of supercapacitors. In the complex-plane, the imaginary component,  $Z_2$ , is usually used to represent the capacitive parameter and the  $Z_1$  (the real component) represents the ohmic parameter. The two components are all studied under a certain frequency range. These kinds of plots usually consist of one or more semicircles in the complex plane, sometimes with the center of a semicircle depressed below the  $Z_1$  axis. The theoretical Nyquist plot of a supercapacitor consists of three regions which are dependent on the frequencies. At very high frequency, the supercapacitor behaves like a pure resistor. At low frequency, the imaginary part sharply increases and a vertical line is observed, indicating a pure capacitive behavior. In the middle frequency domain, the influence of the electrode porosity can be observed. When the frequency decreases, starting from the very high frequency, the signal penetrates deeper inside the porous structure of the electrode, then more and more electrode surface is available for the ion adsorption. This middle frequency range related to the electrolyte penetration, inside the porous structure of the high porosity electrodes, and this region is usually called Warburg curve.

## 2.2 Test Cell Configuration

Electrochemical characterizations of the electrode materials were performed using a two symmetric electrodes configuration with industry-level coin cell. Figure 2-2 shows a schematic of the test cell and fixture assembly. The two electrode test cell configuration was used because it provides the most accurate measure of a material's performance for electrochemical capacitors.[3]

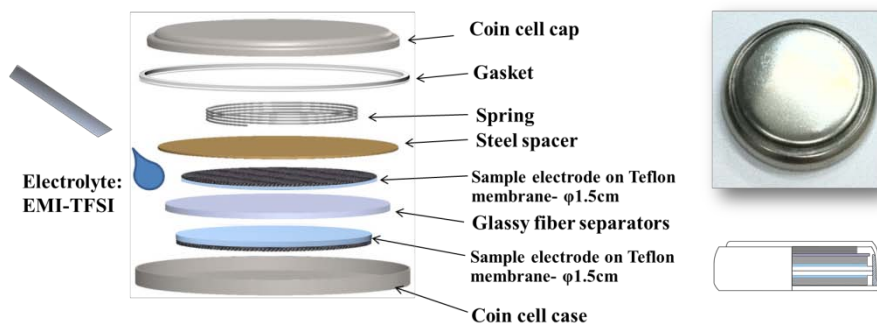


**Figure 2-2** Coin cell structure for coin cell test

## 2.3 Measurement Procedure

Charging current, potential ranges and methods for calculation also affect the results of the supercapacitor. The electrochemical performances of packaged supercapacitor include specific capacitance, energy density, power density, and life cycle testing. The energy density (Wh/kg) is determined by the specific capacitance of electrodes materials and electrochemical voltage windows. The power density of supercapacitor is determined by the equivalent series resistance (ESR). The ESR which can be measured by the electrochemical impedance spectroscopy is affected by all cell components including current collectors, electrodes, electrolyte, and separator. Specific capacitance of the a single electrode is the 4 times larger than the specific capacitance of the whole cell (Equation 2-4)

$$C_{sp} = 4 \times \frac{C}{m} \quad (2-4)$$

Where C is measured capacitance for the two-electrode cell and m is the total mass of the active material in both electrodes. Specific capacitance is best determined from constant discharge curves using Equation 2-5:

$$C = \frac{I}{dV/dt} \quad (2-5)$$

dV/dt calculated from the slope of the constant current discharge curve. Charging voltages for hybrid cells will depend upon electrode materials and electrolytes. The initial portion of a discharge curve exhibits an IR drop due to internal resistance and the rest of the curve will typically be linear for non-faradic materials such as carbon materials.

## 2.4 Summary of Test Method

A three-electrode system is very useful for determining the electrochemical properties of a single electrode. A two-electrode test system is the best construction which can mimics the real packaged

supercapacitor that can be used to characterize the energy density, power density and cycling property of a supercapacitor. For good signal to noise and to minimize measurement errors the test cell should have a capacity of over 0.25 Farad.

## References

1. Wang J. Analytical Electrochemistry; 2006.
2. Allen J. Bard LRF. Electrochemical Methods: Fundamentals and Applications 2000.
3. Stoller MD, Ruoff RS. Best practice methods for determining an electrode material's performance for ultracapacitors. Energy & Environmental Science 2010,3:1294-1301.

---

## Chapter 3

# Hybrid Graphene Electrodes for Supercapacitors of High Energy Density

---

### 3.1 Introduction

Supercapacitors have attracted significant attention recently due to their extraordinary high power density and long cycle life. They also bridge the power and energy gaps between traditional dielectric capacitors (which have high power output but low energy density) and batteries (which have high energy density but low power density). A major challenge for the development of supercapacitors has been to improve their energy density. Activated carbon (AC) has been the material of choice to fabricate the electrodes of supercapacitors for the past few decades.[1-3] However, AC-based supercapacitors have suffered a major setback that their energy density is still relatively low (typically 3-10 Wh kg<sup>-1</sup>) in comparison with best batteries which can offer energy density in the range 20- 150 Wh kg<sup>-1</sup>.

With the discovery and availability of carbon nanotubes (CNTs) and especially graphene, a new opportunity has appeared to improve the energy density of supercapacitors drastically owing to the extraordinary physical, chemical, and electrochemical properties of these nanostructured carbon structures.[4-8] For example, graphene offers superior chemical stability, large specific surface area (~2630 m<sup>2</sup> g<sup>-1</sup>), and a broad electrochemical window, which render it as a most attractive electrode material for supercapacitors with a theoretical electrochemical double layer capacitance of about 550 F g<sup>-1</sup>. [9]

Several interesting papers have been published during the past few years on utilizing graphene in supercapacitors. For example, Stoller et al. reported evaluation of supercapacitor electrodes made of a chemically modified graphene and specific capacitance of 135 F g<sup>-1</sup> and 99 F g<sup>-1</sup> was obtained in aqueous KOH and organic electrolyte, respectively [10]. Liu et al. reported a symmetric supercapacitor based on curved graphene nano-sheets which, when operated at a voltage of 4 V in an ionic liquid electrolyte, showed a high energy density of 85.6 Wh kg<sup>-1</sup> [11]. Very recently, El-Kady et al. used a standard LightScribe DVD optical drive to carry out reduction of graphite oxide films to produce graphene and the supercapacitor device made with the laser-reduced graphene exhibited high specific capacitance, ranging from 265 F g<sup>-1</sup> in organic electrolyte operated at 3 V to 276 F g<sup>-1</sup> in ionic liquid electrolyte operated at 4 V [12].

For high performance graphene supercapacitors, the desired key performance parameters for selected graphene are (i) high specific surface area, (ii) high intra- and inter-particle conductivity in porous graphene electrodes, and (iii) high electrolyte accessibility to the intra-pores in the graphene electrodes.[13] Among the various methods for preparation and processing of graphene, chemical reduction of graphene oxide is most promising owing to its low cost, easy operation, and scalability for mass production.[14] However, since the graphene nano-sheets tend to aggregate and restack through the van der Waals interactions during the reduction process, the effective specific surface area for access to the electrolyte is usually much lower

than its theoretical value of  $2630 \text{ m}^2 \text{ g}^{-1}$ . It is therefore of vital importance to prevent graphene from restacking in the process of fabrication of graphene electrodes. One idea is to use carbon nanotubes, especially single-walled carbon nanotubes, as spacers to prevent graphene from restacking and agglomerating. Attempts have been made to fabricate graphene electrodes with both multiwalled and single-walled carbon nanotubes and exciting results have been obtained with SWNTs. [15, 16] As one can easily imagine, if CNTs could be inserted into the interlayer space of graphene nano-sheets, restacking of graphene can be prevented and, at the same time, the insertion of CNTs can also create certain intra-pore space for the electrolyte to enter. In addition, due to the very high electrical conductivity of carbon nanotubes of  $10^4 \text{ S m}^{-1}$ , the internal electrical resistance of the graphene electrodes can also be reduced. As a result, we have recently developed a SWNT/graphene composite and the SWNT/graphene composite electrodes exhibited a specific capacitance of  $201 \text{ F g}^{-1}$  and high energy density of  $63 \text{ Wh kg}^{-1}$  in organic electrolyte at room temperature.[17]

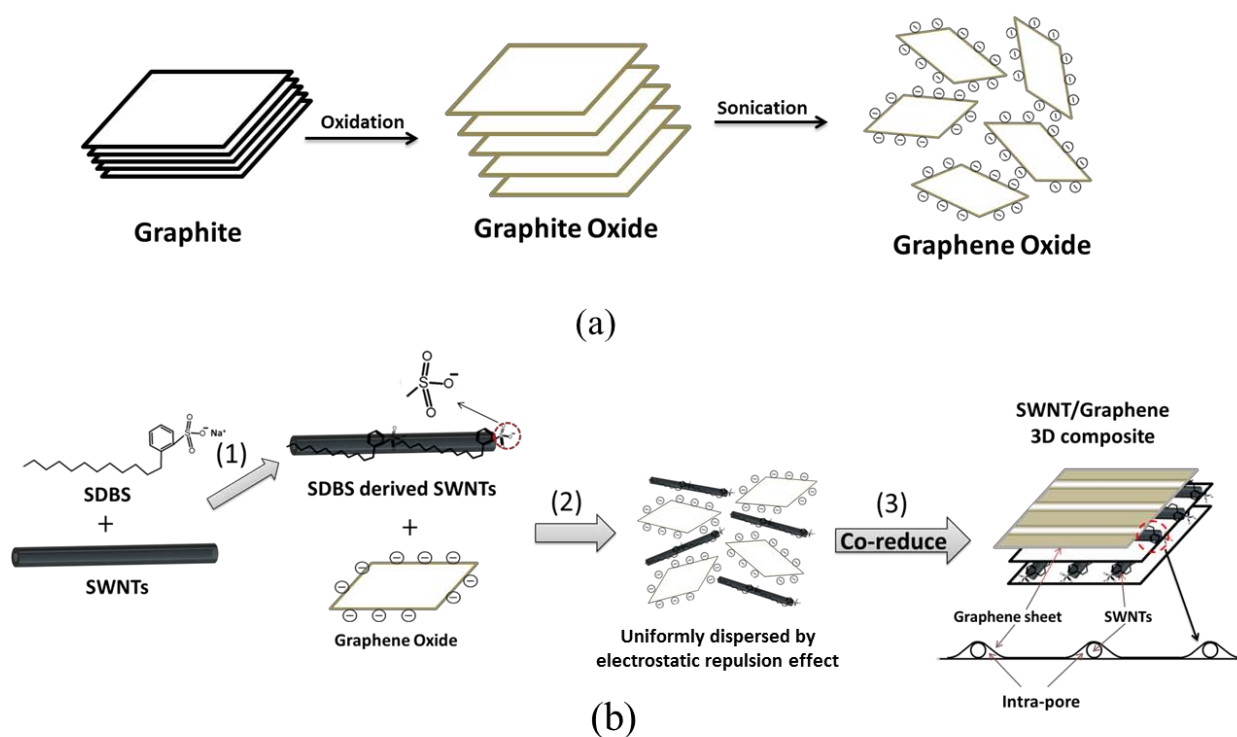


**Figure 3-1.** Schematic of chemical route for synthesis of graphene oxide and preparation of SWNT/graphene composite. (a) Oxidation of graphite to produce graphite oxide with greater interlayer spacing and exfoliation of graphite oxide in water by sonication to obtain GO colloids that is stabilized by electrostatic interactions. (b) Process of co-reduction of SWNT/GO to produce SWNT/graphene composite with SDBS surfactant.

In this work, to further improve the uniformity and electrochemical performance of the CNT/graphene composite, we develop a co-reduction process, in which a suspension of graphene oxide (GO) and SWNTs is reduced simultaneously by hydrazine. As illustrated in Figure 3-1a, in the suspension the GO sheets are negatively charged when they are dispersed in water, as a result of ionization of the carboxylic acid and phenolic hydroxyl groups that are known to exist on the GO surface during oxidation of graphite. The GO

suspension is colloidal.[18, 19] The uniform SWNT suspension was obtained by non-covalent functionalization with sodium dodecyl benzene sulfonate (SDBS) molecules. SWNTs are dispersed as individual tubules and the amount of adsorption corresponds to coating of individual tubule surface with SDBS [20], and this process makes the surface of SWNTs become negatively charged (Figure 3-1b-1). Therefore, GO and SDBS-functionalized SWNTs can be well dispersed by electrostatic repulsions to form a mono-dispersed suspension (Figure 3-1b-2). When this suspension is reduced by hydrazine, GO and SWNTs will deposit homogeneously, with which a uniform SWNT/graphene three-dimensional hybrid structure was obtained (Figure 3-1b-3). As the SWNTs are inserted into the interlayer space of graphene, buckling of otherwise flat graphene sheets will also likely occur and the restacking of graphene could therefore be effectively prevented. At the same time, intra-pores would be created to increase the specific surface area and the electrolyte ions would become more accessible to the electrode surface.

## 3.2 Experimental

### 3.2.1 Preparation of Co-Reduced SWNT/GO Composites

Graphene oxide (GO) was synthesized from graphite by a modified Hummers method. [21] Graphite and  $\text{NaNO}_3$  were first mixed together in a beaker. And,  $\text{H}_2\text{SO}_4$  then was added to the beaker with stirring in an ice water bath.  $\text{KMnO}_4$  was added last to the suspension slowly to avoid overheating. The color of the suspension would eventually become brown and distilled water and  $\text{H}_2\text{O}_2$  were then added and the color of the solution changed from brown to bright yellow. The suspension was treated ultrasonically to exfoliate graphite oxide particles to produce graphene oxide platelets. Last refinement was carried out by centrifuge to remove larger particles. The final GO sediments were dried in a vacuum and the GO appears as dark brown powders with a typical size of about  $10\mu\text{m}$ . Atomic force microcopy (AFM) measurement indicated that the GO nano-sheet was a monolayer with a thickness of about 0.8 nm.

The finished GO powders were then dispersed in distilled water by sonication. SWNTs were added to a sodium dodecylbenzene sulfonate (SDBS) water solution or water to obtain an SWNT suspension. Then, the GO and SWNT suspensions were mixed and sonicated to produce a homogeneous suspension. Hydrazine hydrate was finally added into the suspension for reduction to obtain SWNT/GO( $\text{H}_2\text{O}$ ) and SWNT/GO(SDBS) composites.

### 3.2.2 Materials Characterization

The morphologies and nanostructure of the graphene-based material were characterized using transmission electron microscopy (TEM, JEM-2100), scanning electron microscopy (SEM, JSM-7001F), and atomic force microscopy (AFM, Agilent's PicoScan). X-ray diffraction (XRD) was carried out using Rigaku RINT 2500 with  $\text{Cu K}\alpha$  radiation. Fourier transform infrared spectroscopy (FTIR) was recorded by SPECTRUM GX-Raman (Perkin Elmer). The specific surface area and pore size distribution were measured with Autosorb-1 (Quantachrome Instruments). All electrochemical characterization was performed using

BioLogic EC-Lab (VSP-300).

### 3.2.3 Structure and Evaluation of Graphene Supercapacitor

To compare the electrochemical performance of different graphene supercapacitors, graphene electrodes of almost the same weight were prepared and assembled into coin cells using (i) pure SWNTs, (ii) hydrazine reduced graphene, and (iii) co-reduced SWNT/graphene composite. The electrode material was first dispersed separately in ethanol and then the suspension was filtered onto a porous filter membrane (Hydrophilic, PTFE) by vacuum filtration. After vacuum drying, all electrodes were prepared by cutting the filtered films into circular disks. Ionic liquid (1-ethyl-3-methylimidazolium-bis (trifluoromethylsulfonyl) imide, EMI-TFSI) was used as electrolyte in this work. And the coin cell supercapacitors were assembled in a glove box.

### 3.3 Results and Discussion

The morphology of graphene oxide was shown in Figure 3-2 and Figure 3-3. The size of GO was about  $10\mu\text{m}$ , and AFM investigation indicated that the GO nano-sheet was monolayer (thickness =  $0.83\text{nm}$ ).

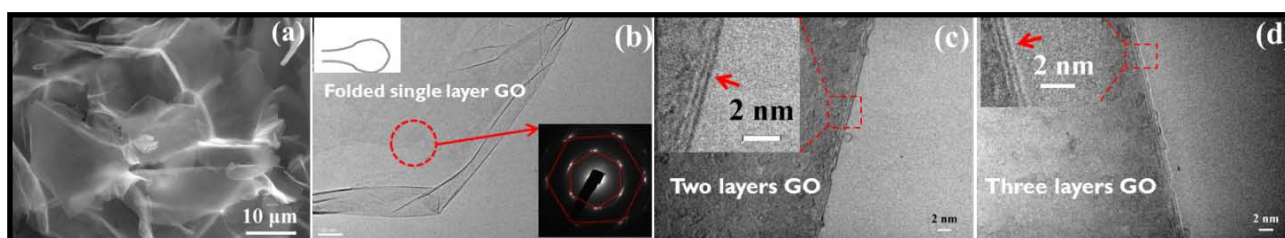


**Figure 3-2** SEM of GO powder (a); TEMs of folded single layer (b), two layers (c) and three layers GO (d)

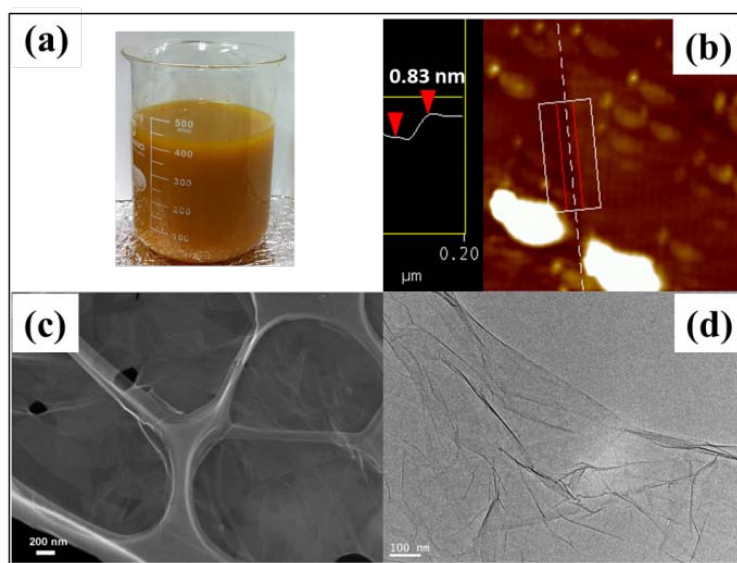


**Figure 3-3** Morphology of graphene oxide (GO). (a) Digital camera image of as prepared GO suspension, (b-d) AFM, SEM and TEM images of GO nano-sheets.

TEM morphologies of folded single layer, two layers and three layers GO and SEM morphology of GO powder was shown in [Figure 3-2](#). TEM investigation indicated that most of the GO nano- sheet were less than three layers.

In order to prepare a uniform and mono-dispersed SWNTs suspension, the SWNTs were dispersed at approximately 0.03wt % in water containing different concentrations of predissolved SDBS (0, 0.5, 1, 2wt %) with the aid of sonication. The dispersability was shown in [Figure 3-4](#). The SWNTs does not disperse at all in distilled water ([Figure 3-4 \(a\)](#)). In the 0.5 % SDBS solution, there were still some deposit existed ([Figure 3-4 \(b\)](#)). When the concentration of SDBS is greater than 1%, SWNTs can be dispersed well ([Figure 3-4 \(c, d\)](#)). Considering that too much SDBS may reduce the conductivity of the composite, 1% SDBS was used to disperse SWNTs powder. In this case, both well dispersed GO and SWNTs precursor (shown in [Figure 3-4 \(e\)](#)) and good conductivity of resulting GO/SWNTs (SDBS) co-reduce product could be obtained.

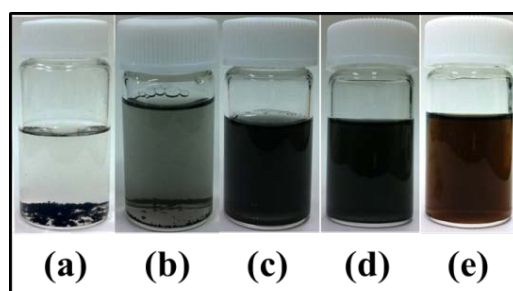


**Figure 3-4** Digital pictures of SWNTs dispersed in (a) water, (b) 0.5%, (c) 1% and (d) 2% SDBS water solution, and (e) GO and SWNTs 1% SDBS mixed water solution. All the dispersions were sonicated for 2h, and then stood for 1 day.

[Figure 3-5](#) shows the morphologies of co-reduced SWNT/GO composite. [Figure 3-5a and 3-5b](#) show the TEM and SEM images of co-reduced SWNT/GO composite with SWNTs pre-dispersed in H<sub>2</sub>O (termed SWNT/GO(H<sub>2</sub>O) hereafter). Since they do not disperse well in water, SWNTs often entangle to form bundles in the composite. We could also observe that graphene agglomerated, which made part of the graphene surface not accessible to the electrolyte. [Figure 3-5c and 3-5d](#) show the TEM and SEM images of co-reduced SWNT/GO composite with SWNTs pre-dispersed in water with 1% SDBS in solution (termed SWNT/GO(SDBS) hereafter). Negatively charged GO and SDBS functionalized SWNTs (also negatively charged) were well dispersed and a uniform suspension was formed. In the structure the SWNTs were in between the graphene sheets resulting in a homogeneous SWNT/graphene composite. In addition, buckling of graphene also occurred because of the intra-pores created between the graphene layers.

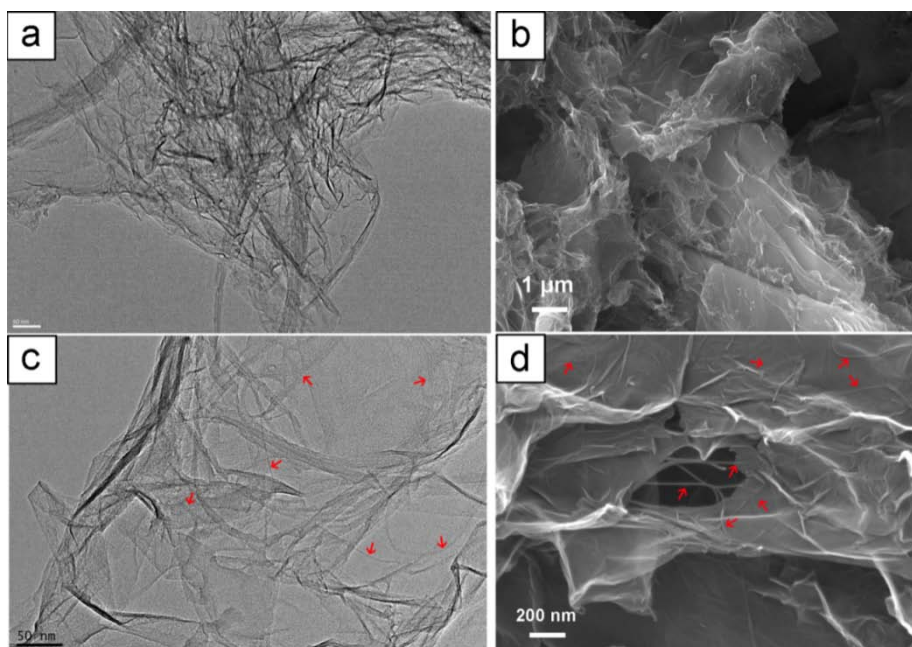


**Figure 3-5** Morphology and structure of SWNT/graphene composite. (a) TEM and (b) SEM image of co-reduced SWNT/graphene composite with SWNTs dispersed in water. Few SWNTs were observed to have formed SWNT/graphene composite. (c) TEM and (d) SEM image of co-reduced SWNT/graphene composite with SWNTs dispersed with SDBS. SWNTs were well dispersed and homogeneous SWNT/graphene composite was obtained. The red arrows indicate SWNTs.

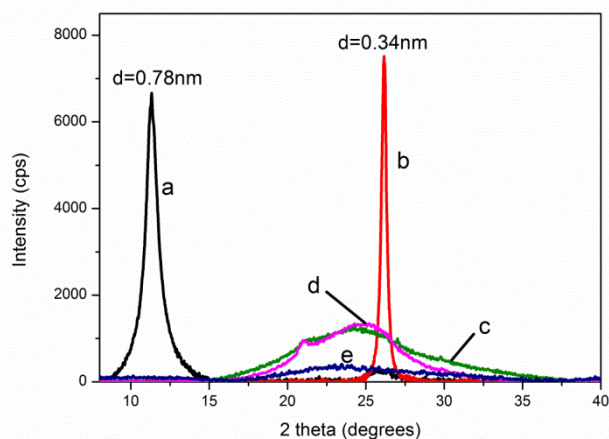


**Figure 3-6** XRD patterns of different samples. (a) Graphite oxide; (b) Graphite; (c) Hydrazine reduced graphene; (d) Co-reduced SWNT/GO( $H_2O$ ); and (e) Co-reduced SWNT/GO(SDBS).

Figure 3-6 shows the XRD patterns of (a) graphite oxide, (b) graphite, (c) hydrazine reduced graphene, (d) co-reduced SWNT/GO( $H_2O$ ), and (e) co-reduced SWNT/GO(SDBS). Graphite oxide showed a larger interlayer spacing (peak a,  $2\theta = 11.3^\circ$ ,  $d = 0.78$  nm) than that of graphite ( $d_{200} = 0.34$  nm). The increased planar spacing is because of the oxygen functional groups in graphite oxide and the water molecules held up in the interlayer spaces of the hydrophilic GO. In the XRD patterns of hydrazine reduced graphene and co-reduced SWNT/GO( $H_2O$ ) composite, the corresponding peak is at  $24 - 25^\circ$  due to an interlayer spacing of

0.35 – 0.37 nm. This spacing is much smaller than that of graphite oxide (0.78 nm), but closer to the (002) peak of graphite with  $2\theta = 26.2^\circ$  ( $d = 0.34$  nm), indicating restacking of graphene nano-sheets. On the other hand, in the case of co-reduced SWNT/GO(SDBS) composite, there is only a small broad peak appeared, suggesting that the GO powders were well dispersed with little restacking.

Nitrogen-adsorption and -desorption isotherms of SWNTs, hydrazine reduced graphene, and co-reduced SWNT/GO(SDBS) composite are shown in Figure 3-7a. Using these isotherms, the multipoint Brunauer-Emmett-Teller (BET) specific surface areas for SWNTs, hydrazine reduced graphene, and co-reduced SWNTs/GO(SDBS) composite were obtained as 442.0, 587.3, and 945.6  $\text{m}^2 \text{g}^{-1}$ . It should be noted that, the BET specific surface area of the co-reduced SWNT/GO(SDBS) composite is much larger than that of SWNTs and hydrazine reduced graphene. This indicates that the mono-dispersed SWNTs acted indeed as spacers between the graphene layers, thereby preventing their agglomeration and restacking, as revealed in Figure 3-5d. Based on the density functional theory (DFT) model, the pore size distribution of SWNTs, hydrazine reduced graphene, and co-reduced SWNT/GO(SDBS) composite is given in Figure 3-7b. The SWNT powders showed several wide peaks in the distribution, attributed to the SWNT bundles of various sizes. Pores from 1.4 to 2.0 nm in half width were observed in hydrazine graphene, which were due to graphene agglomeration. In the co-reduced SWNT/GO(SDBS) composite, there are three major pores with half width of 1.4, 2.3, and 3.8 nm. These data suggest that the SWNTs as spacers were inserted into the graphene layers, increasing the pore size and contributing to electrolyte accessibility and rate capability.

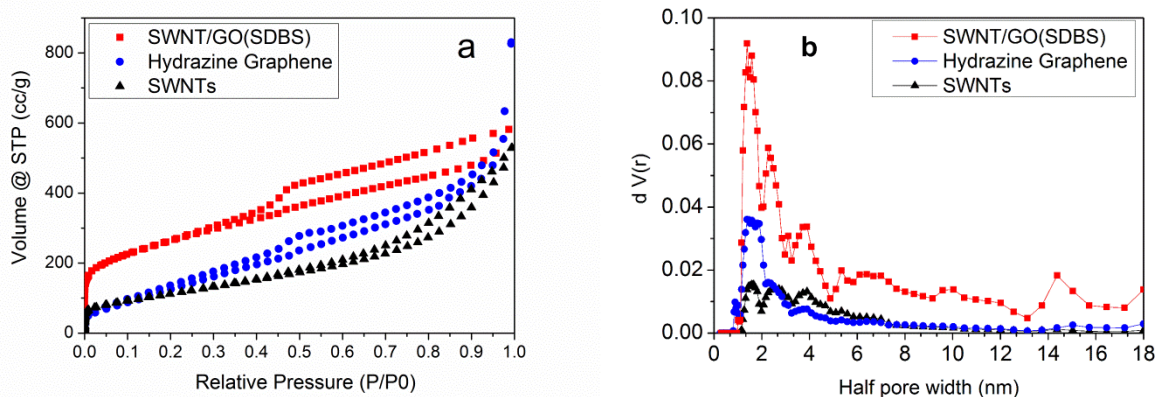


**Figure 3-7** (a) Nitrogen adsorption and desorption isotherms and (b) pore size distribution of SWNTs (black), hydrazine reduced graphene (blue), and co-reduced SWNT/GO(SDBS) composite (red).

Figure 3-8 shows the Fourier transform infrared (FTIR) spectra of (a) GO, (b) hydrazine reduced graphene, (c) co-reduced SWNT/GO( $\text{H}_2\text{O}$ ) composite, and (d) co-reduced SWNT/GO(SDBS) composite. The GO sample shows a strong peak at  $1597 \text{ cm}^{-1}$  (skeletal vibrations from graphitic domains) due to the aromatic C=C bonding. The peaks of GO at  $1725 \text{ cm}^{-1}$  (C=O stretching vibrations from carbonyl and carboxylic groups),  $1425 \text{ cm}^{-1}$  (C-O-C and C-OH stretching vibrations),  $1256 \text{ cm}^{-1}$  (epoxide groups), and  $1060 \text{ cm}^{-1}$  (C-O stretching vibrations), testifying the presence of many oxygen-containing functional groups. In comparison to the FTIR spectrum of GO, the peaks at 1725, 1256 and  $1060 \text{ cm}^{-1}$  in other samples almost

diminished. This is because the C-O-C, C=O, and O-C=O were removed by hydrazine hydrate, which means GO and SWNT hybrid suspensions can be sufficiently reduced independent of the presence of SDBS. The peak at  $1425\text{ cm}^{-1}$  did not disappear, indicating that most C-OH groups were still present and could not be reduced by hydrazine. The peaks in co-reduced SWNT/GO(SDBS) composite at about  $1008$  and  $820\text{ cm}^{-1}$  are due to the remaining SDBS molecules.

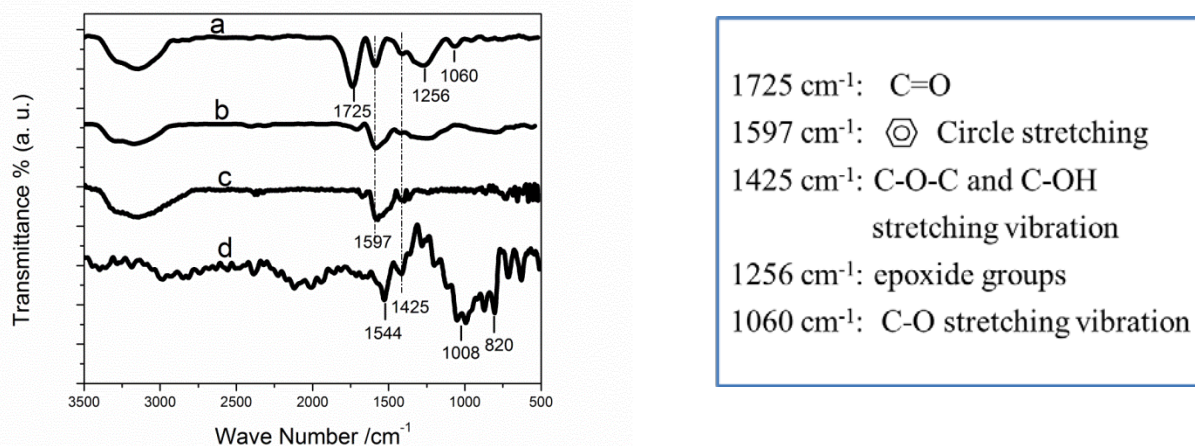


**Figure 3-8** (Left) FTIR spectra of (a) GO, (b) Hydrazine reduced graphene, (c) Co-reduced SWNT/GO( $\text{H}_2\text{O}$ ) composite, and (d) Co-reduced SWNT/GO(SDBS) composite; (Right) Correspondence of peak position and oxygen groups.

Electrochemical characterizations of the electrode materials were performed using a two symmetric electrodes configuration with industry-level coin cell. **Figure 3-9** shows a schematic of the test cell and fixture assembly. The two electrode test cell configuration was used because it provides the most accurate measure of a material's performance for electrochemical capacitors. [22]

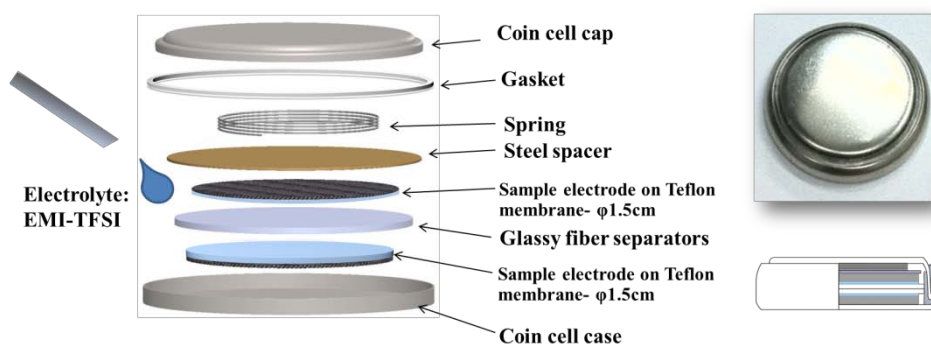


**Figure 3-9** Schematic of test cells assembly

Cyclic voltammetry (CV) curves were acquired at scanning rate from  $10$  to  $100\text{ mV/s}$  and electrochemical impedance spectroscopy (EIS) was conducted using a sinusoidal signal with mean voltage of  $0$  and amplitude of  $10\text{ mV}$  over a frequency range of  $100\text{ kHz}$  to  $10\text{ mHz}$ . The specific capacitance  $C_{sp}$ , energy density  $E_{density}$ , and power density  $P_{density}$  were calculated from galvanostatic charge/discharge curves according to

$$C_{sp} = \frac{2I}{m(dV/dt)}, \quad (1)$$

$$E_{density} = \frac{1}{8} C_{sp} V_{drop}^2, \quad (2)$$

$$P_{density} = \frac{V_{drop}^2}{8mR_{ESR}}, \quad (3)$$

where  $dV/dt$  is calculated from the slope of the discharge curves,  $R_{ESR}$  is the equivalent series resistance,  $m$  is the weight of each electrode, and  $V_{drop}$  is the drop voltage.

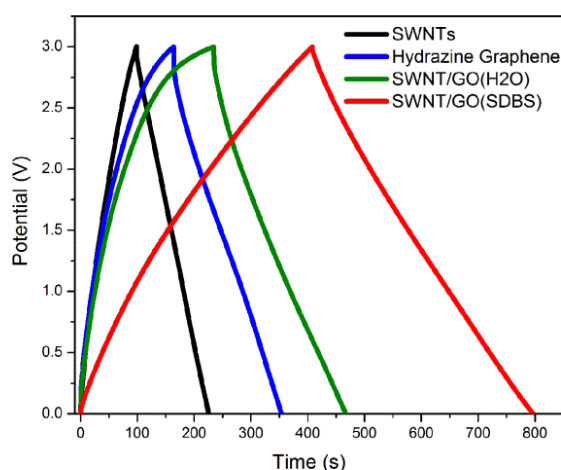


**Figure 3-10** Galvanostatic charge/discharge curves up to 3.0 V of different electrodes at a constant current density of 320 mA g<sup>-1</sup> in ionic liquid (EMI-TFSI) electrolyte.

Galvanostatic charge/discharge curves of symmetric supercapacitors based on pure SWNTs (black), hydrazine reduced graphene (blue), co-reduced SWNT/GO(H<sub>2</sub>O) composite (green), and co-reduced SWNT/GO(SDBS) composite (red) at a constant current density of 320 mA g<sup>-1</sup> in the potential range between 0 and 3 V are all shown in Figure 3-10. It can be seen that the curves are nearly linear and symmetrical, showing typical and characteristic capacitive behavior. Only a very small voltage drop was observed, indicating that the electrodes had low internal resistance. In addition, the charge–discharge duration for co-reduced composites containing SWNTs was longer than that for hydrazine reduced graphene and pure SWNTs, indicating a higher specific capacitance. The increase in the specific capacitance of co-reduced composites is attributed to the functions of SWNTs acting as spacers for graphene layers to prevent the restacking and therefore improving the accessibility for electrolyte ions. When compared the co-reduced SWNT/GO(H<sub>2</sub>O) and SWNT/GO(SDBS) electrodes, the SWNT/GO(SDBS) electrodes exhibited higher specific capacitance and higher energy density, indicating that the uniformity of SWNT/graphene composites is crucial to the supercapacitor performance. In the co-reduced GO-SWNT(H<sub>2</sub>O) electrode, there are still many restacked agglomerates of graphene and SWNT bundles and therefore the performance had limited improvement compared with pure graphene electrode. The specific capacitance and energy density

obtained from galvanostatic charge/discharge curves for (i) SWNTs, (ii) hydrazine reduced graphene, (iii) co-reduced SWNT/GO(H<sub>2</sub>O) composite, and (iv) co-reduced SWNT/GO(SDBS) composite, are 55, 86, 110, and 166 F g<sup>-1</sup>. The corresponding energy densities are 17, 24, 26, and 50 Wh kg<sup>-1</sup>.

Figure 3-11 shows the Nyquist plots of the EIS data of supercapacitors with (i) pure SWNTs (black), (ii) hydrazine reduced graphene (blue), and (iii) co-reduced SWNT/GO(SDBS) (red) electrodes. The devices display nearly a pure capacitive behavior. A semicircle in the high frequency region and a straight line in the low frequency region are observed in all samples. The high frequency semicircle region has been observed in all carbon-based supercapacitors, which is related to the electric resistance within the electrode material. We can observe that the semicircle region for SWNTs is smaller than that for hydrazine reduced graphene, showing good conductivity of SWNTs. We can also find that the semicircle region for co-reduced SWNT/GO composite is smaller than that for hydrazine reduced graphene, indicating that the addition of SWNTs lowered the interlayer resistance of graphene sheets, therefore also acting as conductive binder. The magnitude of the equivalent series resistance (ESR) obtained from the intercept on the horizontal axis for SWNTs, hydrazine reduced graphene, and co-reduced SWNT/GO(SDBS) composite are 5.4, 10.6, and 8.5 Ω. The straight line in low frequency region of the co-reduced composite is shorter than that for SWNTs and graphene, indicating an enhanced access of electrolyte ions to the graphene surface, which is attributed to the insertion of SWNTs between graphene sheets.

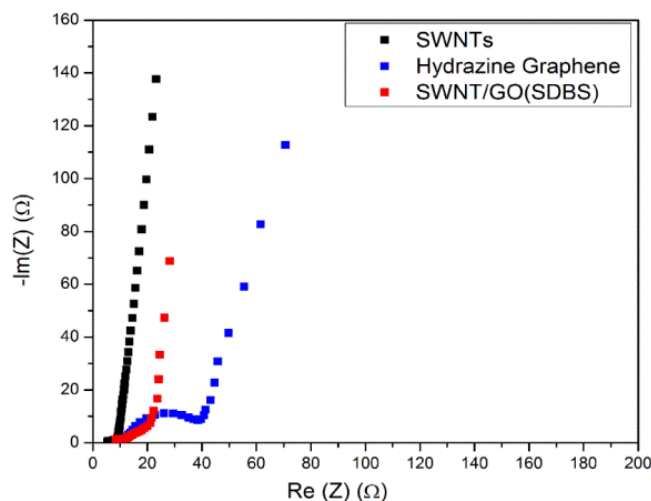


**Figure 3-11** Nyquist plots of EIS data for SWNTs (black), hydrazine reduced graphene (blue), and co-reduced SWNT/GO(SDBS) (red) composite-based supercapacitors, using a sinusoidal signal with mean voltage of 0 V and amplitude of 10 mV over a frequency range of 100 kHz to 10mHz.

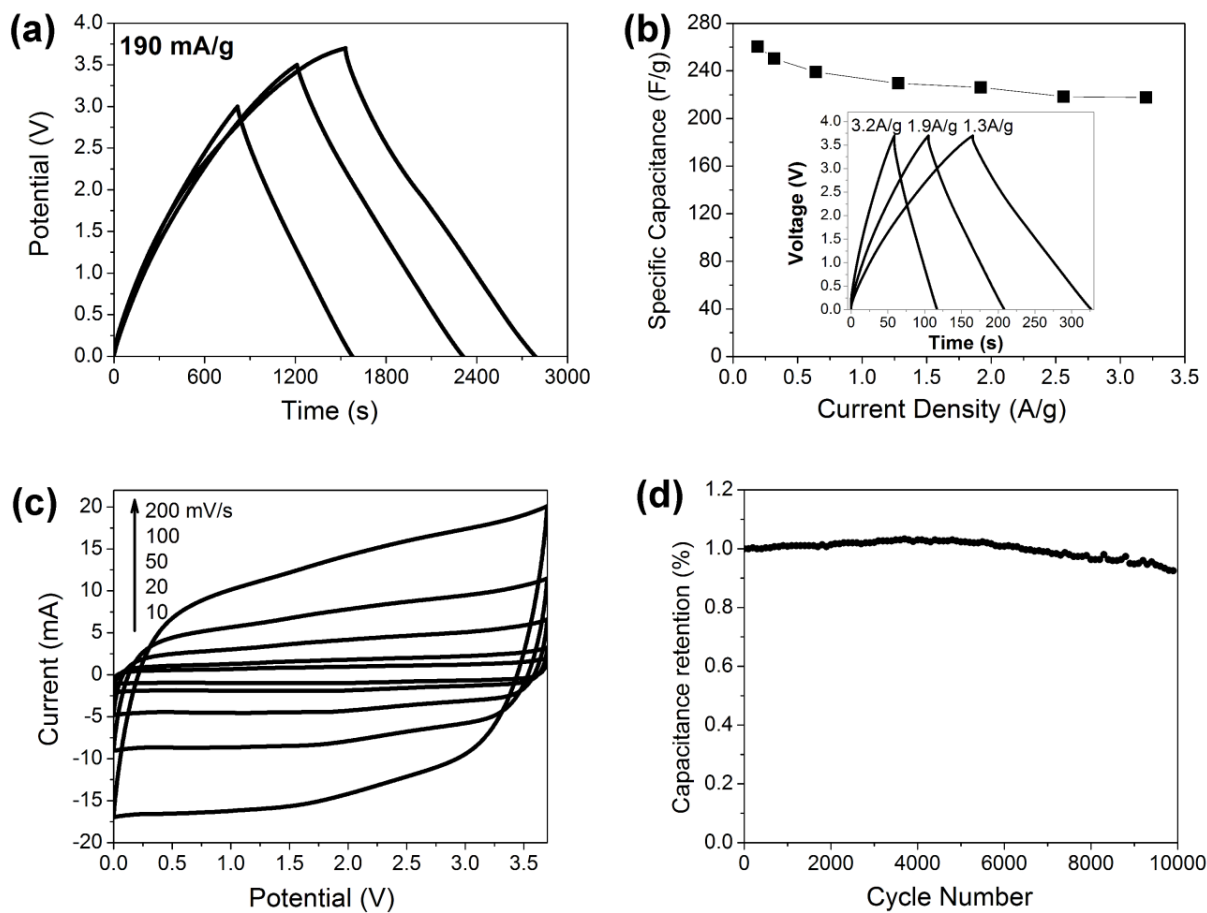


**Figure 3-12** Evaluation of supercapacitor with co-reduced SWNT/GO(SDBS) composite electrodes. (a) Galvanostatic charge/discharge curves operated at current density of 190 mA g<sup>-1</sup>, in the potential ranges of 0 to 3.0, 3.5 and 3.7 V. (b) Stack capacitance calculated from galvanostatic curves as a function of the charge/discharge current density (Inset is galvanostatic charge/discharge curves for SWNT/GO(SDBS) supercapacitor operated under different current density). (c) CV curves at scan rate of 10, 20, 50, 100, and 200 mV s<sup>-1</sup>. (d) Cycling stability of the device in 10,000 cycles.

We also tested the cyclic stability of the supercapacitor with SWNT/GO(SDBS) electrodes. The galvanostatic charge/discharge curves for the co-reduced SWNT/GO(SDBS) graphene supercapacitor at a constant current density of 190 mA g<sup>-1</sup> in the potential ranges between 0 and 3.0, 3.5, and 3.7 V are shown in Figure 3-12a. The charge/discharge curves are nearly linear and symmetrical. The specific capacitance and energy density of the co-reduced SWNT/GO(SDBS) composite at current density of 190 mA g<sup>-1</sup> and potential of 3.7 V are 261 F g<sup>-1</sup>. The corresponding energy density and power density are 123 Wh kg<sup>-1</sup> and 255 kW kg<sup>-1</sup>, respectively. The stack capacitance of a composite electrode is calculated from galvanostatic curves as a function of the applied charge/discharge current density is given in Figure 3-12b. This electrode shows a high rate capability as it continues to show high capacitance of 218 F g<sup>-1</sup> even when the current density was increased to 3.2 A g<sup>-1</sup>. The SWNT/GO(SDBS) composite retained 84% of its capacitance when the current density increased from 0.19 to 3.2 A g<sup>-1</sup>.

The CV curves for the co-reduced SWNT/GO(SDBS) composite at different scan rate in the voltage range of 0 to 3.7V are shown in [Figure 3-12c](#). Even at the scan rate of  $100\text{mV s}^{-1}$ , the CV curve remained rectangular, indicating excellent capacitive characteristics. When the scan rate was increased to  $200\text{mV s}^{-1}$ , a CV curve with small oblique deformation was observed because of the relatively large resistance of ionic liquid electrolyte at high charging rate limited by ion diffusivity in the electrolyte. The stability of the co-reduced SWNT/GO(SDBS) graphene supercapacitor was also evaluated by conducting galvanostatic charge–discharge measurements for 10,000 cycles at a constant current of 2 mA in the potential range 1.0 to 3.7 V, which is shown in [Figure 3-12d](#). The results indicate that the supercapacitor exhibited an excellent cycle life. There was no decay in capacitance observed in the first 5,000 cycles. Even after 10,000 cycles, 94% of the electrode capacitance was retained, demonstrating long cycle life and stability.

### 3.4 Conclusions

A process of co-reduction has been established and demonstrated to produce SWNT/graphene composite with a three-dimensional network structure for applications in graphene supercapacitors. High specific capacitance of  $261\text{ F g}^{-1}$  and energy density of  $123\text{ Wh kg}^{-1}$  have been obtained for the graphene supercapacitors at potential 3.7 V using ionic liquid electrolyte. We ascribe these improvements to (i) increase in the specific surface area of the co-reduced composite due to the spacer effect of SWNTs and that the resulted intra-pore space offers better electrolyte accessibility to the graphene sheets and (ii) increase of electrical conductivity owing to the SWNT conductive binder. The SWNT/graphene supercapacitor of high specific capacitance and energy density would have promising applications energy storage such as in hybrid vehicles and electrical vehicles.

### References

1. Kierzek K, Frackowiak E, Lota G, Gryglewicz G, Machnikowski J. Electrochemical capacitors based on highly porous carbons prepared by KOH activation (vol 49, pg 515, 2004). *Electrochimica Acta* 2004,49:1169-1170.
2. Raymundo-Pinero E, Kierzek K, Machnikowski J, Beguin F. Relationship between the nanoporous texture of activated carbons and their capacitance properties in different electrolytes. *Carbon* 2006,44:2498-2507.
3. Endo M, Maeda T, Takeda T, Kim YJ, Koshiba K, Hara H, et al. Capacitance and pore-size distribution in aqueous and nonaqueous electrolytes using various activated carbon electrodes. *Journal of the Electrochemical Society* 2001,148:A910-A914.
4. Kim B, Chung H, Kim W. High-performance supercapacitors based on vertically aligned carbon nanotubes and nonaqueous electrolytes. *Nanotechnology* 2012,23.
5. Kaempgen M, Chan CK, Ma J, Cui Y, Gruner G. Printable Thin Film Supercapacitors Using Single-Walled Carbon Nanotubes. *Nano Letters* 2009,9:1872-1876.
6. Xu B, Wu F, Chen RJ, Cao GP, Chen S, Zhou ZM, et al. Highly mesoporous and high surface area carbon: A high capacitance electrode material for EDLCs with various electrolytes. *Electrochemistry Communications* 2008,10:795-797.

7. Geim AK, Novoselov KS. The rise of graphene. *Nat Mater* 2007,6:183-191.
8. Park S, Ruoff RS. Chemical methods for the production of graphenes. *Nat Nano* 2009,4:217-224.
9. Vivekchand S, Rout C, Subrahmanyam K, Govindaraj A, Rao C. Graphene-based electrochemical supercapacitors. *Journal of Chemical Sciences* 2008,120:9-13.
10. Stoller MD, Park S, Zhu Y, An J, Ruoff RS. Graphene-Based Ultracapacitors. *Nano Letters* 2008,8:3498-3502.
11. Liu C, Yu Z, Neff D, Zhamu A, Jang BZ. Graphene-Based Supercapacitor with an Ultrahigh Energy Density. *Nano Letters* 2010,10:4863-4868.
12. El-Kady MF, Strong V, Dubin S, Kaner RB. Laser Scribing of High-Performance and Flexible Graphene-Based Electrochemical Capacitors. *Science* 2012,335:1326-1330.
13. Wang G, Zhang L, Zhang J. A review of electrode materials for electrochemical supercapacitors. *Chem Soc Rev* 2012,41:797-828.
14. Stankovich S, Dikin DA, Piner RD, Kohlhaas KA, Kleinhammes A, Jia Y, et al. Synthesis of graphene-based nanosheets via chemical reduction of exfoliated graphite oxide. *Carbon* 2007,45:1558-1565.
15. Yu DS, Dai LM. Self-Assembled Graphene/Carbon Nanotube Hybrid Films for Supercapacitors. *Journal of Physical Chemistry Letters* 2010,1:467-470.
16. Kim YS, Kumar K, Fisher FT, Yang EH. Out-of-plane growth of CNTs on graphene for supercapacitor applications. *Nanotechnology* 2012,23.
17. Cheng Q, Tang J, Ma J, Zhang H, Shinya N, Qin LC. Graphene and carbon nanotube composite electrodes for supercapacitors with ultra-high energy density. *Phys Chem Chem Phys* 2011,13:17615-17624.
18. Lerf A, He H, Forster M, Klinowski J. Structure of Graphite Oxide Revisited. *The Journal of Physical Chemistry B* 1998,102:4477-4482.
19. Szabó T, Berkesi O, Forgó P, Josepovits K, Sanakis Y, Petridis D, et al. Evolution of Surface Functional Groups in a Series of Progressively Oxidized Graphite Oxides. *Chemistry of Materials* 2006,18:2740-2749.
20. Utsumi S, Kanamaru M, Honda H, Kanoh H, Tanaka H, Ohkubo T, et al. RBM band shift-evidenced dispersion mechanism of single-wall carbon nanotube bundles with NaDDBS. *Journal of Colloid and Interface Science* 2007,308:276-284.
21. Hummers WS, Offeman RE. Preparation of Graphitic Oxide. *Journal of the American Chemical Society* 1958,80:1339-1339.
22. Stoller MD, Ruoff RS. Best practice methods for determining an electrode material's performance for ultracapacitors. *Energy & Environmental Science* 2010,3:1294-1301.

---

## Chapter 4

# Graphene-Carbon Nanotube Composite Aerogel for Selective Detection of Uric Acid

---

### 4.1 Introduction

Nanostructured carbon has been widely used in electro-analysis and electro-catalysis. For example, carbon nanotubes (CNTs) have shown excellent performance in biosensors, chemical sensors, and biofuel cells.[1, 2] CNT-based electrodes also showed electro-catalytic properties in the oxidation/reduction of a wide variety of compounds.[3] CNTs are very useful for electrochemical sensing because of their high surface area and rigid structure, which enabled construction of truly “nanoarchitectonic” electrodes.[4]

Graphene has attracted significant research interest in recent years. Its intriguing physicochemical properties, such as a large specific surface area (theoretically 2630 m<sup>2</sup>/g for single-layer graphene),[5] extraordinary electronic properties and electron transport capabilities,[6] superior chemical stability, [5] excellent thermal and electrical conductivities,[7, 8] made possible many applications in electrochemistry (chemical sensors, biosensors, supercapacitors, and batteries[9-11]). For example, in electrochemical sensing field, the high surface area of graphene sheets can give rise to high densities of attached analytic molecules, which in turn can facilitate high sensitivity and device miniaturization. Facile electron transfer between graphene and redox species opens up opportunities for sensing strategies based on direct electron transfer rather than mediation. Therefore, this 2D nanomaterial has already revealed potential applications in electrochemistry, and remarkably rapid progress in this area has already been made.[12] A number of experimental methods have been developed for preparation of graphene, including mechanical exfoliation, chemical vapor deposition (CVD), hydrothermal synthesis, and chemical oxidation-reduction.[13] Hydrothermal synthesis is an efficient and non-toxic method for large-scale production without using any chemical reagents or catalysts. However, graphene sheets tend to aggregate irreversibly through the strong  $\pi$ - $\pi$  interactions during the reduction process, thereby decreasing the effective specific surface area. One feasible proposal has been to use spacers to avoid or reduce the restacking and agglomeration of graphene. On the other hand, it would apparently be a better choice if the selected spacers could also contribute to the specific surface area, stability, and reactivity of the electrode material and structure.

Keeping the above in view, we describe the preparation and processing of graphene and single-walled carbon nanotubes (SWNTs) composite (hydrothermal G/S) by a hydrothermal method, where the SWNTs are connected with graphene and also inserted into the interlayer space between graphene sheets to reduce restacking of graphene. And this composite has also been explored for a novel uric acid (UA) biosensing application employing an electrochemical technique. Uric acid is an important analyte of clinical interest

(normal level in serum 4.0- 8.8 mg/dL, its early detection can be helpful to prevent various diseases like kidney stone, gout, diabetes and cardiovascular disease [14, 15]. The current detection methods of UA include enzymatic-based assay,[16] capillary electrophoresis,[17] high performance liquid chromatography [18] and electrochemical technique[19]. Among those methods, the electrochemical method is the most rapid, cheap and convenient one. But one of the major problems in biological determination of UA comes from electrochemical interferences such as ascorbic acid (AA) and dopamine (DA), which have a similar oxidation potential at normal electrodes. In this work, a novel hydrothermal G/S composite modified glassy carbon electrode (GCE) was fabricated for the selective detection of UA.

## 4.2 Experimental

### 4.2.1 Hydrothermal Synthesis of Graphene/SWNT Composite

Graphene oxide (GO) was obtained from graphite by a modified Hummers-Offeman method, which was developed and used in chapter three for supercapacitor applications. Atomic force microscopy (AFM) measurement indicated that the GO nano-sheets were mostly of a monolayer structure with thickness of about 0.8 nm.

In order to remove the catalyst impurities, 50 mg SWNTs were sonicated for 5 hours in 200 ml of an acid mixture (100 ml 48 % HF and 100 ml 98 % HNO<sub>3</sub>, in the presence of SDS). The resulting dispersion was filtered and rinsed twice with 200 ml deionized water of pH 12 (adjusted by addition of sodium hydroxide), followed by rinsing with 800 ml methanol and then vacuum dried at 100 °C for 16 hours. The product is termed as a-SWNTs hereafter.[20]

Solutions of GO and a-SWNTs with respective concentration of 1 mg ml<sup>-1</sup> and 0.25 mg ml<sup>-1</sup> were mixed together and then sealed in a 200 ml Teflon-lined autoclave for 4 hours at 180 °C to obtain hydrothermal graphene-SWNT composite (hydrothermal G/S) hydrogel after it was freeze dried for 48 hours. For comparison studies, hydrothermally reduced graphene oxide (hydrothermal G) without adding a-SWNTs was also prepared by the same process.

In the synthetic process of hydrothermal G/S composite (Figure 4-1), GO and a-SWNTs were both negatively charged when they were dispersed in water, as a result of ionization of the carboxylic acid and phenolic hydroxyl groups that are known to exist on the GO sheets, SWNT tips, and SWNT surface during oxidation. Therefore, GO and a-SWNTs can be well dispersed by electrostatic repulsions. When this suspension is reduced by hydrothermal treatment, there are several possible reactions to take place between GO and SWNTs: (1) elimination of OH and H can occur on the edge sites of graphene, resulting the recovery of  $\pi$ -conjugation, which believed to be analogous to the H<sup>+</sup>-catalyzed dehydration of alcohol [21]; (2) in the meanwhile, intermolecular dehydration can occur on the edges or basal planes of graphene and tips or surface of SWNTs by cross-linking of hydroxyl and carboxylic groups; and (3) carbon dioxide is released during thermal treatment due to the reduction of linearly clustered epoxy groups and leaves vacancies and topological defects on the carbon plate.[22] These three factors together with the  $\pi$ -stacking of graphene

sheets and SWNTs resulted in successful production of the hydrothermal G/S composite.

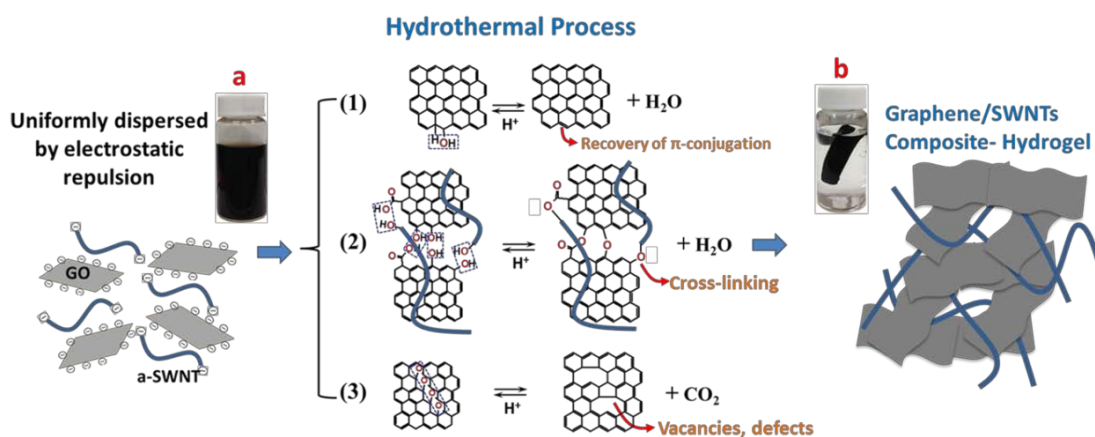


**Figure 4-1** Mechanism of formation for hydrothermal reduction of graphene/SWNT composite. Inset a shows photograph of GO and a-SWNT dispersion and inset b shows photograph of hydrothermal G/S composite hydrogel in water.

#### 4.2.2 Characterization

Morphology and structure of the material were characterized using transmission electron microscopy (TEM; JEOL JEM-2100, operated at 90 kV), scanning electron microscopy (SEM, JEOL JSM-7001F), and atomic force microscopy (AFM, Agilent PicoScan). X-ray diffraction (XRD) was carried out using Rigaku RINT 2500 with  $\text{Cu K}_\alpha$  radiation source. The specific surface area and pore size distribution were measured with AUTOSORB-1 (Quantachrome Instruments).

#### 4.2.3 Electrochemical Measurements

Electrochemical measurements were performed using an Ivium CompactStat (Ivium Technologies B.V.). Bare or modified glassy carbon electrode (GCE) of 3 mm in diameter was used as the working electrode, platinum wire as the counter electrode, and saturated calomel electrode (SCE) as the reference electrode. GCEs were polished with alumina slurry (0.05 and  $0.3\mu\text{m}$ ) on a polishing cloth, then cleaned in acetone and distilled water bath with sonication for 5 minutes and finally rinsed with doubly distilled water. The clean electrode was dried under an infrared lamp. 10 mg of a-SWNTs, hydrothermal G, and hydrothermal G/S composite aerogel were dispersed for 30 min with the aid of ultrasonic agitation in 10 ml water to produce a solution with concentration of  $1\text{ mg ml}^{-1}$ . An a-SWNT modified electrode (a-S/GCE), hydrothermal G modified electrode (H-G/GCE), and Hydrothermal G/S composite modified electrode (H-G/S/GCE) were prepared by dropping  $4\mu\text{L}$  of the solution with a finnpipette on the GCE and then heated under an IR lamp to remove the liquid solution.

### 4.3 Results and Discussion

The hydrothermal G/S composite has a well-defined and interconnected three-dimensional porous network as observed by SEM and TEM in the structure of its freeze-dried aerogel, shown in Figure 4-2. The

SWNTs are inserted into the interlayer space of graphene and restacking of graphene could therefore be effectively prevented. At the same time, intra-pores would be created to increase the specific surface area and the analytic molecules would become more accessible to the electrode surface. Nitrogen-adsorption and -desorption isotherms are shown in Figure 4-3(a). Using these isotherms, the multipoint Brunauer-Emmett-Teller (BET) specific surface areas of a-SWNTs, hydrothermal G, and hydrothermal G/S composite were obtained as 442, 483, and 656  $\text{m}^2 \text{g}^{-1}$ , respectively. The BET specific surface area of the hydrothermal G/S composite is much larger than that of a-SWNTs and hydrothermal G. This fact indicates that the well-dispersed SWNTs acted indeed as spacers between the graphene layers, reduced the restacking of graphene sheets, and helped to produce a three-dimensional network structure with intra-pores. The pore size distribution obtained from density functional theory (DFT) model is shown in the inset of Figure 4-3(b). Compared with hydrothermal G, pores with diameter of 3.8 nm in the hydrothermal G/S composite were increased significantly, which can also contribute to the “spacer” effect of SWNTs.

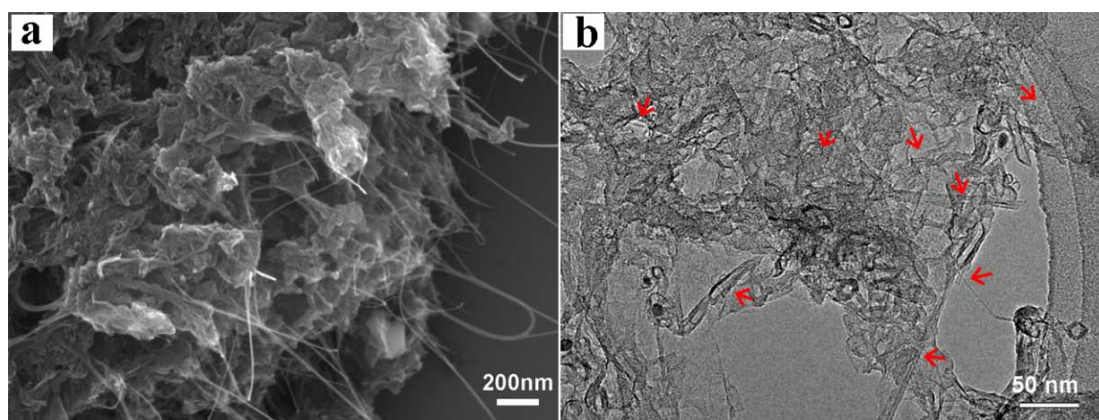


**Figure 4-2** (a) SEM and (b) TEM image of hydrothermal G/S composite. Red arrows indicate SWNTs.

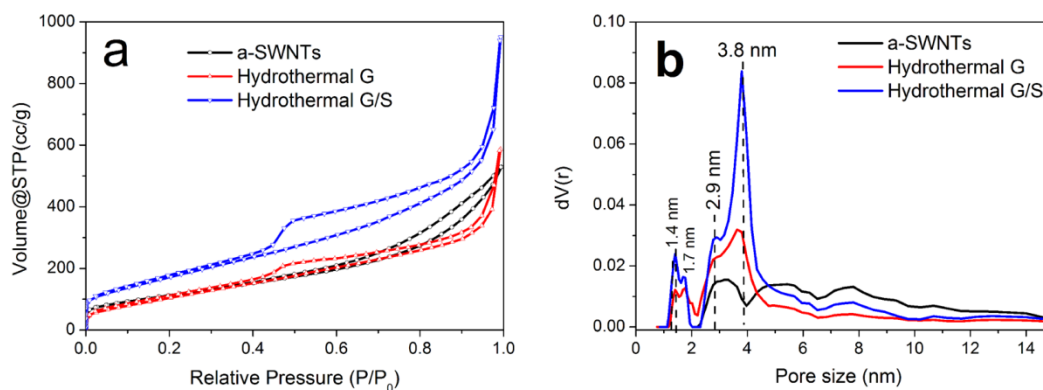


**Figure 4-3** (a) Nitrogen-adsorption and -desorption isotherms and (b) DFT pore-size distribution of a-SWNTs (black), hydrothermal G (red), and hydrothermal G/S composite (blue).

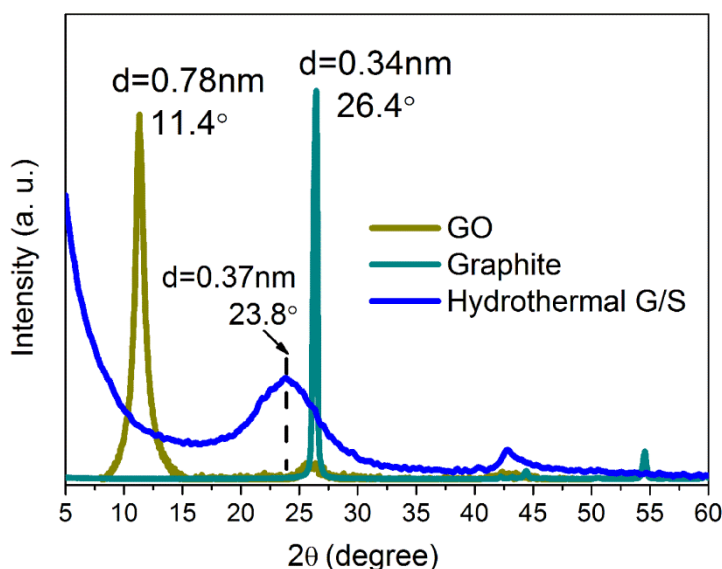


**Figure 4-4** XRD patterns of graphite (dark cyan), GO (dark yellow), and hydrothermal G/S composite (blue).

X-ray diffraction (XRD) patterns of graphite, graphene oxide, and hydrothermal G/S composite powders are shown in Figure 4-4. There is a broad and a narrow peak in the hydrothermal G/S composite with interlayer spacing of 0.37 nm. This value is much lower than that of GO (0.78 nm), but it is slight larger than that of graphite (0.34 nm). These results suggest that some  $\pi$ - $\pi$  stacking of graphene sheets and also residual oxygenated functional groups were still present in the graphene/SWNT composite structure.

XPS was applied to determine the elemental composition as well as chemical and electronic states of elements on the surface of the material (Figure 4-5). The surface chemistry of modified electrodes is known to affect the electrochemical processes, for example adsorption or chelation effects arise from surface charge [23]. Figure 4-5(a) shows the wide spectra for GO and hydrothermal G/S composite. Using the C1s and O1s signal intensities, the C:O ratios were calculated to be 2.3 and 10.4 for GO and hydrothermal G/S composite, respectively, which clearly revealed that the GO and a-SWNTs solution were effectively reduced in the hydrothermal process.

The high-resolution C1s spectra of GO and hydrothermal G/S composite are shown in Figure 4-5(b). The peak at 284.3 eV corresponds to the  $sp^2$  hybridized graphitic carbon and the peak at 290.7 eV corresponds to the  $\pi$ - $\pi^*$  structure. The peaks at 285.0, 287.0, and 288.4 eV are attributed to C-C, C-OH, and O-C=O, respectively.[24] Compared with GO, the spectra for the hydrothermal G/S composite had a dominant peak at 284.3 eV and two small peaks at 288.4 and 290.7 eV, corresponding to  $sp^2$  C-C, O-C=O, and  $\pi$ - $\pi^*$  bonds, respectively, which clearly revealed that most of the oxygen groups had been removed. The peak of O-C=O configuration at 288.4 eV indicates the chemical bonding between graphene and SWNTs by cross-linking reactions.

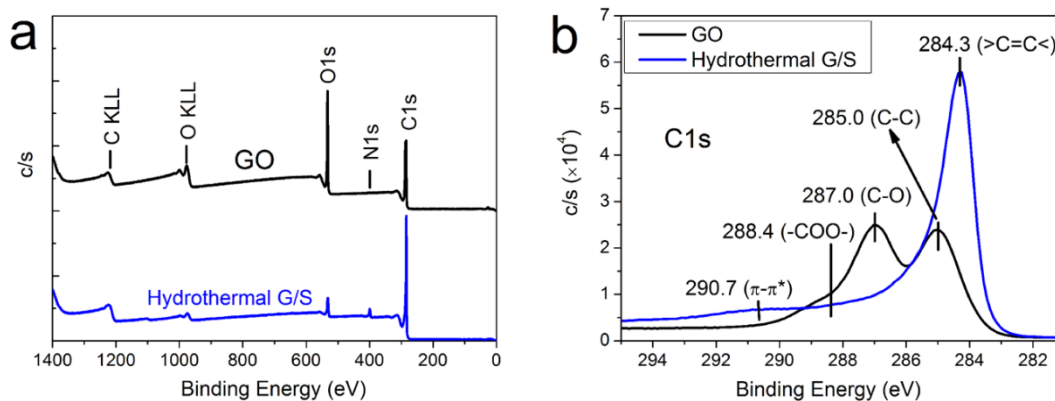


**Figure 4-5** The XPS wide spectra (a), and high resolution C1s XPS spectra (b) of GO (black line) and hydrothermal G/S composite (blue line).

To evaluate the electrochemical activity of the hydrothermal G/S composite for detection of UA, cyclic voltammograms (CV) were collected within the potential range from  $-0.2$  to  $0.8$  V at scanning rate of  $50$   $\text{mV s}^{-1}$ . The CVs of UA at H-G/S/GCE, H-G/GCE, a-S/GCE, and bare GCE are shown in Figure 4-6(a). As can be seen, UA exhibits a broad and small CV peak in response at  $0.47$  V at the bare GCE and a-S/GCE and H-G/GCE led to an increasing anodic peak at the same potential. Since catalyst impurities in SWNTs have been removed in the acid treatment, the reason for the improved performance of a-S/GCE is attributed to the nanoscale dimensions of the structural elements, the electronic structure, and the topological defects present on the nanotube surface and tips. The enhanced oxidation current due to UA on H-G/GCE is attributed to the high density of defective sites at graphene edges, which provided many more active sites for electron transfer to the biological species. [25] The height of oxidation peak of UA at H-G/S/GCE is the highest, which means that the concentration of UA at H-G/S/GCE was higher than that at a-S/GCE and H-G/GCE. It can be explained that the effective insertion of SWNT space in the graphene/SWNT composite reduced restacking of graphene sheets and also produced additional intra-pores, resulting larger surface area and more porosity in the structure. In addition, as a result, more active sites and reaction area were also exposed to the oxidation of UA.

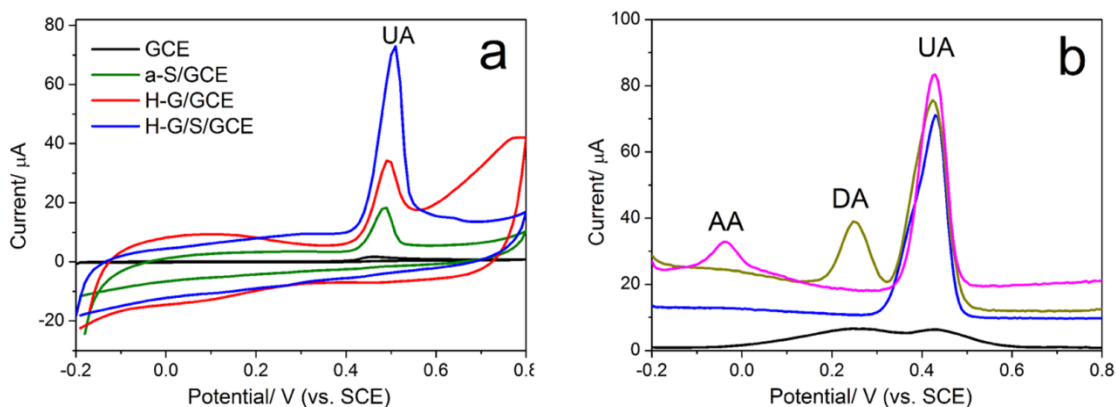


**Figure 4-6** (a) CVs of  $1.0 \times 10^{-5}$  M UA at bare GCE (black), a-S/GCE (olive), H-G/GCE (red), and

H-G/S/GCE (blue). (b) DPVs of a mixture of  $1.0 \times 10^{-5}$  M UA,  $4.0 \times 10^{-4}$  M AA, and  $2.5 \times 10^{-6}$  M DA at bare GCE (black);  $1.0 \times 10^{-5}$  M UA and  $4.0 \times 10^{-4}$  M AA (magenta),  $1.0 \times 10^{-5}$  M UA, and  $2.5 \times 10^{-6}$  M DA (dark cyan) and  $1.0 \times 10^{-5}$  M UA (blue) at H-G/S/GCE.

Figure 4-6(b) shows a series of differential pulse voltammograms (DPVs) of UA, ascorbic acid (AA), and dopamine (DA) mixture (DA and AA are typical interfering elements for electrochemical detection of UA, which coexist with UA in body fluid with similar oxidation potential on GCE). Only one rather broad, small, and overlay wave at 0.2-0.5 V appeared at the bare GCE (black curve). The current enhancement at H-G/S/GCE was remarkable and in addition, a decrease in the oxidation potential of AA occurred. AA, DA and UA can be distinguished from each other by a large anodic peak potential difference ( $\Delta E_{p(\text{UA,AA})} = 465$  mV (magenta curve) and  $\Delta E_{p(\text{UA,DA})} = 180$  mV (dark cyan curve)), which is large enough for selective determination of UA. In the buffer solution of pH 4.6, AA exists in an anionic form, while UA exists in a neutral form, since their  $pK_a$  values are 4.1 and 5.4, respectively. Neutral UA interacts more strongly with oxygen groups in graphene and SWNTs by hydrogen bonds. But  $\text{HA}^-$  (anionic form of AA) will be repelled by the negative charges remained in the composite.

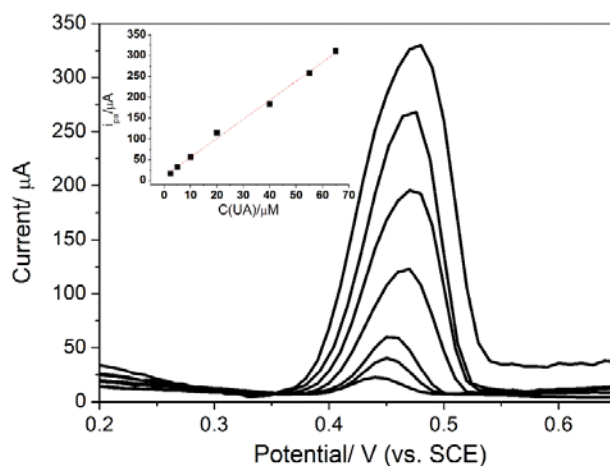


**Figure 4-7** DPV recordings of UA at H-G/S/GCE. Inset: graph of oxidation peak current vs. UA concentration.

The analytical determination experiments of UA were carried out using the DPVs for reducing the influence of background current. The oxidation peak current was related to the concentration of UA. A linear relationship between  $I_{pa}$  and the UA concentration was observed in the range of 2.5 and 65  $\mu\text{M}$  (Figure 4-7,  $y = 9.9663 + 4.5648x$ ,  $R = 0.9960$ ) and the detection limit was established to be 0.5  $\mu\text{M}$  ( $S/N = 3$ ). The H-G/S/GCE retained 98% of its initial response after 2 weeks of storage in dry conditions. Such stability is acceptable for most practical applications. The reproducibility was measured with the same electrode, and the relative standard deviation (RSD) was 0.8% ( $n=5$ ). When the modified electrode was prepared repeatedly five times, the RSD was 1.5%.

**Table 4-1** lists the determined parameters of this modified electrode in comparison with other modified electrodes that are often used for the determination of UA. Compared with the literature reports on the determination of UA [19, 26-29], the hydrothermal graphene/SWNT composite modified electrode showed excellent performance with a wider linear range, larger peak potential difference, and lower detection limit.

**Table 4-1** Figures of merits of comparable methods for determination of uric acid.

Electrode	Detection range (linear) ( $\mu\text{M}$ )	Detection limit ( $\mu\text{M}$ )	Peak potential difference (mV)	Ref.
MWCNT-T/GCE	10-200	1	$\Delta E_p(\text{UA, AA})=353$ $\Delta E_p(\text{UA, DA})=164$	[19]
$\alpha$ -CD/CNT/CPE	5.0-40.0	5.0	$\Delta E_p(\text{UA, DA})\approx 130$	[27]
PDDA-AuNPs-GNs/GCE	0.5-20	0.1	$\Delta E_p(\text{UA, AD})=170$	[28]
GC/HDA/ERGO electrode	5-1000	0.08	$\Delta E_p(\text{UA, XA})=370$ $\Delta E_p(\text{UA, HX})=710$	[29]
Poly(L-arginine)/Graphene	0.10-10.0	0.05	$\Delta E_p(\text{UA, XA})=390$ $\Delta E_p(\text{UA, HX})=760$	[30]
H-G/S/GCE	2.5-65	0.1	$\Delta E_p(\text{UA, AA})=465$ $\Delta E_p(\text{UA, DA})=180$	This work

## 4.4 Conclusion

We have developed a graphene/SWNT composite aerogel by an efficient and non-toxic hydrothermal synthesis. Structural characterization using SEM, TEM, BET, and XRD suggest that the composite structure having SWNTs effectively inserted between the graphene layers. The graphene/SWNT composite modified electrode has been successfully utilized in the selective detection of UA, eliminating the interference of AA and DA. The composite modified electrode shows excellent linearity from 2.5 to 65 $\mu\text{M}$ , lower detection limit of 0.1  $\mu\text{M}$ , and sustaining stability for two weeks.

## References

1. Agui L, Yanez-Sedeno P, Pingarron JM. Role of carbon nanotubes in electroanalytical chemistry - A review. *Anal Chim Acta* 2008,622:11-47.
2. Gong KP, Yan YM, Zhang MN, Su L, Xiong SX, Mao LQ. Electrochemistry and electroanalytical applications of carbon nanotubes: A review. *Analytical Sciences* 2005,21:1383-1393.
3. Rubianes MD, Rivas GA. Dispersion of multi-wall carbon nanotubes in polyethylenimine: A new alternative for preparing electrochemical sensors. *Electrochemistry Communications* 2007,9:480-484.
4. Pumera M. The Electrochemistry of Carbon Nanotubes: Fundamentals and Applications. *Chemistry-a European Journal* 2009,15:4970-4978.
5. Geim AK, Novoselov KS. The rise of graphene. *Nature Materials* 2007,6:183-191.
6. Novoselov KS, Jiang Z, Zhang Y, Morozov SV, Stormer HL, Zeitler U, et al. Room-temperature quantum hall effect in graphene. *Science* 2007,315:1379-1379.

7. Balandin AA, Ghosh S, Bao WZ, Calizo I, Teweldebrhan D, Miao F, et al. Superior thermal conductivity of single-layer graphene. *Nano Letters* 2008,8:902-907.
8. Bolotin KI, Sikes KJ, Jiang Z, Klima M, Fudenberg G, Hone J, et al. Ultrahigh electron mobility in suspended graphene. *Solid State Communications* 2008,146:351-355.
9. Huang X, Zeng ZY, Fan ZX, Liu JQ, Zhang H. Graphene-Based Electrodes. *Advanced Materials* 2012,24:5979-6004.
10. Shao YY, Wang J, Wu H, Liu J, Aksay IA, Lin YH. Graphene Based Electrochemical Sensors and Biosensors: A Review. *Electroanalysis* 2010,22:1027-1036.
11. Wang Y, Li Y, Tang L, Lu J, Li J. Application of graphene-modified electrode for selective detection of dopamine. *Electrochemistry Communications* 2009,11:889-892.
12. Chen D, Feng HB, Li JH. Graphene Oxide: Preparation, Functionalization, and Electrochemical Applications. *Chemical Reviews* 2012,112:6027-6053.
13. Yuan XY. Progress in Preparation of Graphene. *Journal of Inorganic Materials* 2011,26:561-570.
14. Alderman MH. Serum uric acid and cardiovascular disease risk. *Annals of Internal Medicine* 2000,132:591-591.
15. Lakshmi D, Whitcombe MJ, Davis F, Sharma PS, Prasad BB. Electrochemical Detection of Uric Acid in Mixed and Clinical Samples: A Review. *Electroanalysis* 2011,23:305-320.
16. Zanon NCM, Oliveira Jr ON, Caseli L. Immobilization of uricase enzyme in Langmuir and Langmuir-Blodgett films of fatty acids: Possible use as a uric acid sensor. *Journal of Colloid and Interface Science* 2012,373:69-74.
17. Georgakopoulos CD, Lamari FN, Karathanasopoulou IN, Gartaganis VS, Pharmakakis NM, Karamanos NK. Tear analysis of ascorbic acid, uric acid and malondialdehyde with capillary electrophoresis. *Biomedical Chromatography* 2010,24:852-857.
18. Dai XH, Fang X, Zhang CM, Xu RF, Xu B. Determination of serum uric acid using high-performance liquid chromatography (HPLC)/isotope dilution mass spectrometry (ID-MS) as a candidate reference method. *Journal of Chromatography B-Analytical Technologies in the Biomedical and Life Sciences* 2007,857:287-295.
19. Bi HQ, Li YH, Liu SF, Guo PZ, Wei ZB, Lv CX, et al. Carbon-nanotube-modified glassy carbon electrode for simultaneous determination of dopamine, ascorbic acid and uric acid: The effect of functional groups. *Sensors and Actuators B-Chemical* 2012,171:1132-1140.
20. Chattopadhyay D, Galeska I, Papadimitrakopoulos F. Complete elimination of metal catalysts from single wall carbon nanotubes. *Carbon* 2002,40:985-988.
21. Zhou Y, Bao QL, Tang LAL, Zhong YL, Loh KP. Hydrothermal Dehydration for the "Green" Reduction of Exfoliated Graphene Oxide to Graphene and Demonstration of Tunable Optical Limiting Properties. *Chemistry of Materials* 2009,21:2950-2956.
22. Schniepp HC, Li JL, McAllister MJ, Sai H, Herrera-Alonso M, Adamson DH, et al. Functionalized single graphene sheets derived from splitting graphite oxide. *Journal of Physical Chemistry B* 2006,110:8535-8539.
23. An Wong CH, Ambrosi A, Pumera M. Thermally reduced graphenes exhibiting a close relationship to amorphous carbon. *Nanoscale* 2012,4:4972-4977.
24. Li Y, Zhao Y, Cheng H, Hu Y, Shi G, Dai L, et al. Nitrogen-Doped Graphene Quantum Dots with Oxygen-Rich Functional Groups. *Journal of the American Chemical Society* 2011,134:15-18.

25. Banks CE, Davies TJ, Wildgoose GG, Compton RG. Electrocatalysis at graphite and carbon nanotube modified electrodes: edge-plane sites and tube ends are the reactive sites. *Chemical Communications* 2005:829-841.
26. Ghoreishi SM, Behpour M, Fard MHM. Electrochemical methods for simultaneous determination of trace amounts of dopamine and uric acid using a carbon paste electrode incorporated with multi-wall carbon nanotubes and modified with alpha-cyclodextrine. *Journal of Solid State Electrochemistry* 2012,16:179-189.
27. Xue Y, Zhao H, Wu ZJ, Li XJ, He YJ, Yuan ZB. The comparison of different gold nanoparticles/graphene nanosheets hybrid nanocomposites in electrochemical performance and the construction of a sensitive uric acid electrochemical sensor with novel hybrid nanocomposites. *Biosens Bioelectron* 2011,29:102-108.
28. Raj MA, John SA. Simultaneous determination of uric acid, xanthine, hypoxanthine and caffeine in human blood serum and urine samples using electrochemically reduced graphene oxide modified electrode. *Anal Chim Acta* 2013,771:14-20.
29. Zhang FY, Wang ZH, Zhang YZ, Zheng ZX, Wang CM, Du YL, et al. Simultaneous electrochemical determination of uric acid, xanthine and hypoxanthine based on poly(L-arginine)/graphene composite film modified electrode. *Talanta* 2012,93:320-325.

---

## Chapter 5

# Elimination of Ascorbic Acid and Sensitive Detection of Uric Acid at the MnO<sub>2</sub> Nanorods /Graphene-based Modified Electrode

---

### 5.1 Introduction

Graphene, a two-dimensional (2D) monolayer of carbon atoms in a tightly packed honeycomb  $sp^2$  carbon lattice, has attracted significant research interest in recent years. Its intriguing physiochemical properties, such as unusual electric properties, large thermal conductivity, superior mechanical properties and chemical stability, large surface area, biocompatibility and electrochemical properties provide potential applications in fabricating various electronic devices and biosensors.[1, 2] Nowadays, graphene could be prepared by the facile route of the chemical reduction of graphene oxide with low cost, easy operation and mass production. More importantly, with their two-dimensional nanostructures and adjustable surface chemistry, graphene sheets can interact strongly with other organic and/or inorganic systems with combination and synergistic effects of different components.[3-5] Therefore, the special properties of graphene may provide insight for fabricating novel electrochemical sensors for virtual applications. Recently, graphene based modified electrodes have been reported extensively.[6, 7] Compared with single walled carbon nanotubes, graphene illustrated a better sensitivity, signal-to-noise ratio, and stability. For example, Alwarappan et al. [8] employed chemically synthesized graphene nanosheets as electrode materials for the electrochemical detection of important neurotransmitters such as dopamine and serotonin. Srivastava et al. [9] utilized functionalized multilayered graphene to immobilize urease and glutamate dehydrogenase for fabrication of a novel amperometric urea electrochemical biosensor with a lower detection limit of 3.9 mg/dL and a short response time of 10s. These enhanced sensing properties are mainly attributed to the presence of more  $sp^2$  like planes and various edge defects present on the surface of graphene. Furthermore, several graphene composites, such as graphene/polymer composite, graphene/metal oxide composite and graphene/ionic liquid composite, based electrochemical sensors have also been developed for bioanalysis. For example, Shan et al.[10] constructed a novel polyvinylpyrrolidone-protected graphene/polyethylenimine-functionalized ionic liquid/glucose oxidase (GOD) composite electrochemical biosensor, achieving direct electron transfer of GOD. Palanisamy et al.[11] developed a nonenzymatic amperometric sensor for hydrogen peroxide using graphene oxide/zinc oxide composite by a simple and cost effective approach. Peng et al. [12] fabricated a graphene and room temperature ionic liquid (IL, BMIMPF<sub>6</sub>) composite modified electrode towards the oxidation of azithromycin, obtaining a remarkably enhanced electrocatalytic activity. Sun et al.[13] constructed a graphene-SnO<sub>2</sub> nanocomposite modified electrode for the sensitive electrochemical detection of dopamine. In our previous work, we developed a quercetin -graphene composite-modified glassy carbon electrode (Qu/GH/GCE) for the selective and sensitive detection of

dopamine (DA). [14]

Uric acid (UA) is a kind of small electroactive biomolecule, created when the body breaks down substances called purine nucleotides. High concentration of UA in blood leads to a type of arthritis, such as gout, and serum uric related to type II diabetes. The currently detection methods of UA include enzymatic-based assay,[15] capillary electrophoresis,[16] high performance liquid chromatography [17] and electrochemical technique[18]. Among those methods, the electrochemical method is the most rapid, simple and convenient one. But one of the major problems in biological determination of uric acid comes from electrochemical interferences such as ascorbic acid (AA), which has a similar oxidation potential at normal electrodes. In order to solve this problem, various methods have been developed [19]. Recently, some attentions were paid to fabricating of carbon-based sensors for the detection of UA. For example, Esmael Alipour et al.[20] fabricated a pretreated pencil graphite electrode for the simultaneous determination of dopamine and uric acid in biological samples. Bingyan Zhang et al.[21] reported the simultaneous electrochemical determination of ascorbic acid, dopamine and uric acid with helical carbon nanotubes. Sun et al.[22] created a graphene/Pt-modified glassy carbon electrode to simultaneously characterize ascorbic acid (AA), dopamine (DA), and uric acid (UA) levels. During the preparation of the nanocomposite, size-selected Pt nanoparticles with a mean diameter of 1.7 nm were self-assembled onto the graphene surface. In our previous work,[23] we fabricated the poly acridine orange/graphene modified electrode (PAO/GH/G CE) by immobilizing graphene (GH) onto the surface of glassy carbon electrode (GCE) then electro-polymerizing acridine orange (AO) on the GH/GCE matrix with an electrolysis micelle disruption method for selective determination of uric acid.

Manganese oxide is a kind of attractive inorganic material in biosensing application, due to their excellent catalytic oxidation abilities.[24-26] Recently, many efforts have been focused on the synthesis of nanoscale  $\text{MnO}_2$ /carbon nanotubes (graphene or graphene oxide or porous carbon) hybrids due to their significant electrochemical applications, such as supercapacitors. Our group [27] has successfully fabricated binderless supercapacitors using graphene and  $\text{MnO}_2$ -nanoflowers coated graphene to provide a high specific capacitance of 245 F/g for graphene and 328 F/g for  $\text{MnO}_2$ -coated graphene. Herein, we fabricated a novel biosensor ( $\text{MnO}_2$  NR/RGO) based on  $\text{MnO}_2$  nanorods ( $\text{MnO}_2$  NR) and reduced graphene oxide (RGO) composites for the electrochemical detection of UA. The ultra large surface area of graphene provides more reactive sites for electroactive molecules, and good conductivity can facilitate electron transfer, which improves the sensitivity for UA dramatically. Interestingly,  $\text{MnO}_2$  nanorods can be as an eliminator of ascorbic acid. The  $\text{MnO}_2$  NR/RGO composites may take advantage of the synergetic effect from different nanomaterials and provide enhanced performance. Moreover, as  $\text{MnO}_2$  nanorods coated on the plane of graphene nanosheets, it can be acted as a separator for avoiding the restacking effect of graphene. At the same time, some intrapores would generate to increase the specific surface area, and the biomolecules be more accessible to the electrode surface.

## 5.2 Experimental

### 5.2.1 Reagents and Apparatus

Manganese sulfate (MnSO<sub>4</sub>), KMnO<sub>4</sub>, uric acid, L(+)-ascorbic acid and potassium hexacyanoferrate (III) (K<sub>3</sub>[Fe(CN)<sub>6</sub>], ≥ 99.0%) were obtained from Nacalai tesque, Japan. Potassium hexacyanoferrate(II) trihydrate (K<sub>4</sub>[Fe(CN)<sub>6</sub>], 98.5-102.0%) was purchased from Sigma-Aldrich. All solutions were prepared with doubly distilled water. Graphite (99%) was provided by Nacalai tesque, Japan.

Electrochemical experiments were performed via a CompactStat (Ivium Technologies, Netherlands) with a conventional three-electrode system. A bare electrode (glassy carbon electrode, GCE) and the modified electrodes were applied as working electrodes. A platinum wire and a saturated calomel electrode (SCE) were used as the counter and reference electrodes, respectively.

Characterizations of morphologies and crystalline structure were performed by scanning electron microscopy (SEM, JSM-7001F), transmission electron microscopy (TEM, JEM-2100), atomic force microscopy (AFM, Agilent's PicoScan) and X-ray powder diffraction (XRD, RINT 2500HF, RIGAKU).

### 5.2.2 Synthesis of Reduced Graphene Oxide (RGO)

Graphene oxide was synthesized by using the modified Hummers method. A mixture of graphite (3.0 g) and NaNO<sub>3</sub> (1.5 g) were added into 23 mL of 98% H<sub>2</sub>SO<sub>4</sub>, followed by stirring in an ice bath. After that, potassium permanganate (KMnO<sub>4</sub>, 8.0 g) was then added to the suspension little by little. The mixture was stirred at room temperature for 2 h and then 90 mL of distilled water was added, which would be heated quickly to about 90°C. After being stirred for 12 h, 30 mL of 30 % H<sub>2</sub>O<sub>2</sub> was added to the mixture. The mixture was washed by 5 % HCl and distilled water for several times for purification. After filtration and drying in vacuum, graphene oxide was obtained.

In a typical procedure for reduction of graphene oxide, graphene oxide (100 mg) was firstly dispersed in 30 mL distilled water and sonicated for 30 min. The brown graphene oxide (30 mL) suspension was mixed with 3 mL hydrazine monohydrate. The mixture was then put in a water bath (98°C) for 24 h. The stable black dispersion in the vial was washed with distilled water for several times to remove the excessive hydrazine and then centrifuged at 4000 rpm for 3 min to remove bulk graphite. The final product, RGO, was obtained by vacuum filtration and dried in vacuum.

### 5.2.3 Fabrication of Modified Electrode

A GCE was firstly polished by chamois leather containing Al<sub>2</sub>O<sub>3</sub> slurry (first 0.3 μm then 0.05 μm), then ultrasonically cleaned in distilled water, finally dried at room temperature. 6 μL of RGO solution (1 mg mL<sup>-1</sup>) was dropped on the surface of GCE and dried in air to form the RGO modified electrode (RGO/GCE).

MnO<sub>2</sub> NR/RGO modified electrode (MnO<sub>2</sub> NR/RGO/GCE) was prepared by a simple casting method. Firstly, the MnO<sub>2</sub> nanorods (MnO<sub>2</sub> NR) were synthesized by hydrothermal method as the following processes: 0.2 g of manganese sulfate (MnSO<sub>4</sub>) and 0.5 g of KMnO<sub>4</sub> were dissolved in deionized water (200 mL) under stirring. After that, the mixture was refluxed at 98 °C for 6 h. Secondly, a mixture of MnO<sub>2</sub> NR

and RGO at a concentration ratio of 1:1 (2 mg mL<sup>-1</sup> RGO and 2 mg mL<sup>-1</sup> MnO<sub>2</sub> NR) was dispersed in water and ultrasonicated to obtain well-proportioned composite solution. Finally, 6 μL of the composite solution (1mg mL<sup>-1</sup>) was dropped onto a GCE and then dried at room temperature.

### 5.2.4 Electrochemical Measurement

Electrochemical experiments were carried out in the three-electrode system by cyclic voltammetry (CV) and differential pulse voltammetry (DPV) methods. The potential interval was from -0.2 to 0.8 V. Electrochemical impedance spectroscopy (EIS) was done using a sinusoidal signal with mean voltage of 0 V and amplitude of 10 mV over a frequency range of 100 kHz to 10 mHz.

## 5.3 Results and Discussion

### 5.3.1 Characterization of RGO, MnO<sub>2</sub> NR and MnO<sub>2</sub> NR/RGO Composite

A TEM image of the as-synthesized RGO is shown in [Figure 5-1b](#). In this case, it clearly explains the flake-like shape. The morphology and nano-scale structure of graphene was further examined using atomic force microscope (AFM) ([Figure 5-1a](#)). From the Fig. 1a, it can be seen that the thickness of the RGO is about 2~3 nm, belonging to few-layer graphene given by the classification of the graphene-based nanomaterials[28].

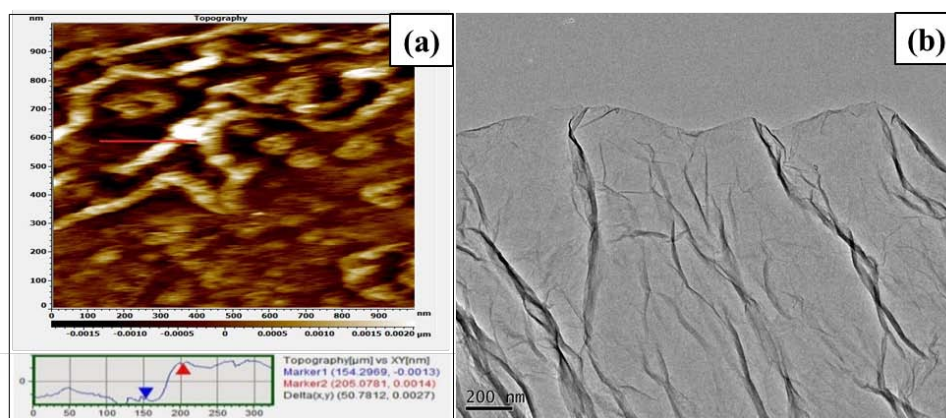


**Figure 5-1** AFM (a) and TEM (b) images of as-prepared RGO.

The morphology of the MnO<sub>2</sub> and MnO<sub>2</sub> NR/RGO composite were presented in [Figure 5-2](#). [Figure 5-2\(a\)](#) is X-ray diffraction pattern of MnO<sub>2</sub>. All the diffraction peaks can be easily indexed to planes of α-MnO<sub>2</sub> crystal, which are in agreement with the standard datafile (JCPDS file NO. 42 -1169). [Figure 5-2 \(b\)](#) shows the TEM image of MnO<sub>2</sub>. As shown, the as-synthesized MnO<sub>2</sub> looks like nanorods. The interplanar distance of MnO<sub>2</sub> (211,310) are 0.24 nm and 0.30 nm, respectively ([Figure 5-2 \(b\), inset](#)). The morphology of the as-synthesized MnO<sub>2</sub>/graphene composite was illustrated in [Figure 5-2 \(c, d\)](#). As revealed by the SEM and TEM images, the MnO<sub>2</sub> nanorods are randomly distributed on the surface of the RGO, which indicating the successfully formation of nanocomposites with graphene nanosheets and MnO<sub>2</sub> nanorods.

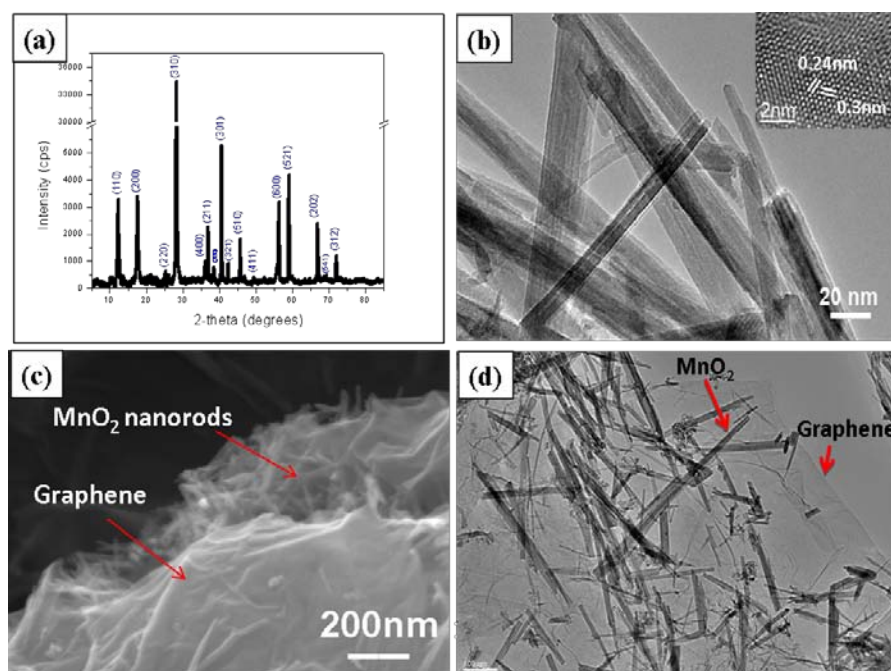


**Figure 5-2** Morphology and structural characterization of as prepared MnO<sub>2</sub> and MnO<sub>2</sub>/graphene composite. (a) XRD of MnO<sub>2</sub> nanorods, (b) TEM image of MnO<sub>2</sub> nanorods, the inset is a portion of the image at higher magnification, (c, d) SEM and TEM images of MnO<sub>2</sub>/graphene composite.

### 5.3.2 Electrochemical Behaviors of the MnO<sub>2</sub> NR/RGO Modified Electrodes

Electrochemical impedance spectrum (EIS) was applied for studying the performance of the electrode interface. **Figure 5-3** shows the electrochemical impedance spectra on the bare GCE (a), MnO<sub>2</sub> NR/GCE (b), MnO<sub>2</sub> NR/RGO/GCE (c) and RGO /GCE (d) in 0.1M KCl containing equimolar [Fe(CN)<sub>6</sub>]<sup>3-/4-</sup>. As shown, the electron transfer resistance of the electrode decreased after modification, and compared to RGO/GCE, the modification of graphene with MnO<sub>2</sub> inhibits fast electron transfer to some extent due to the presence of semiconductive MnO<sub>2</sub>. Nevertheless, the Nyquist complex plane plot of MnO<sub>2</sub> NR/RGO/GCE is almost straight line, which shows that the MnO<sub>2</sub> NR/RGO/GCE still keeps fast electron transfer.

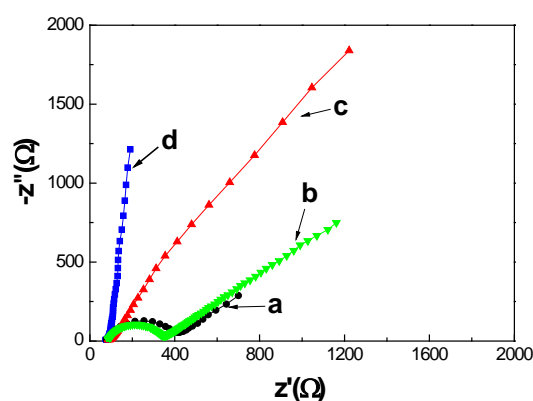


**Figure 5-3** Electrochemical impedance spectra of the bare GCE (a), MnO<sub>2</sub> NR/GCE (b), MnO<sub>2</sub> NR /RGO/GCE (c) and GR/GCE (d) in 0.1 M KCl containing equimolar [Fe(CN)<sub>6</sub>]<sup>3-/4-</sup>

The DPV responses of the mixture solution containing 0.5mM UA and 0.5mM AA at the different modified electrodes are shown in Figure 5-4 (A). As shown, UA and AA exhibited an overlapped and broad anodic peak at bare GCE (a) with a peak potential at 375 mV. Two oxidation peaks of UA and AA at the RGO/GCE (c) were observed at 300 mV and -10 mV, respectively. However, only the oxidation peak of UA at MnO<sub>2</sub> NR/GCE (b) and MnO<sub>2</sub> NR/RGO/GCE (d) was obtained at 310 mV and 335 mV respectively, which indicates that MnO<sub>2</sub> NR can eliminate the oxidation of AA. It also shows that the oxidation current of UA at MnO<sub>2</sub> NR/RGO/GCE is dramatically increase by 14 times compared to the MnO<sub>2</sub> NR/GCE. This because RGO could provide more reactive sites for UA molecules, and help to realize fast electron transfer between electrode and UA.

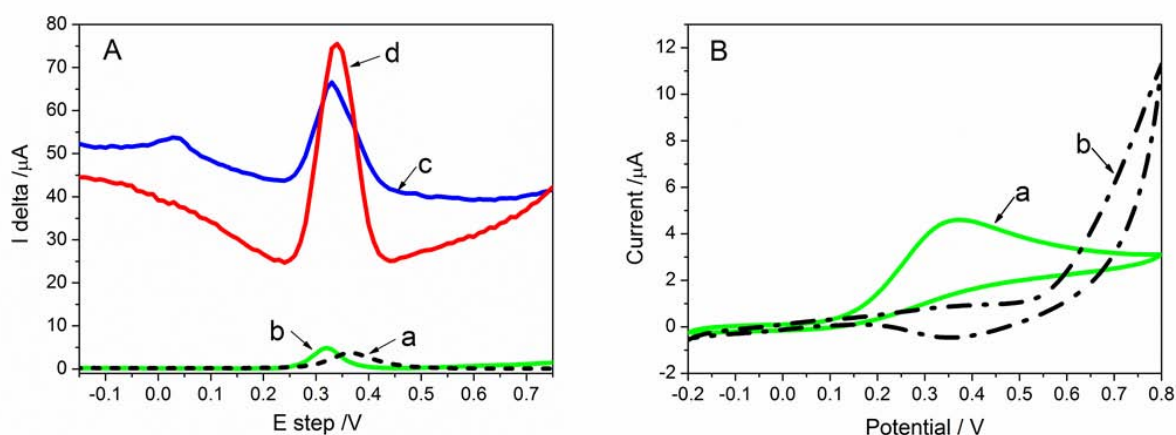
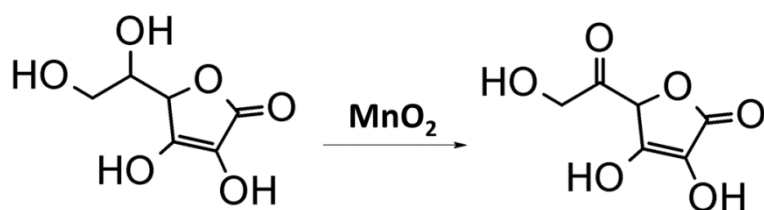


**Figure 5-4** (A) DPVs of the bare GCE (a), MnO<sub>2</sub> NR/GCE (b), RGO/GCE (c), MnO<sub>2</sub> NR/RGO/GCE (d) in PBS (pH 6.5) containing a mixture of 0.5 mM UA and 0.5 mM AA. Scan rate: 100 mV/s. (B) Current responses at bare GCE (a) and MnO<sub>2</sub> NR /GCE (b) in 0.1M pH 6.5 PBS in the presence of  $1 \times 10^{-3}$  M AA

In order to verify the mechanism of eliminating effect of AA at MnO<sub>2</sub> NR/GCE, the CV responses of  $1 \times 10^{-3}$  M AA on the bare GCE and the MnO<sub>2</sub> NR/GCE in 0.1M pH 6.5 PBS were studied. Figure 5-4 (B) shows there is a big respond of AA at the bare GCE with the peak current of  $6 \times 10^{-7}$  A (curve a), whereas there is no current respond of AA at the MnO<sub>2</sub> NR/GCE (curve b), indicating MnO<sub>2</sub> NR can eliminate the effect of AA. This may arise from a special reaction that MnO<sub>2</sub> can catalyze hydroxyl to carbonyl, and this carbonyl form has no-electrochemical activity. The special reaction is illustrated as below. MnO<sub>2</sub> nanoparticles has been reported that can electively oxidize AA to electrochemical inactive product, and thus eliminate the interference of AA on a glucose biosensor [29].



Moreover, we studied the effect of the scan rates from 10 to 300mV/s on the electrochemical behavior

of UA at the MnO<sub>2</sub> NR/RGO/GCE. A relationship between the peak current and the scan rate is linear with the scan rate increased from 20 to 250mV/s. The equation is  $I_p(\mu\text{A}) = 33.26 + 0.79 v \text{ (mV/s)}$ ,  $R = 0.9923$ , indicating that the electrochemical oxidation of UA at the MnO<sub>2</sub> NR/RGO/GCE was controlled by adsorption process.

### 5.3.3 UA Electrochemical Detection Performance on the MnO<sub>2</sub> NR/RGO/GCE

Under the optimal conditions, the MnO<sub>2</sub> NR/RGO/GCE was applied for UA detection. The dependence of the peak current response on UA concentration is shown in Figure 5-5. The anodic peak current response showed a liner increase as the UA concentration increased from  $5 \times 10^{-8}$  to  $4 \times 10^{-4}$  M. The regression equation is  $I_p(\mu\text{A}) = 6.89 + 0.17 C (\mu\text{M})$  ( $R= 0.9992$ ) and the detection limit is up to  $1.0 \times 10^{-8}$  M ( $S/N = 3$ ). In addition, the modified electrode showed good stability and reproducibility. A relative standard deviation (RSD) is 1.8 % for 20 times parallel detections. In order to understand the stability of the modified electrode, it was stored at room temperature for four weeks. 95.5% of the initial response current was remained after four weeks. Therefore, the MnO<sub>2</sub> NR/RGO/GCE displays the promise for the determination of UA with high sensitivity, low detection limit and good reproducibility.

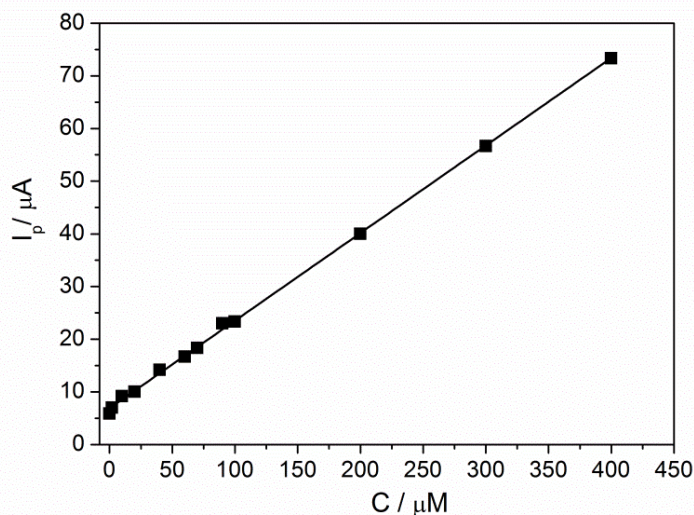


**Figure 5-5** The linear relationship between the peak current and UA concentration

### 5.3.4 Analysis of Human Urine Samples

The MnO<sub>2</sub> NR/RGO/GCE was applied to the direct analysis of UA in human urine samples. The urine samples were acquired from our three laboratory person and then diluted by using 0.1 M PBS for determination (1000 times dilution of the 24-hour collected urine sample). The results obtained from five parallel measurements were presented at Table 5-1. The data of recovery and RSD confirmed that proposed method can be used effectively for the quantitative analysis of UA.

**Table 5-1** Analysis of UA in human urine ( $n = 5$ )

Sample	UA detected ( $\mu\text{M}$ )	UA added ( $\mu\text{M}$ )	Found ( $\mu\text{M}$ )	Recovery (%)	RSD (%)
Urine 1	1.98	10	12.01	100.2	1.2
Urine 2	2.00	20	21.68	98.5	1.6
Urine 3	2.03	30	32.25	100.6	1.3

## 5.4 Conclusions

A novel sensor of  $\text{MnO}_2$  NR/RGO/GCE was fabricated by using synthesized  $\text{MnO}_2$  NR/RGO film and then used to investigate the electrochemical behavior of UA in the presence of AA. The  $\text{MnO}_2$  nanorods could eliminate the effect of AA effectively. Moreover, ultra large surface area and good conductivity of RGO can provide more reactive sites for UA molecules and help to realize fast electron transfer. The high selectivity and sensitivity towards UA were acquired at  $\text{MnO}_2$  NR/RGO/GCE. The developed sensor has been applied to the selective determination of UA in human urine with satisfactory results.

## References

1. Wang Y, Lu J, Tang L, Chang H, Li J. Graphene Oxide Amplified Electrogenerated Chemiluminescence of Quantum Dots and Its Selective Sensing for Glutathione from Thiol-Containing Compounds. *Anal Chem* 2009,81:9710-9715.
2. Chen D, Feng H, Li J. Graphene Oxide: Preparation, Functionalization, and Electrochemical Applications. *Chemical Reviews* 2012,112:6027-6053.
3. Chua CK, Pumera M. Covalent chemistry on graphene. *Chem Soc Rev* 2013,42:3222-3233.
4. Li N, Cao MH, Hu CW. Review on the latest design of graphene-based inorganic materials. *Nanoscale* 2012,4:6205-6218.
5. Strikha MV. Non-volatile memory and IR radiation modulators based upon graphene-on-ferroelectric substrate. A review. *Ukrainian Journal of Physical Optics* 2012,13:S5-S26.
6. Wang ZH, Gao YL, Xia JF, Zhang FF, Xia YZ, Li YH. Synthesis and characterization of glycyrrhizin-decorated graphene oxide for hepatocyte-targeted delivery. *Comptes Rendus Chimie* 2012,15:708-713.
7. Shao YY, Wang J, Wu H, Liu J, Aksay IA, Lin YH. Graphene Based Electrochemical Sensors and Biosensors: A Review. *Electroanalysis* 2010,22:1027-1036.
8. Alwarappan S, Erdem A, Liu C, Li C-Z. Probing the Electrochemical Properties of Graphene Nanosheets for

- Biosensing Applications. *The Journal of Physical Chemistry C* 2009,113:8853-8857.
9. Srivastava RK, Srivastava S, Narayanan TN, Mahlotra BD, Vajtai R, Ajayan PM, et al. Functionalized Multilayered Graphene Platform for Urea Sensor. *Acs Nano* 2012,6:168-175.
  10. Shan CS, Yang HF, Song JF, Han DX, Ivaska A, Niu L. Direct Electrochemistry of Glucose Oxidase and Biosensing for Glucose Based on Graphene. *Anal Chem* 2009,81:2378-2382.
  11. Palanisamy S, Chen SM, Sarawathi R. A novel nonenzymatic hydrogen peroxide sensor based on reduced graphene oxide/ZnO composite modified electrode. *Sensors and Actuators B-Chemical* 2012,166:372-377.
  12. Peng JY, Hou CT, Liu XX, Li HB, Hu XY. Electrochemical behavior of azithromycin at graphene and ionic liquid composite film modified electrode. *Talanta* 2011,86:227-232.
  13. Sun W, Wang X, Wang Y, Ju X, Xu L, Li G, et al. Application of graphene-SnO<sub>2</sub> nanocomposite modified electrode for the sensitive electrochemical detection of dopamine. *Electrochimica Acta*,87:317-322.
  14. Wang Z, Xia J, Zhu L, Chen X, Zhang F, Yao S, et al. A Selective Voltammetric Method for Detecting Dopamine at Quercetin Modified Electrode Incorporating Graphene. *Electroanalysis*,23:2463-2471.
  15. Zanon NCM, Oliveira ON, Caseli L. Immobilization of uricase enzyme in Langmuir and Langmuir-Blodgett films of fatty acids: Possible use as a uric acid sensor. *Journal of Colloid and Interface Science* 2012,373:69-74.
  16. Georgakopoulos CD, Lamari FN, Karathanasopoulou IN, Gartaganis VS, Pharmakakis NM, Karamanos NK. Tear analysis of ascorbic acid, uric acid and malondialdehyde with capillary electrophoresis. *Biomedical Chromatography* 2010,24:852-857.
  17. Zuo YG, Wang CJ, Zhou JP, Sachdeva A, Ruelos VC. Simultaneous Determination of Creatinine and Uric Acid in Human Urine by High-Performance Liquid Chromatography. *Analytical Sciences* 2008,24:1589-1592.
  18. Akyilmaz E, Sezginurk MK, Dinckaya E. A biosensor based on urate oxidase-peroxidase coupled enzyme system for uric acid determination in urine. *Talanta* 2003,61:73-79.
  19. Wang Z, Wang Y, Luo G. A selective voltammetric method for uric acid detection at [small beta]-cyclodextrin modified electrode incorporating carbon nanotubes. *Analyst* 2002,127:1353-1358.
  20. Alipour E, Majidi MR, Saadatirad A, Golabi Sm, Alizadeh AM. Simultaneous determination of dopamine and uric acid in biological samples on the pretreated pencil graphite electrode. *Electrochimica Acta*,91:36-42.
  21. Zhang B, Huang D, Xu X, Alemu G, Zhang Y, Zhan F, et al. Simultaneous electrochemical determination of ascorbic acid, dopamine and uric acid with helical carbon nanotubes. *Electrochimica Acta*,91:261-266.
  22. Sun C-L, Lee H-H, Yang J-M, Wu C-C. The simultaneous electrochemical detection of ascorbic acid, dopamine, and uric acid using graphene/size-selected Pt nanocomposites. *Biosensors and Bioelectronics*,26:3450-3455.
  23. Wang Z, Xia J, Zhu L, Zhang F, Guo X, Li Y, et al. The fabrication of poly (acridine orange)/graphene modified electrode with electrolysis micelle disruption method for selective determination of uric acid. *Sensors and Actuators B: Chemical*,161:131-136.
  24. Wang L, Wang D-L. Preparation and electrochemical characterization of MnOOH nanowire 鈥搒raphene oxide. *Electrochimica Acta*,56:5010-5015.
  25. Wang B, Park J, Wang C, Ahn H, Wang G. Mn<sub>3</sub>O<sub>4</sub> nanoparticles embedded into graphene nanosheets: Preparation,

- characterization, and electrochemical properties for supercapacitors. *Electrochimica Acta*,55:6812-6817.
26. Wu M-S, Lin C-J, Ho C-L. Multilayered architecture of graphene nanosheets and MnO<sub>2</sub> nanowires as an electrode material for high-performance supercapacitors. *Electrochimica Acta*,81:44-48.
  27. Cheng Q, Tang J, Ma J, Zhang H, Shinya N, Qin L-C. Graphene and nanostructured MnO<sub>2</sub> composite electrodes for supercapacitors. *Carbon*,49:2917-2925.
  28. Rao CNR, Sood AK, Subrahmanyam KS, Govindaraj A. Graphene: The New Two-Dimensional Nanomaterial. *Angewandte Chemie International Edition* 2009,48:7752-7777.
  29. Xu J-J, Luo X-L, Du Y, Chen H-Y. Application of MnO<sub>2</sub> nanoparticles as an eliminator of ascorbate interference to amperometric glucose biosensors. *Electrochemistry Communications* 2004,6:1169-1173.

---

## Chapter 6

# Electrochemistry of HOPG Electrodes: Edge and Basal Plane Effect for Supercapacitor and Biosensing

---

### 6.1 Introduction

The molecular engineering of an electrode surface is of paramount importance for the development of electrochemical devices with region-specific electron-transfer capabilities. As it has a unique two-dimensional molecular geometry and excellent electronic properties, graphene has been widely used as functional electrodes in various electrochemical systems, such as chemical sensors, biosensors, supercapacitors, and batteries [1-3].

Supercapacitors store the charge at the electrode/electrolyte interface through reversible ion adsorption at high-surface-area porous carbon electrodes (activated carbon, carbon nanotubes and graphene) [4-9]. But the molecular mechanism is still not quite clear: the large capacitances achieved seem to demand a much higher level of charge separation at the interface under the influence of an applied potential than can be readily explained by studies of idealized electrode geometries. To build higher-performance materials, one should know whether the increase in capacitance is due only to a larger surface area or if the pore structure or surface chemistry also plays a role. Figuring out these questions through experiments alone is difficult because of lacking of the techniques to probe the relationship between the local degree of charge separation and the local structure of pores. A computational approach was presented for explaining the enhanced capacitance in microporous carbon electrodes [10]. The capacitance in quantitative is agreement with experimental results in ionic liquid electrolyte, shown that the increase of capacitance is not merely due to a larger surface area and demonstrate the key role of the pore size and microstructure.

An chemically activated microwave-expanded graphite oxide (a-MEGO) was synthesized by activating a graphene-like precursor with potassium hydroxide[11]. This porous material proved to be composed of atom-thick walls of trivalently bonded carbon and pores of 0.6-5.0 nanometres in diameter. It has a remarkably high surface area- 3,100 m<sup>2</sup>/g, which is about 17% higher than theoretical value of graphene itself. And the carbon lattice in this structure includes heptagons and octagons that form regions of so-called negative curvature -or the familiar saddle shape, and the content of oxygen and hydrogen is low. The authors expected to attribute an ultrahigh specific capacitance of above 150F/g to the separate perforated thin sheets with many atoms along the sheet edges. It has been reported that when crumpled, the carbon atoms along a fold are more reactive[12]. In the case of graphene, one may wonder how its physical deformation (ripples,

edges and introduced groups) affects its chemical activity.

Graphene derivatives, including pristine graphene, GO, chemically reduced GO (rGO)[13] and N-doped graphene[14] have been intensively studied for their widespread applications in biosensing and detection of biomolecules such as hemin, DNA, urea and dopamine[15-19]. Many studies have suggested that much of the enhanced electrochemical activity and electron-transfer rate at graphene electrodes arises from the surface defects and functional groups load on the basal plane and edge. [20] It has been reported that the heterogeneous electron transfer from/to a graphene sheet takes place on the edges of the graphene sheet, while heterogeneous electron transfer from the plane of a graphene sheet is very close to zero.[21] However, no convincing experimental evidence has been obtained owing to technical difficulties in distinguishing the electrochemical role of the graphene surface atom from its edge.

This situation was further complicated by oxygen-containing groups, often introduced through chemical/electrochemical oxidation of the graphene, which could affect the absorption and reactive kinetics. For example, there is a controversy over whether this influence is positive (i.e., enhances the heterogeneous electron transfer rate) or negative (slows the heterogeneous electron transfer rate). Chou et al. suggested that the carboxylic groups at electrodes modified by single-walled carbon nanotubes are responsible for increasing the heterogeneous electron transfer rate constant (and thus for increasing the speed of electron transfer) of ferro/ferricyanide.[22] However, Ji et al. showed that with an increasing amount of oxygen-containing groups present on graphite microparticles, heterogeneous electron transfer between the graphitic material and ferro /ferricyanide decreases.[23] The effect of oxygen-containing groups on the electrochemistry of graphene is not just their influence on the heterogeneous electron transfer rate but also on the adsorption/desorption of molecules, which takes place before and after the electrochemical reaction.[20]

In this work, in order to study the electrochemistry of the graphene basal plane and edge specifically, we selectively masking regions of the highly oriented pyrolytic graphite (HOPG) with a nonconducting polymer coating (e.g. polystyrene, PS) such that the electrolyte has access the basal plane and edge only. The effectiveness of the polymer masking was checked by fully coating the HOPG with polystyrene under the same conditions: no electrochemical signal was observed at all. Sulfuric acid solution was used as an electrolyte for study of edge and basal plane effect of graphene for supercapacitor. And various electrochemical probes, including  $K_3[Fe(CN)_6]$ , uric acid (UA) and ascorbic acid (AA) with specific electrochemical sensitivities to various surface states of an electrode,[23, 24] were then used to monitor the electrochemical activities of the basal plane and edge atoms.

## 6.2 Experimental

### 6.2.1 Fabrication of HOPG Edge (HOPG-E) and Basal Plane Electrodes (HOPG-P)

Figure 1 shows a schematic representation of the procedure for the HOPG-E and HOPG-P electrodes from the HOPG sheet (thickness of 100 $\mu$ m). To start with, HOPG sheet were connected to a copper belt (step

1 in Figure 1) with silver epoxy. The HOPG electrode with only the edge exposed (designated as the HOPG-E electrode) was then prepared by thoroughly coating the copper-belt-supported HOPG with a PS solution (15wt% in toluene) and drying at 50°C in air (step 2 in Figure 1), followed by partially cutting off the free end of the polymer-wrapped HOPG (step 3 in Figure 1). The access of aqueous electrolytes to the inner wall of the HOPG side wall layers can be effectively limited by its hydrophobic nature. [9] On the other hand, the HOPG electrode with only the basal plane exposed (designated as the HOPG-P electrode) was prepared by coating the all sides and back of the copper-belt-supported HOPG with the PS solution and drying at 50°C in air (step 4 in Figure 1).

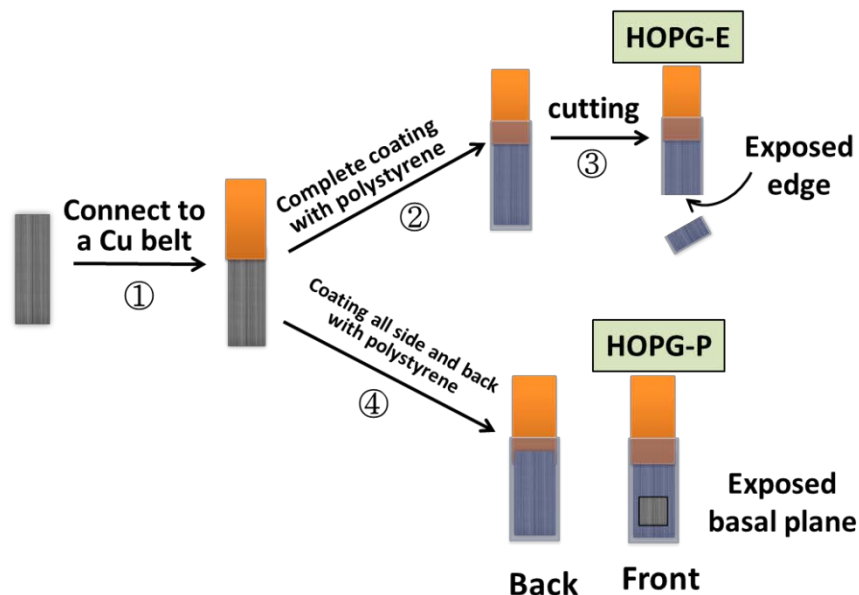


**Figure 1** A schematic representation of the procedure for preparing the HOPG electrodes with only the edge (HOPG-E) or basal plane (HOPG-P) carbon atoms accessible to electrolyte.

### 6.2.2 Electrochemical Oxidation of HOPG Edge and Plane Electrodes

To prepare the corresponding HOPG electrodes with oxygen-containing surface functionalities (designated as O<sub>x</sub>min-HOPG-E and O<sub>y</sub>min-HOPG-P), the newly prepared HOPG-E and HOPG-P electrodes were polarized at 1.8 V in 0.1 M phosphate-buffered saline solution (PBS, pH 6.5) for different time ( $x$  and  $y = 3, 10, 30$ min); they were then treated by cycling potential scanning in 0.5 M H<sub>2</sub>SO<sub>4</sub> until a stable cyclic voltammogram (CV) was recorded.

### 6.2.3 Structural and Electrochemical Characterization

Morphology and structure of the electrodes were characterized using scanning electron microscopy (SEM, JEOL JSM-7001F). X-ray photoelectron spectroscopic (XPS) measurements were made on a PHI Quantera SXM (ULVAC-PHI) using monochromatic Al K $\alpha$  radiation at a power of 100W (20kV, 5mA). Raman spectroscopy data were collected at room temperature using a Micro-Raman

spectrometer (Nikon) with 532 nm laser source.

Electrochemical measurements were performed using a BioLogic EC-Lab (VSP-300) with a three-electrode configuration. The as-prepared HOPG-E, HOPG-P, O<sub>3</sub>min-HOPG-E and O<sub>3</sub>min-HOPG-P electrodes were used as the working electrode, platinum wire as the counter electrode, and saturated calomel electrode (SCE) as the reference electrode. All potentials used were biased versus SCE. And all electrochemical experiments were performed in air at room temperature.

## 6.3 Results and Discussion

### 6.3.1 Characterizations

#### Morphological Characterizations

SEM has been done to characterize surface morphology of HOPG-P and HOPG-E with different oxidation time. Figure 3a shows that the original surface of HOPG sheet is smooth with a little wrinkles and edge planes. The HOPG has a structure of polycrystals, the size of which varies, the maximum being 10 mm for the highest quality. The basal plane surface of an HOPG electrode consists of layers of graphite which lie parallel to the surface and are separated from each other by 3.35 Å. [25] Surface defects occur in the form of edge plane steps exposing the edges of the graphite layers as illustrated in Figure 2. The distance between these defects can be no greater than the lateral grain size of the graphite sample, which in the case of HOPG is 1-10 mm (for the grade of HOPG used in this work). Thus, as the steps are multiples of 3.35 Å deep and typically range between 1-20 layers for HOPG, the total surface coverage of edge-plane graphite is rather small [26]. For example, McCreery and co-workers have shown via STM that the total coverage of edge-plane defects can be as low as 0.2% (cleavage with adhesive tape results in significantly more surface defects). [27]

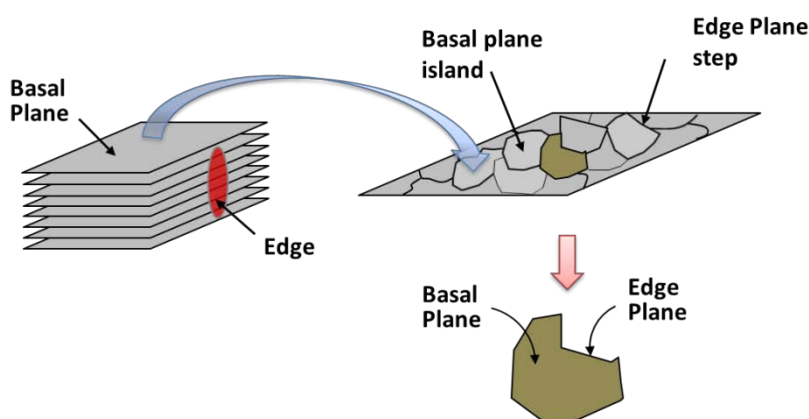


**Figure 2** Schematic diagrams showing the overhead view of a section of the basal plane HOPG surface.

As seen in Figure 3b, when electrochemical oxidation of the HOPG basal plane for 3 minutes (O<sub>3</sub>min-HOPG-P), a little structure defects caused by tiny blisters are observed around the step defects present

on the surface of HOPG indicating a preferential intercalation of the solvent in correspondence of sheet edges. It is known that blisters come from the intercalation of electrolyte and water into HOPG followed by subsurface gas evolution.[28] The intercalation process preferentially etches the step defects, grain boundaries and edge sites with weak van der Waals interactions and then yields gas production in correspondence of these sites. And some small size single layer or few layers graphene (several hundred nanometers) were exfoliated in the oxidized process, which was also proved by the Raman results in Figure 6. After a long time oxidation of 30 minutes, there is a significant change observed in the surface structure of HOPG (Figure 3c). Most of the surface was deeply exfoliated to big size graphene flakes. The gas formation process is so strong to deform the upper layers, which bend upward, and form a network of cracks. The blisters grow continuously upon explosion or gas release, and then collapse forming the network of ripples visible on the surface. And some curved single layer or few layers graphene with size bigger than 10 micrometers was found.

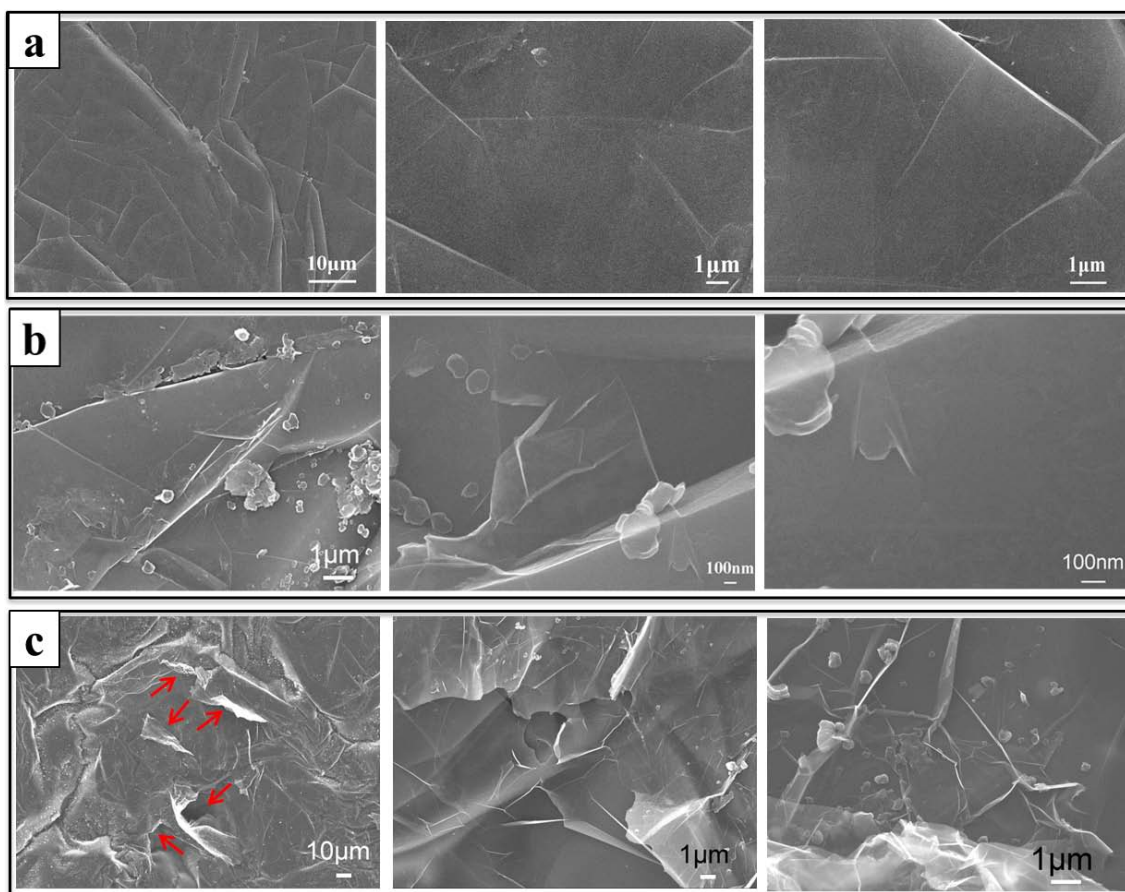


**Figure 3** SEMs of the surface of (a) HOPG-P, (b) O 3min-HOPG-P, and (c) O 30min-HOPG-P electrodes

SEMs of HOPG-E electrodes in different oxidation time (0, 3, 10, 30 min) were shown in Figure 4. As we can see in Figure 4a, most of the surface carbon exposed to the electrolyte is edge atom. In order to consider the repeatability of the HOPG-E electrodes, three electrodes (HOPG-E 01, HOPG-E 02 and HOPG-E 01-cut) were tested by CV method. The result was shown in Figure 5. CV curves of these three electrodes greatly coincident, which given a very good repeatability. So in this work, we assumed that the

surface of HOPG-E electrode all consist of edge carbon atoms.

Figure 4b -d shows SEM images of a typical exfoliation process as observed at different times on the same sample. The electrochemical exfoliation has two main effects: i) the exposed edge of HOPG sheet swells macroscopically, due to electrolyte intercalation and decomposition, producing gas and creating a highly expanded structure, and ii) exfoliated material is detached from the bulk solid due to the gas eruption, and dispersed in solution[29]. The exfoliation is effective enough to be easily visible by SEM even after a few minutes treatment (Figure 4b). The stacked graphite sheets swell due to visible gas formation and bubbling, yielding expanded structures that resemble open books; the foam like structure is instead observed (Figure 4d middle). The increase of sample volume can be relevant, creating highly expanded sheets that have a volume much larger than the original volume. Following the oxidation of HOPG-E electrode, the thickness of O-HOPG-E electrode was increased quickly, from original thickness of 100 $\mu\text{m}$  to 380 $\mu\text{m}$  of 30 minutes oxidation. When the oxidation time longer than one hour, a large amount of material released in solution and makes the solution dark.

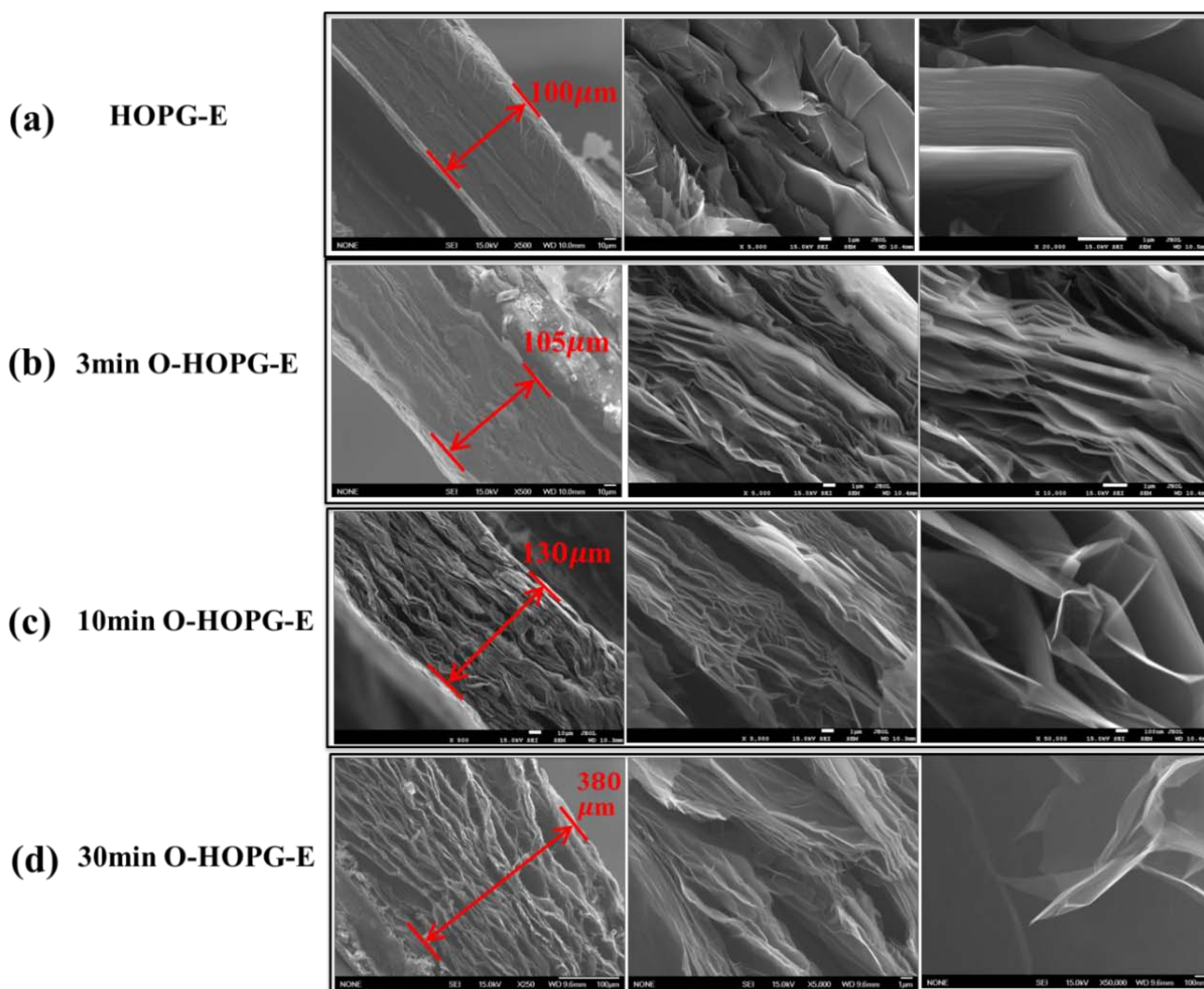


**Figure 4** SEMs of the surface of (a) HOPG-E, (b) O 3min-HOPG-E, (c) O 10min-HOPG-E, and (d) O 30min-HOPG-E electrodes

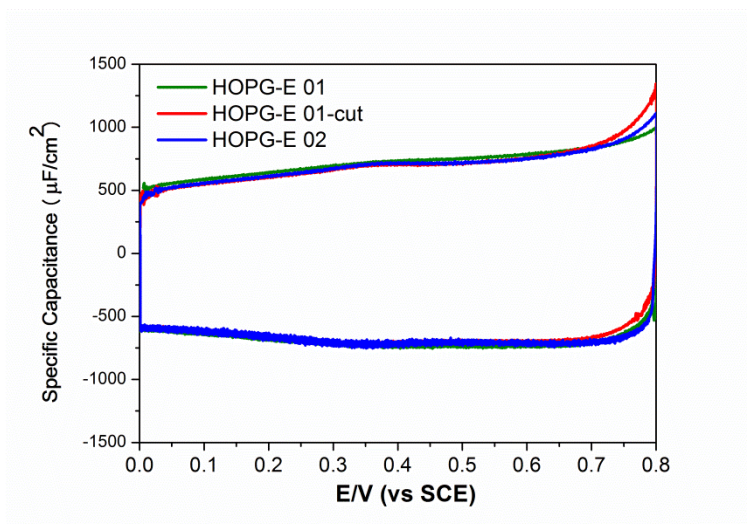


**Figure 5** Repeatability tests of HOPG-E electrode. CV curves were obtained at scan rate of 100mV/s in 0.5M H<sub>2</sub>SO<sub>4</sub> aqueous solution.

### Raman Characterizations

Raman spectroscopy is used to characterize the vibrational modes of molecules. Micro-Raman spectroscopy allows the probing of a small volume by combining a confocal microscope with the spectroscopy system [30]. The ability to collect Raman data from a very small area (350 nm in diameter) can in some situations reduce undesirable back-ground signals and enhance chemical sensitivity. Raman spectroscopy and imaging has been used as an effective tool for identifying the number of graphene layers. It can also use to probe structural and electronic characteristics of graphite materials, providing information on the defects (D band at  $\sim 1350\text{cm}^{-1}$ ), in-plane vibration of sp<sup>2</sup> carbon atoms (G band at  $\sim 1580\text{cm}^{-1}$ ) as well as the stacking order (2D band at  $\sim 2670\text{cm}^{-1}$ ) [31].

The Raman spectroscopy and imaging of HOPG-P and HOPG-E electrodes with different oxidation time are shown in Figure 6. In the imaging maps, the intensity of D, G and 2D bands are colored as purple, red and green, respectively. A typical Raman spectroscopy of HOPG is observed at  $1582.7\text{cm}^{-1}$  for G band and  $2725.1\text{cm}^{-1}$  for 2D band in Figure 6(1). Most of the surface of HOPG sheet has no defect, although a little D band at  $1582.7\text{cm}^{-1}$  appears, which may come from the edge-plane defect on the surface. After electrochemical oxidized for 3 minutes in 0.1M PBS, the imaging of the electrode surface undergoes a significant change in color, especially many green color areas appear which means the intensity of 2D band increase in these areas (Figure 6(2)). In the Micro Raman spectroscopies of points b and c, we can see some defects ( $I_D/I_G = 0.4$ ) were introduced into the surface along the “cracks”, indicating the edge-plane atoms are easy to oxidize. And the intensity ratio of  $I_{2D}/I_G \approx 5$  and  $\sim 20\text{cm}^{-1}$  blueshifted of the 2D band at point c, confirm the presence of some small single layer graphene. The Raman spectroscopy of basal plane of O 3min-HOPG-P electrode shows similar phenomena with HOPG-P, means that the basal plane atoms are not oxidized after short time reaction. In the situation of O 30min-HOPG-P electrode (Figure 6(3)), some defects

were introduced to the basal plane after the long time oxidation, with intensity ratio of  $I_D/I_G \approx 1$  and a big D' band ( $1613\text{ cm}^{-1}$ ) intensity was found which also indicating the defect. And many larger size single layer and few layers graphene with defect were observed because of electrochemical exfoliation. The Raman spectroscopies of HOPG-E electrodes with different oxidation time are shown in Figure 6(4). With the increase of oxidation time, the  $I_D/I_G$  intensity ratio increase from 0.07 for 3min-oxidation to 0.27 for 30min-oxidation. And a weak band at  $\sim 3246\text{ cm}^{-1}$  called 2D' band, is an overtone of D' ( $1613\text{ cm}^{-1}$ ) mode. In the electrochemical oxidation process, the introduction of oxygen containing groups rise defect band in Raman spectroscopy. Comparing the  $I_D/I_G$  intensity ratios of O-HOPG-P and O-HOPG-E electrodes, under the same oxidation time, the defect content in O-HOPG-P electrode is much larger than O-HOPG-E electrode. This maybe because of the oxidation and exfoliation effects work on the electrode surface at the same time. As the layered structure of HOPG-E electrode, the exfoliation effect is larger than oxidation effect for a while. But for HOPG-P electrode which only expose the basal plane surface out to the electrolyte, the intercalation of the ions and exfoliation of the gas are much harder than the layered sidewall, the oxidation reaction may happens easier than the exfoliation process.

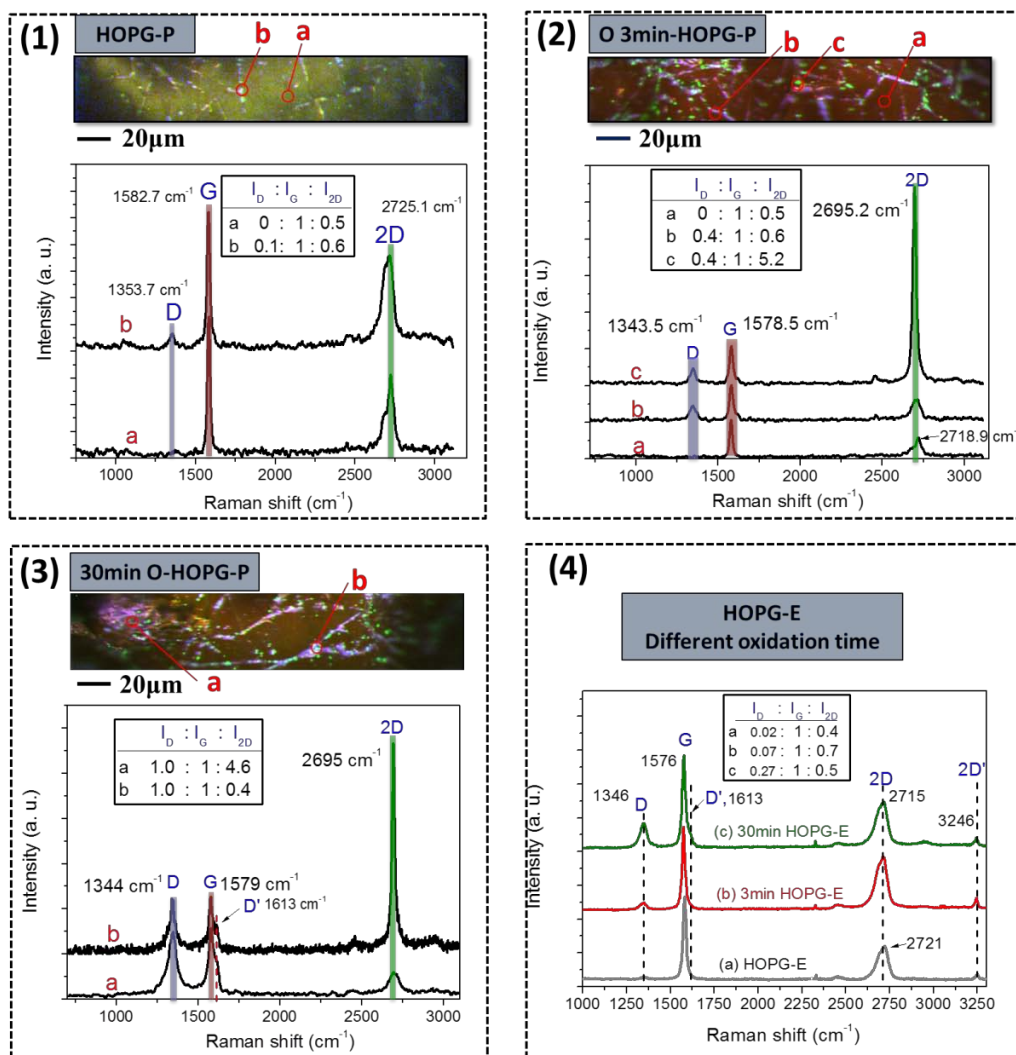


**Figure 6** Raman spectroscopy and imaging of 1) HOPG-P, 2) O 3min-HOPG-P, 3) O 30min-HOPG-P

electrodes and spectroscopy of 4) HOPG-E with different oxidation time.

XPS was applied to determine the elemental composition as well as chemical and electronic states of elements on the surface of the HOPG electrodes. The surface chemistry of modified electrodes is known to affect the electrochemical processes, for example adsorption or chelation effects arise from surface charge [32]. Figure 7 shows the wide spectra for O 30min-HOPG-P and O 30min-HOPG-E electrodes. Using the C1s and O1s signal intensities, the C: O ratios were calculated to be 19 and 32 for O 30min-HOPG-P and O 30min-HOPG-E electrode, respectively. This result consistent with our suspect in Raman experiments. That after 30 minutes electrochemical oxidation, the defect caused by introduction of oxygen groups on the HOPG-P electrode is much than the HOPG-E electrode.

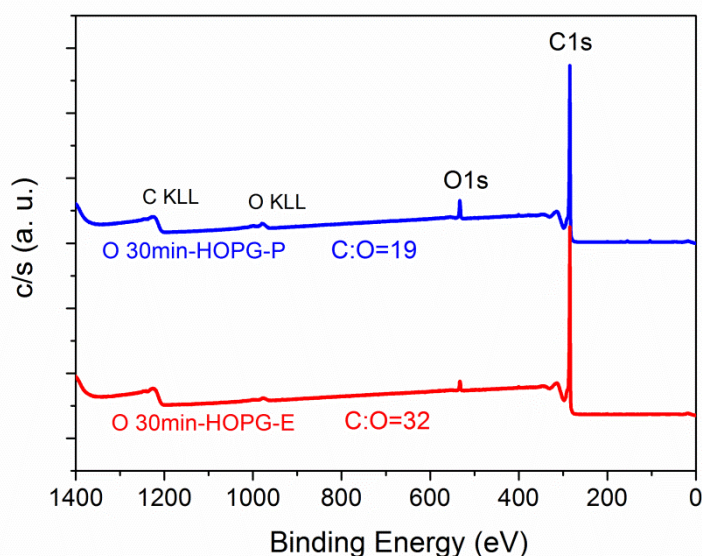


**Figure 7** The XPS wide spectra of O 30min-HOPG-P and O 30min-HOPG-E electrodes.

The high-resolution C1s and O1s XPS spectra of HOPG-P electrodes in different oxidation time are shown in Figure 8a and b, respectively. In C1s spectra, the peak at 284.5eV corresponds to the  $sp^2$  hybridized graphitic carbon and the peak at 291.0eV corresponds to the  $\pi-\pi^*$  structure. After oxidation for 3 min and 30min, there is no obvious change in C1s spectra for O-HOPG-P electrodes. In O1s spectra, the peak at 532.9eV to contributions from C–OH groups and the peak at 531.3eV to C=O and O=C–OH groups or some absorbed oxygen. After oxidation for 3min and 30min, the peak at 532.9eV for C–OH groups increase gradually, which means during the electrochemical oxidation, main chemical groups introduced to the surface of HOPG basal plane is hydroxyl groups. A broad band at 534 to 530 eV is observed at the original HOPG-P electrode without oxidation, which comes from the absorbed oxygen.

The high-resolution C1s and O1s XPS spectra of HOPG-E and O 30min-HOPG-E electrodes are shown in Figure 8c and d, respectively. In C1s spectra, compare with the original HOPG-E

electrode, it also has a peak at 285.4eV. The large full width at half maximum (FWHM) and the broad tail towards higher binding energy (286 to 289eV) in O 30min-HOPG-E electrode indicate that contributions of a variety of different carbon bonding configurations are superimposed. That can be fit to peaks at 286.2 and 287.0eV and thus assigned to C-OH, C=O species, respectively. The assignment of peaks in the O1s spectra for O 30min-HOPG-E is assign to the “carbon-oxygen” functional groups. Information provided by analysis of the O1s spectra can complement the information provided by analysis of C1s spectra. Because the O1s photoelectron kinetic energies are lower than those of the C1s, the O1s sampling depth is smaller, and therefore the O1s spectra are slightly more surface specific.[33] By reference to the C1s peak, we have assigned the O1s peaks at 531.3 and 530.6eV to contribution from C=O and O=C-OH groups, respectively, and that at 532.9 eV to C-OH groups. An interesting phenomena is noticed when compare spectra O1s of O 30min-HOPG-P and O 30min-HOPG-E electrodes, that the edge carbon atoms of graphite are more inclined to oxidized to carbon-oxygen double bond than basal plane atoms under the same electrochemical oxidation process.

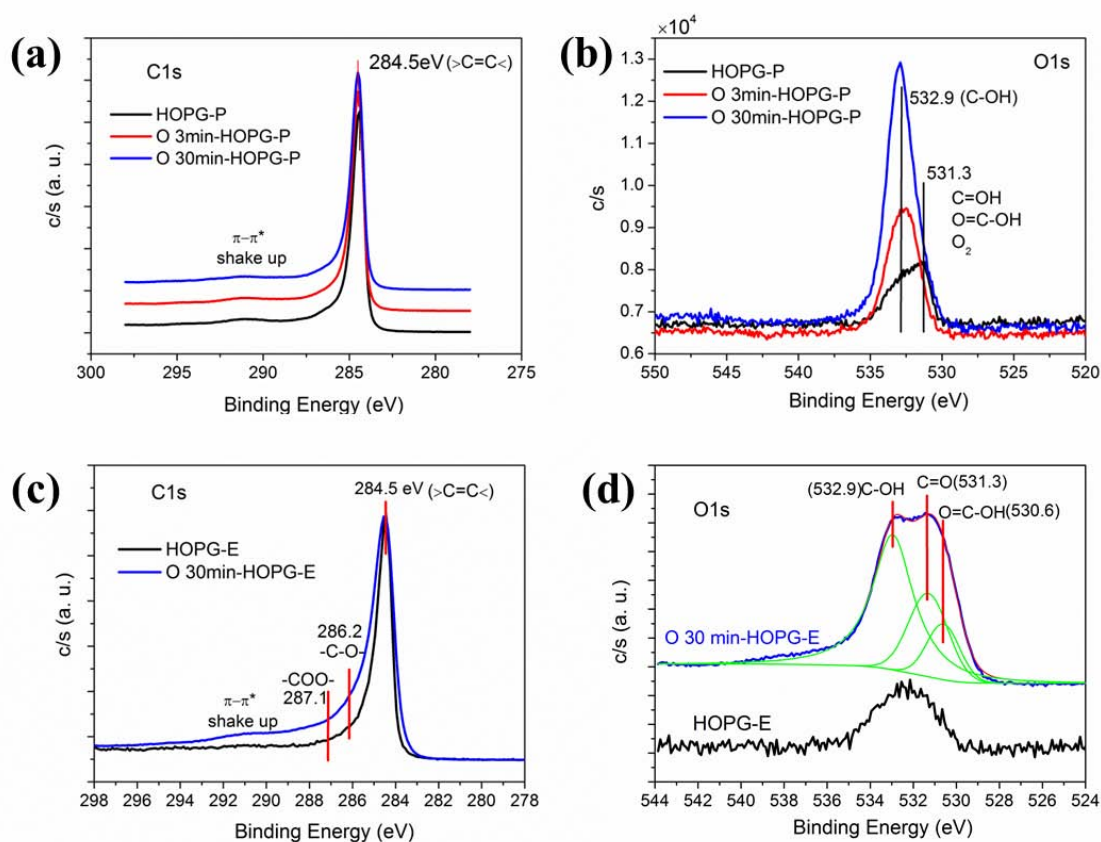


**Figure 8** XPS high resolution C1s spectra of HOPG-P (a), HOPG-E (b) and O1s spectra of HOPG-P (c), HOPG-E (d) with electrochemical oxidation for different time.

### 6.3.2 Edge and Basal Plane Effect of HOPG for Supercapacitor

After the confirmation of the successful electrochemical oxidation by Raman and X-ray photoelectron spectroscopic (XPS) measurements, these newly prepared and well-characterized HOPG-P and HOPG-E electrodes with and without the electrochemical oxidation were then used for subsequent electrochemical measurements. As only surface carbon atom (edge and basal plane) exposed to the electrolyte with all rest part of the carbon atom covered with PS in HOPG-P and HOPG-E electrodes, we assume that these electrodes can act as single layer or few layers graphene sheet to a certain extent. For study effect of carbon position (edge and basal plane) and oxidation state of graphene supercapacitor, a three electrodes system was used as shown in Figure 9.

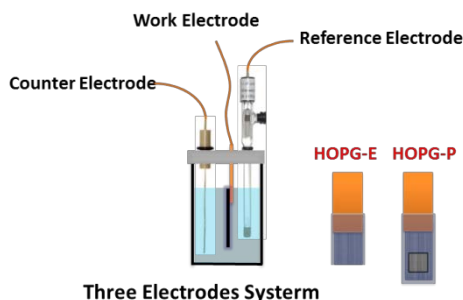


**Figure 9** Illustration of the three electrode system

Cyclic voltammetry (CV) curves were acquired at scanning rate from  $100 \text{ mV s}^{-1}$  and galvanostatic charge/discharge curves were obtained at constant current density in the potential range of 0 to 0.8V in 0.5 M  $\text{H}_2\text{SO}_4$  electrolyte. The specific capacitance  $C_{\text{sp}}$ , was calculated from galvanostatic charge/discharge curves according to

$$C_{\text{sp}} = \frac{I}{S \left( \frac{dV}{dt} \right)}$$

where  $dV/dt$  is calculated from the slope of the discharge curves,  $I$  is the charge/discharge current, and  $S$  is the surface area of the electrode (for HOPG-P electrode is about  $1.0 \text{ cm}^2$  and HOPG-E electrode is about  $0.01 \text{ cm}^2$ ).

The CV curves for the HOPG-P and HOPG-E electrodes at scan rate of  $100 \text{ mV s}^{-1}$  in the voltage range of 0-0.8V are shown in Figure 10(a). The CV curves have shown rectangular shapes, indicating excellent capacitive characteristics. And the HOPG-E electrode shows much larger specific capacitance than HOPG-P electrode (the area of the rectangular CV curves). Galvanostatic charge/discharge curves of HOPG-P and HOPG-E electrodes at a constant current density of  $10 \mu\text{A}/\text{cm}^2$  in the potential range between 0 and 0.8V are all shown in Figure 10(b). It can be seen that the curves are linear and symmetrical, showing typical and characteristic capacitive behavior. Only a very small voltage drop was observed, indicating that the electrodes had low internal resistance. In addition, the charge discharge duration for HOPG-E electrode was much longer than that for HOPG-P electrode, indicating a higher specific capacitance. The specific capacitance obtained from galvanostatic charge/discharge curves for HOPG-P is  $14 \mu\text{F}/\text{cm}^2$ , and for HOPG-E

is  $722 \mu\text{F}/\text{cm}^2$ , which is more than 50 folds larger than HOPG-P electrode. This result indicating that the graphene edge carbon atoms have more ability for absorption of electrolyte ions than basal plane atoms. The stack capacitance calculated from galvanostatic curves as a function of the charge/discharge current density of HOPG-P and HOPG-E are shown in Figure 10(c) and (d). The HOPG-E electrode shows good stack capacitance performance with almost no decay when the current density increasing. While the specific capacitance of HOPG-P electrode decrease by 20% when the current density increases from 1 to  $10 \mu\text{A}/\text{cm}^2$ . This is because the electron transfer at HOPG-E electrode surface could be better facilitated by the more active edge atoms than by the stable basal carbon atoms of HOPG-P electrode. Furthermore, the galvanostatic charge/discharge curves on HOPG-E electrode shows linear and symmetrical curves, but HOPG-P electrode gives bending curves. This because the perpendicular graphene layered structure of HOPG-E electrode has better conductivity because of the horizontal transfer of electrons align the graphene sheets than the HOPG-P electrode, in which electrons need to transfer vertically.

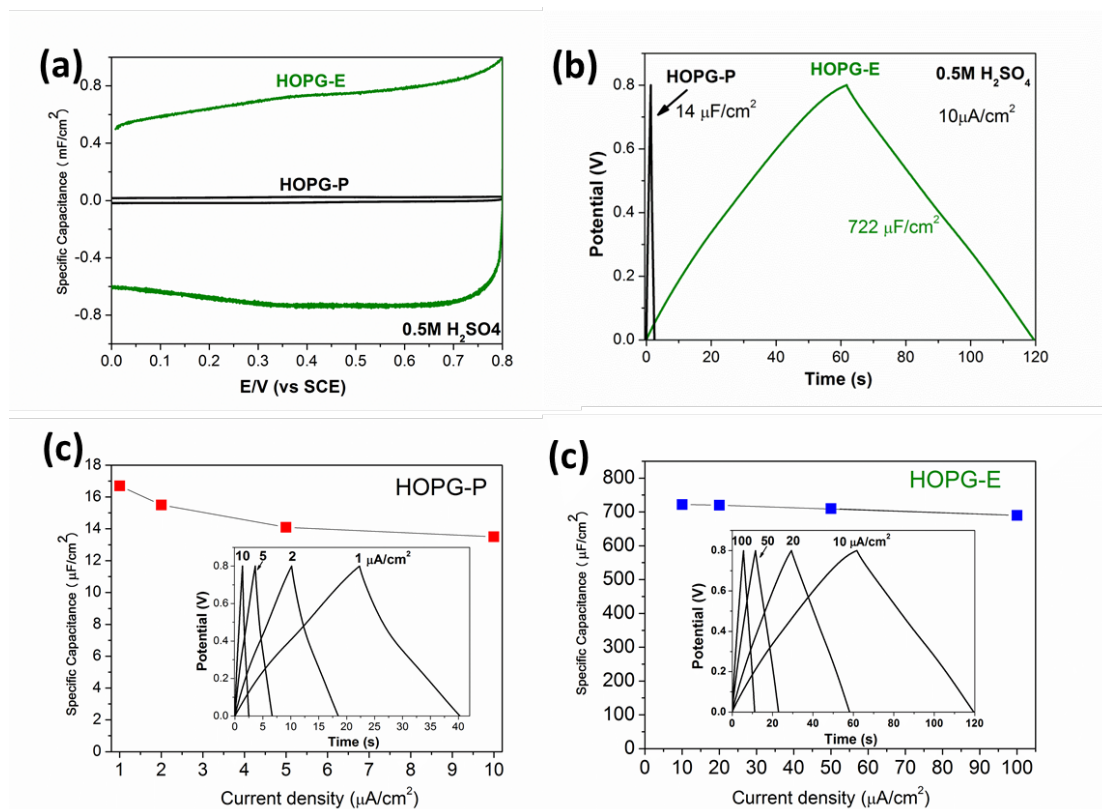


**Figure 10** Comparison of supercapacitor performance for HOPG-P and HOPG-E electrodes. (a) CV curves at scan rate of  $100 \text{ mV s}^{-1}$  and (b) Galvanostatic charge/discharge curves operated at current density of  $10 \mu\text{A}/\text{cm}^2$ , in the potential ranges of 0 to 0.8V in 0.5 M H<sub>2</sub>SO<sub>4</sub> electrolyte for HOPG-P (black line) and HOPG-E (green line) electrodes. Stack capacitance calculated from galvanostatic curves as a function of the charge /discharge current density of HOPG-P (c) and HOPG-E (d). (Inset is galvanostatic charge/discharge curves for electrodes operated under different current density).

In order to research the effect of oxidation in graphene based capacitor, the HOPG-P and HOPG-E electrodes with electrochemical oxidation of different time were used to consider the capacitor. Figure 11 (a)

shows the CV curves of O-HOPG-P electrodes with different oxidation time (0, 3, 10 and 30min) at scan rate of  $100 \text{ mV s}^{-1}$ . As the oxidation time increase, there is an obvious redox peak observed at about 0.3V with the reduction peak bigger than oxidation peak. This peak comes from the reduction of oxygen groups introduced to the basal plane during the electrochemical oxidation process, which mainly is hydroxyl group (From Raman and XPS results). In galvanostatic charge/discharge curves (Figure 11(b)), we can see that when oxidation time increase the discharging curves become non-lined, and also a big pseudo-capacitance appears. And the conductivity of the O-HOPG-P electrodes reduced seriously. The specific capacitances obtained from galvanostatic charge/discharge curves for O-HOPG-P are 14, 72, 149 and  $309 \mu\text{F}/\text{cm}^2$  for oxidation time of 0, 3, 10 and 30min, respectively. The increase of the capacitance is mainly contributes to the introduction of pseudo-capacitance. In the case of O-HOPG-E electrodes, we can see that after 10 minutes oxidation there is still only a small redox peak in CV curve (Figure 11(c)). And the galvanostatic charge /discharge curve remains linearly and symmetrically, which indicating that only a little oxygen introduced to the structure (In accordance with the Raman and XPS results). As we obtained from the HOPG-P and HOPG-E without oxidation, the specific capacitance of edge carbon atoms is more than 50 times larger than the basal plane atoms. So the increasing capacitance for O-HOPG-E electrodes is because of not only the increase of the total specific surface area, but also more edge atoms exposed to the electrolyte after electro-exfoliation of the HOPG sidewall stack.

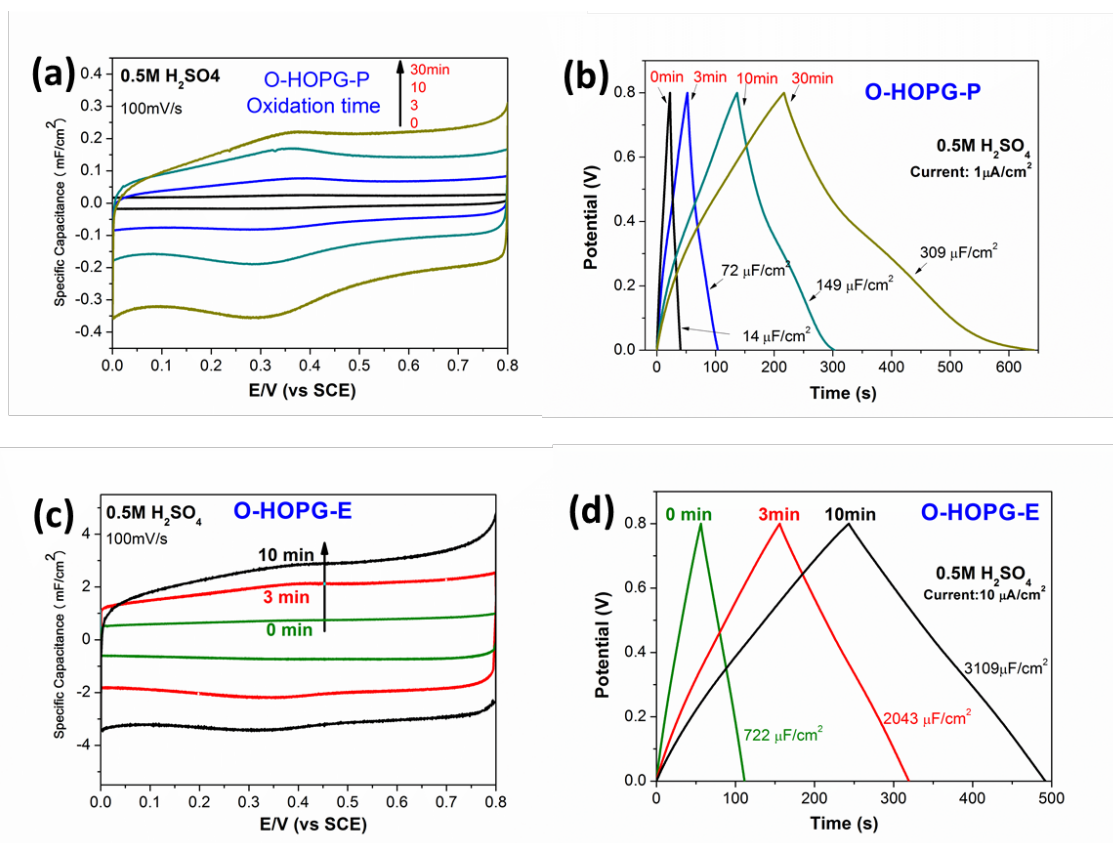


**Figure 11** Comparison of supercapacitor performance for HOPG-P and HOPG-E electrodes with electrochemical oxidation of different time. (a) CV curves at scan rate of  $100 \text{ mV s}^{-1}$  and (b) Galvanostatic charge/discharge curves operated at current density of  $1 \mu\text{A}/\text{cm}^2$ , in the potential ranges of 0 to 0.8V in 0.5

M H<sub>2</sub>SO<sub>4</sub> electrolyte for O-HOPG-P electrodes with oxidation time (0, 3, 10 and 30min); (c) and (d) are CV and galvanostatic charge/discharge curves of O-HOPG-E electrodes with electrochemical oxidation of different time under same condition.

### 6.3.3 Edge and Basal Plane Effect of HOPG for Biosensing

Over the past twenty years the popularity of nano, micro-carbon for example carbon fiber, carbon nanotubes and graphene as electrode material has increased dramatically.[34, 35] The fact that these different types of carbon materials are commercially available has led to their use in a wide range of applications.[36] However, despite the large amount of research conducted with carbon electrodes, there still remains uncertainty about the individual roles of the edge and basal-plane regions in the electrochemical response of a graphite surface. Herein, various electrochemical probes, including K<sub>3</sub> [Fe(CN)<sub>6</sub>], uric acid (UA) and ascorbic acid (AA) used to monitor the electrochemical activities of the basal plane and edge atoms.

#### Sensitive to both carbon position and oxidation state

##### Electrochemical activity of K<sub>3</sub> [Fe(CN)<sub>6</sub>] probe

Figure 12 shows the cyclic voltammograms of 5 mM potassium ferricyanide (K<sub>3</sub> [Fe(CN)<sub>6</sub>]) at the HOPG-P and HOPG-E electrodes with different oxidation time. As can be seen in Figure 12(a), the electrochemical oxidation caused some changes in the peak-to-peak separation for the O-HOPG-P electrodes ( $\Delta E_p \approx 690\text{mV}$  for HOPG-P and  $\Delta E_p \approx 280\text{mV}$  for O 30min-HOPG-P), indicating that the electron-transfer kinetics is sensitive to the oxygen-containing species. In the meanwhile, different  $\Delta E_p$  values were observed for the O 3min-HOPG-E (60 mV) and unoxidized (90 mV) electrodes under the same conditions (Figure 12(b)). The observed decrease in  $\Delta E_p$  by 30 mV indicates an enhanced electron-transfer rate for the oxidized HOPG-E electrode. Furthermore, the  $\Delta E_p$  for the electrochemically oxidized HOPG-E electrode is close to 59 mV over the whole range of scan rates from 10 up to 200 mV/s (Figure 13(a)); this indicates an almost ideal Nernst system with diffusion control (in Figure 13(b)).[37]

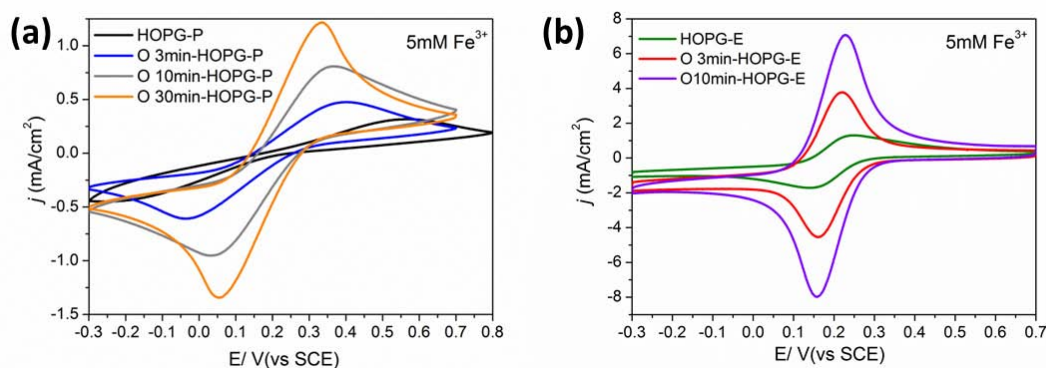


**Figure 12** Cyclic voltammograms of 5 mM K<sub>3</sub> [Fe(CN)<sub>6</sub>] recorded in 0.1 m PBS (pH 6.5) at a scan rate of 100 mV/s for the HOPG-P (a) and HOPG-E (b) electrodes with different oxidation time.

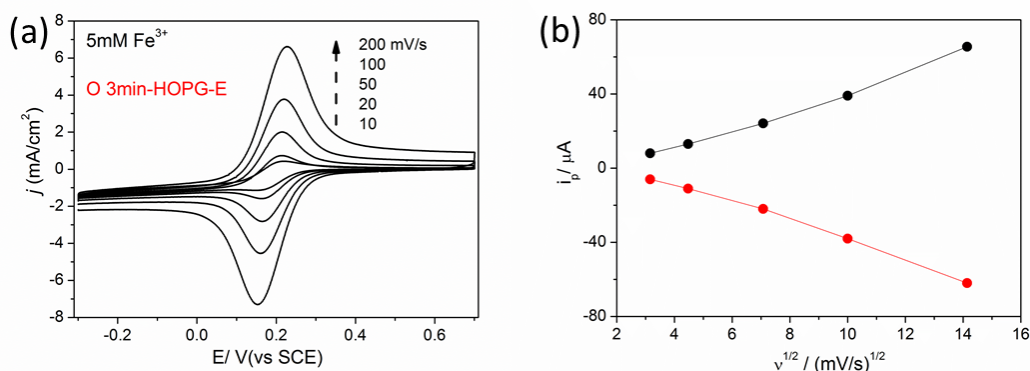


**Figure 13** (a) Cyclic voltammograms of 5 mM K<sub>3</sub>[Fe(CN)<sub>6</sub>] recorded in 0.1 M PBS (pH 6.5) at scan rates of 10, 20, 50, 100 to 200 500 mV/s (from inner to outer), (b) shows the plot of peak current as a function of the square root of the scan rate.

A summary of the oxidation and reduction peak potentials and currents of O-HOPG-P and O-HOPG-E electrodes with different oxidation time is shown in Table 1. The overall smaller values of  $\Delta E_p$  observed for the HOPG-E and O-HOPG-E electrodes with respect to the HOPG-P and O-HOPG-P electrodes imply much faster electron-transfer kinetics at the edge in this case. This is because the electron transfer at HOPG-E electrodes could be better facilitated by the edge end than the basal plane. Furthermore, the perpendicularly layered blocks, in which all the edge atoms are on one plane at the interface between the electrode and electrolyte solution, should provide additional advantages for the edge-bound oxygen-containing functionalities to collectively adsorb the electrochemical probe molecules and/or to increase their hydration degree for an enhanced electron-transfer rate at the O-HOPG-E electrode (Figure 12(b)). And the peak current of Fe<sup>3+</sup> on the O-HOPG-E electrodes increase significantly, this because the exfoliation of electrode surface could be exposed more edge atoms as reactive sites.

	E <sub>pa</sub> (V)	I <sub>pa</sub> (mA/cm <sup>2</sup> )	E <sub>pc</sub> (V)	I <sub>pc</sub> (mA/cm <sup>2</sup> )	$\Delta E = E_{pa} - E_{pc}$ (mV)
HOPG-P	0.54	0.18	-0.15	0.07	690
O 3min-HOPG-P	0.38	0.41	-0.03	0.37	410
O- 30min-HOPG-P	0.33	1.08	0.05	0.85	280
HOPG-E	0.24	1.4	0.15	1.3	90
O 3min--HOPG-E	0.22	3.7	0.16	3.3	60
O 10min-HOPG-E	0.23	6.9	0.16	6.6	60

**Table 1** Summary of the oxidation and reduction peak potentials and currents of O-HOPG-P and O-HOPG-E electrodes with different oxidation time in cyclic voltammograms of 5 mM K<sub>3</sub>[Fe(CN)<sub>6</sub>].

#### Electrochemical activity of uric acid (UA) molecular

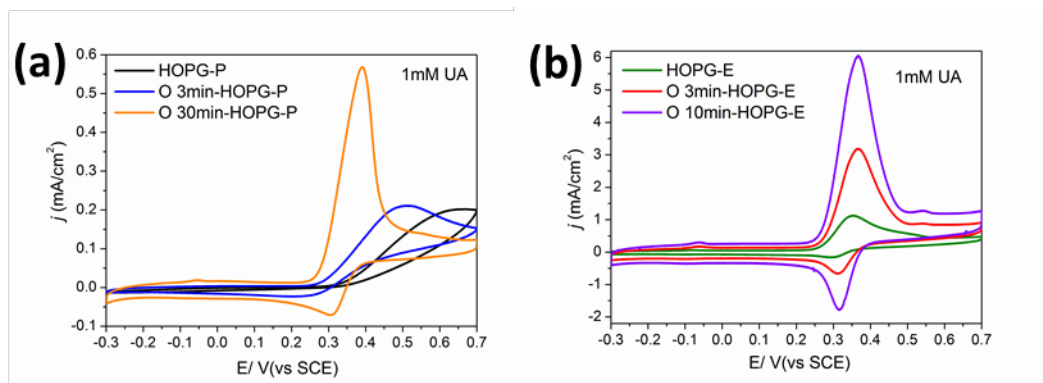


**Figure 14** Cyclic voltammograms of 1mM UA recorded in 0.1 m PBS (pH 6.5) at a scan rate of 100 mV/s of the HOPG-P (a) and HOPG-E (b) electrodes with different oxidation time.

Figure 14 shows the cyclic voltammograms of 1mM potassium UA at the HOPG-P and HOPG-E electrodes with different oxidation time. As can be seen in Figure 14(a), the electrochemical oxidation caused changes obviously in the peak-to-peak separation for the O-HOPG-P electrodes (No obvious peak at HOPG-P and  $\Delta E_p \approx 80\text{mV}$  for O 30min-HOPG-P, which is close to the idea potential difference of 59mV), indicating that the electron-transfer kinetics is sensitive to the oxygen-containing species. In contrast, a constant  $\Delta E_p$  values of 60mV was observed for the O-HOPG-E and unoxidized electrodes under the same conditions (Figure 14(b)).

A summary of the oxidation and reduction peak potentials and currents of O-HOPG-P and O-HOPG-E electrodes with different oxidation time for CV detection of UA is shown in Table 2. A dramatically  $\Delta E_p$  change at O-HOPG-E electrode was observed from 210mV for 3min oxidation to 80mV for 30min oxidation, which is more significant than the result in the above case of  $\text{K}_3[\text{Fe}(\text{CN})_6]$ . This maybe because of the oxygen and nitrogen groups in the structure of UA molecular could be interact with the oxygen groups (especially hydroxyl group) introduced to HOPG basal plane, which is further catalyst the redox and enhance the electron-transfer rate reaction of UA.

	$E_{pa}$ (V)	$I_{pa}$ (mA/cm <sup>2</sup> )	$E_{pc}$ (V)	$I_{pc}$ (mA/cm <sup>2</sup> )	$\Delta E = E_{pa} - E_{pc}$ (mV)
HOPG-P	0.57	0.25	N	N	-
O 3min-HOPG-P	0.48	0.62	0.27	-0.2	210
O- 30min-HOPG-P	0.39	2.59	0.31	-0.51	80
HOPG-E	0.36	0.94	0.30	-0.15	60
O 3min--HOPG-E	0.36	2.82	0.30	-0.48	60
O 10min-HOPG-E	0.37	5.82	0.31	-1.44	60

N: No obvious peak

**Table 2** Summary of the oxidation and reduction peak potentials and currents at O-HOPG-P and O-HOPG-E electrodes with different oxidation time for cyclic voltammograms of UA.

### Sensitive to carbon position but not oxidation state

### Electrochemical activity of ascorbic acid (AA) molecular

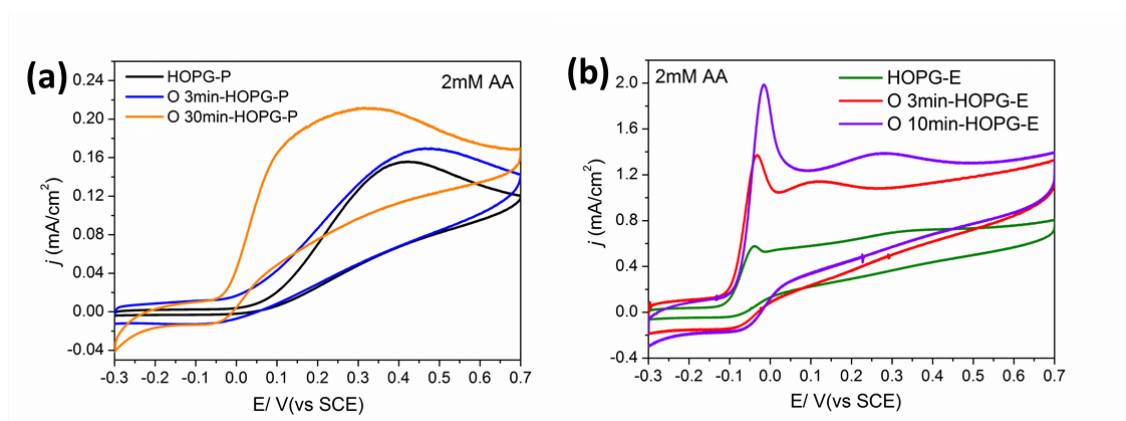


**Figure 15** Cyclic voltammograms of 2mM AA recorded in 0.1 m PBS (pH 6.5) at a scan rate of 100mV/s of the HOPG-P (a) and HOPG-E (b) electrodes with different oxidation time.

Figure 15 shows the typical voltammograms of 2.0 mM ascorbic acid (AA) in 0.1 m PBS electrolyte (pH 6.5) at the HOPG-P, HOPG-E electrodes with and without oxidation. In the case of O 3min-HOPG-E and O 30min-HOPG-E electrodes, the oxidation potential has no change, with oxidation peak current increase because of the exfoliation effect. In the O 3min-HOPG-P and O 30min-HOPG-P electrodes, there is also no change in oxidation potential. Together with the very different  $E_{p,a}$  values for the AA oxidation observed at HOPG-P and HOPG-E electrodes suggest that the electron-transfer rate in this particular case varies significantly with the edge/basal carbon atoms position but not with the oxygen-containing groups.

## 6.4 Conclusions

Depending on the electrochemical species used we found that the HOPG basal plane and edge carbon atoms could play a different role in electrochemistry at the HOPG electrode. Furthermore, oxygen-containing surface functionalities induced by electrochemical oxidation, were also demonstrated to regulate electrochemical activities of the HOPG electrode.

Direct evidence is obtained by XPS that the edge carbon atoms of graphite are more inclined to be oxidized to carbon-oxygen double bond, nevertheless main chemical groups introduced to the surface of HOPG basal plane is hydroxyl groups during the electrochemical process. HOPG-E electrodes gave a high specific capacitance of  $722 \mu\text{F}/\text{cm}^2$  obtained from galvanostatic charge/discharge curves, which is more than 50 folds larger than HOPG-P electrodes. After electro-oxidation, a pseudo-capacitance introduced to the O-HOPG-P electrodes from the oxygen groups, which increase the specific capacitance but reduce the conductivity of HOPG-P electrodes.

This work also highlights the importance of the carbon position (edge and basal plane sites of HOPG) and oxygenated species in electroanalysis, where control of these factors has the potential to lead to the

development of enhanced analytical sensors. In the case of electro-analyse of  $\text{Fe}^{3+}$  and UA, the response signal were sensitive to both carbon position and oxidation state; and in the case of AA, the redox reaction is sensitive to only carbon position but not oxidation state.

Furthermore, as all graphite electrodes are made from essentially the same building blocks (graphene sheets) we can expand our conclusions to other carbon materials even nanomaterials such as graphene, carbon fibers, and even carbon nanotubes. These novel findings reported herein address the longstanding issue concerning the relative roles of the basal plane and edge to electrochemistry at HOPG, and should facilitate the design and development of novel graphene-based electrodes of practical significance, especially in the development of supercapacitor and biosensors.

## References

1. Huang X, Zeng ZY, Fan ZX, Liu JQ, Zhang H. Graphene-Based Electrodes. *Advanced Materials* 2012,24:5979-6004.
2. Shao YY, Wang J, Wu H, Liu J, Aksay IA, Lin YH. Graphene Based Electrochemical Sensors and Biosensors: A Review. *Electroanalysis* 2010,22:1027-1036.
3. Wang Y, Li Y, Tang L, Lu J, Li J. Application of graphene-modified electrode for selective detection of dopamine. *Electrochemistry Communications* 2009,11:889-892.
4. Fernández JA, Morishita T, Toyoda M, Inagaki M, Stoeckli F, Centeno TA. Performance of mesoporous carbons derived from poly(vinyl alcohol) in electrochemical capacitors. *Journal of Power Sources* 2008,175:675-679.
5. Izadi-Najafabadi A, Yasuda S, Kobashi K, Yamada T, Futaba DN, Hatori H, et al. Extracting the Full Potential of Single-Walled Carbon Nanotubes as Durable Supercapacitor Electrodes Operable at 4 V with High Power and Energy Density. *Advanced Materials* 2010,22:E235-E241.
6. Futaba DN, Hata K, Yamada T, Hiraoka T, Hayamizu Y, Kakudate Y, et al. Shape-engineerable and highly densely packed single-walled carbon nanotubes and their application as super-capacitor electrodes. *Nat Mater* 2006,5:987-994.
7. El-Kady MF, Strong V, Dubin S, Kaner RB. Laser Scribing of High-Performance and Flexible Graphene-Based Electrochemical Capacitors. *Science* 2012,335:1326-1330.
8. Gao W, Singh N, Song L, Liu Z, Reddy ALM, Ci LJ, et al. Direct laser writing of micro-supercapacitors on hydrated graphite oxide films. *Nature Nanotechnology* 2011,6:496-500.
9. Miller JR, Outlaw RA, Holloway BC. Graphene double-layer capacitor with ac line-filtering performance. *Science* 2010,329:1637-1639.
10. Merlet C, Rotenberg B, Madden PA, Taberna PL, Simon P, Gogotsi Y, et al. On the molecular origin of supercapacitance in nanoporous carbon electrodes. *Nature Materials* 2012,11:306-310.
11. Zhu YW, Murali S, Stoller MD, Ganesh KJ, Cai WW, Ferreira PJ, et al. Carbon-Based Supercapacitors Produced by Activation of Graphene. *Science* 2011,332:1537-1541.

12. Srivastava D, Brenner DW, Schall JD, Ausman KD, Yu M, Ruoff RS. Predictions of Enhanced Chemical Reactivity at Regions of Local Conformational Strain on Carbon Nanotubes. *Physical Chemistry B* 1999,103:4330-4337.
13. Tang L, Wang Y, Li Y, Feng H, Lu J, Li J. Preparation, Structure, and Electrochemical Properties of Reduced Graphene Sheet Films. *Advanced Functional Materials* 2009,19:2782-2789.
14. Wang Y, Shao YY, Matson DW, Li JH, Lin YH. Nitrogen-Doped Graphene and Its Application in Electrochemical Biosensing. *ACS Nano* 2010,4:1790-1798.
15. Shen H, Zhang LM, Liu M, Zhang ZJ. Biomedical Applications of Graphene. *Theranostics* 2012,2:283-294.
16. Wang Y, Li YM, Tang LH, Lu J, Li JH. Application of graphene-modified electrode for selective detection of dopamine. *Electrochemistry Communications* 2009,11:889-892.
17. Srivastava RK, Srivastava S, Narayanan TN, Mahlotra BD, Vajtai R, Ajayan PM, et al. Functionalized Multilayered Graphene Platform for Urea Sensor. *ACS Nano* 2012,6:168-175.
18. Xue T, Jiang S, Qu Y, Su Q, Cheng R, Dubin S, et al. Graphene-Supported Hemin as a Highly Active Biomimetic Oxidation Catalyst. *Angewandte Chemie International Edition* 2012,51:3822-3825.
19. Tang LH, Wang Y, Liu Y, Li JH. DNA-Directed Self-Assembly of Graphene Oxide with Applications to Ultrasensitive Oligonucleotide Assay. *ACS Nano* 2011,5:3817-3822.
20. Pumera M. Electrochemistry of graphene: new horizons for sensing and energy storage. *The Chemical Record* 2009,9:211-223.
21. Davies TJ, Hyde ME, Compton RG. Nanotrench Arrays Reveal Insight into Graphite Electrochemistry. *Angewandte Chemie* 2005,117:5251-5256.
22. Chou A, Bocking T, Singh NK, Gooding JJ. Demonstration of the importance of oxygenated species at the ends of carbon nanotubes for their favourable electrochemical properties. *Chemical Communications* 2005:842-844.
23. Ji XB, Banks CE, Crossley A, Compton RG. Oxygenated edge plane sites slow the electron transfer of the ferro-/ferricyanide redox couple at graphite electrodes. *Chemphyschem* 2006,7:1337-1344.
24. Khan MMI, Hague AMJ, Kim K. Electrochemical determination of uric acid in the presence of ascorbic acid on electrochemically reduced graphene oxide modified electrode. *Journal of Electroanalytical Chemistry* 2013,700:54-59.
25. Chang H, Bard AJ. Observation and characterization by scanning tunneling microscopy of structures generated by cleaving highly oriented pyrolytic graphite. *Langmuir* 1991,7:1143-1153.
26. Banks CE, Davies TJ, Wildgoose GG, Compton RG. Electrocatalysis at graphite and carbon nanotube modified electrodes: edge-plane sites and tube ends are the reactive sites. *Chemical Communications* 2005:829-841.
27. McDermott MT, McCreery RL. Scanning Tunneling Microscopy of Ordered Graphite and Glassy Carbon Surfaces: Electronic Control of Quinone Adsorption. *Langmuir* 1994,10:4307-4314.
28. Goss CA, Brumfield JC, Irene EA, Murray RW. Imaging the incipient electrochemical oxidation of highly oriented pyrolytic graphite. *Anal Chem* 1993,65:1378-1389.
29. Xia ZY, Pezzini S, Treossi E, Giambastiani G, Corticelli F, Morandi V, et al. The Exfoliation of Graphene in Liquids by Electrochemical, Chemical, and Sonication-Assisted Techniques: A Nanoscale Study. *Advanced Functional Materials* 2013,23:4684-4693.

30. Ewen Smith GD. Modern Raman spectroscopy- a practical approach; 2004.
31. Ni Z, Wang Y, Yu T, Shen Z. Raman spectroscopy and imaging of graphene. *Nano Research* 2008,1:273-291.
32. An Wong CH, Ambrosi A, Pumera M. Thermally reduced graphenes exhibiting a close relationship to amorphous carbon. *Nanoscale* 2012,4:4972-4977.
33. Yang D, Velamakanni A, Bozoklu G, Park S, Stoller M, Piner RD, et al. Chemical analysis of graphene oxide films after heat and chemical treatments by X-ray photoelectron and Micro-Raman spectroscopy. *Carbon* 2009,47:145-152.
34. Li X, Wei BQ. Supercapacitors based on nanostructured carbon. *Nano Energy* 2013,2:159-173.
35. McCreery RL. Advanced Carbon Electrode Materials for Molecular Electrochemistry. *Chemical Reviews* 2008,108:2646-2687.
36. Geim AK, Novoselov KS. The rise of graphene. *Nat Mater* 2007,6:183-191.
37. McCreery RL. In *Electroanalytical Chemistry*. In. Edited by Bard AJ. New York: Dekker; 1991. pp. 221-374.

---

## Chapter 7

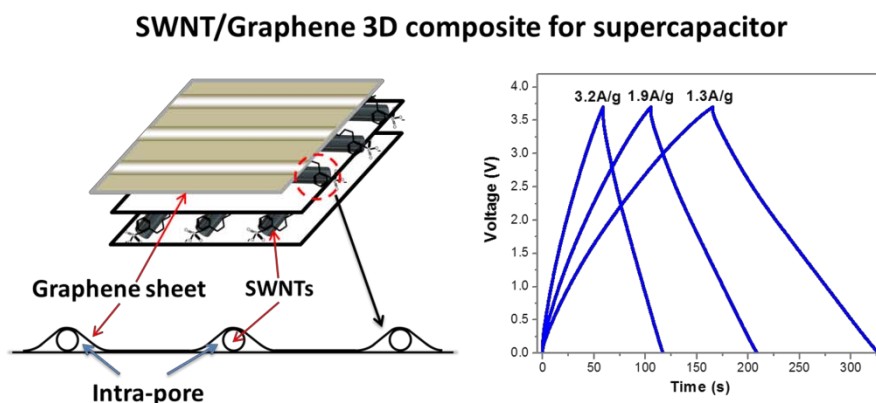
### Conclusions and Perspective

---

#### 7.1 Conclusions

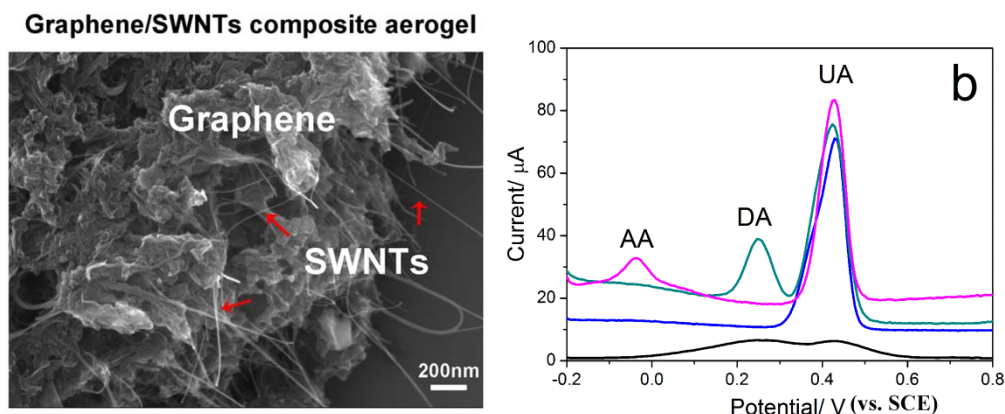
Due to the extraordinary physical, chemical, and electrochemical properties, graphene based materials with various micro-structure have proved to be promising electrodes materials for application in supercapacitor and biosensing.

#### Hybrid Graphene Electrodes for Supercapacitors of High Energy Density



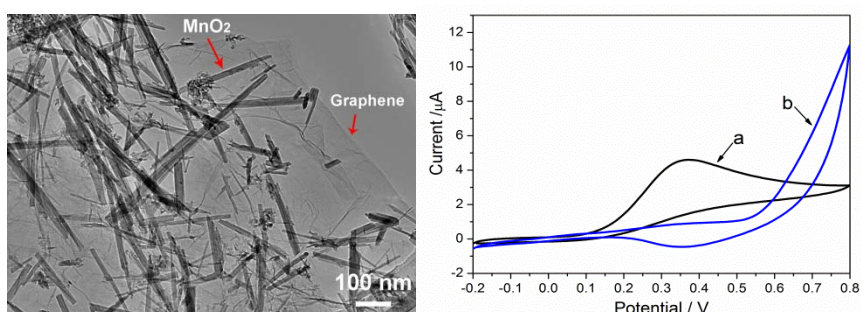
- (1) A process of co-reduction has been established and demonstrated to produce single-walled carbon nanotubes and graphene (SWNTs/graphene) composite with a three-dimensional network structure for applications in supercapacitors, with specific capacitance of  $261 \text{ F g}^{-1}$  and energy density of  $123 \text{ Wh kg}^{-1}$  in ionic liquid electrolyte (EMI-TFSI).
- (2) The composite electrode shown excellent cycling property with no decay in 5000 cycles.
- (3) Well dispersed SDBS modified SWNTs can be a “conductive spacer and binder” for the graphene electrode, which effectively prevent the restacking problem.
- (4) The introduction of SWNTs improving the resistance of chemical reduced graphene dramatically.

## Graphene-Carbon Nanotube Composite Aerogel for Selective Detection of Uric Acid



- (1) We have successfully fabricated a graphene and SWNTs hybrid structure (H-G/S composite) by a simple non-toxic hydrothermal process. A well-defined and interconnected three-dimensional porous network as obtained by freeze drying with SWNTs effectively inserted between the graphene layers.
- (2) The graphene/SWNTs composite modified electrode has been successfully utilized in the selective detection of uric acid (UA), eliminating the interference of ascorbic acid (AA) and dopamine (DA).
- (3) The composite modified electrode shows excellent linearity from 2.5 to 65  $\mu\text{M}$ , lower detection limit of 0.1  $\mu\text{M}$ , and sustaining stability for two weeks.

## Elimination of Ascorbic Acid and Sensitive Detection of Uric Acid at the $\text{MnO}_2$ Nanorods /Graphene-based Modified Electrode



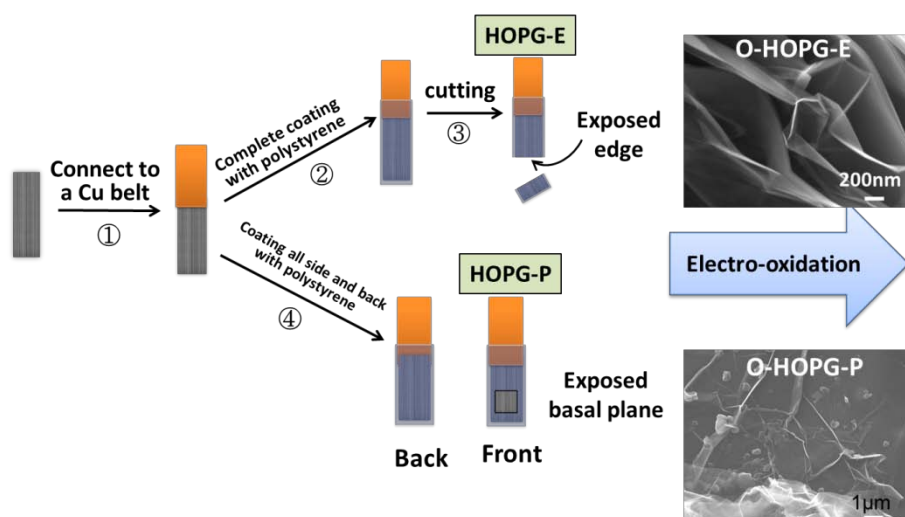
(Left) TEM image of  $\text{MnO}_2$ /graphene composite. (Right) Current responses at bare GCE (a) and  $\text{MnO}_2$  NR /GCE (b) in the presence of  $1 \times 10^{-3}$  M AA

- (1) The  $\alpha$ - $\text{MnO}_2$  nanorods ( $\text{MnO}_2$  NR) were first synthesized and then incorporated onto reduced graphene oxide (RGO) to get a composite ( $\text{MnO}_2$  NR/RGO) by aid of ultra-sonication.
- (2) A novel sensor ( $\text{MnO}_2$  NR /RGO/GCE) was fabricated, which takes advantage of the synergetic

effect from different nanomaterials;  $\text{MnO}_2$  nanorods can be as an eliminator of ascorbic acid, and ultra large surface area and good conductivity of RGO can provide more reactive sites for UA molecules and help to realize fast electron transfer, resulting in selective and sensitive detection of UA in the mass of ascorbic acid (AA).

- (3) The developed sensor has been applied to the selective determination of UA in human urine with good recovery (98.5-100.6%) and relative standard deviation ( $1.4 \pm 0.2\%$ ).

### Electrochemistry of HOPG Electrodes: Edge and Basal Plane Effect for Supercapacitor and Biosensing



- (1) The direct evidence is obtained by XPS that the edge carbon atoms of graphite are more inclined to be oxidized to carbon-oxygen double bond, nevertheless main chemical groups introduced to the surface of HOPG basal plane is hydroxyl groups during the electrochemical process.
- (2) HOPG-E electrodes gave a high specific capacitance of  $722 \mu\text{F}/\text{cm}^2$ , which is more than 50 folds larger than HOPG-P electrodes. After electro-oxidation, a pseudo-capacitance introduced to the O-HOPG-P electrodes from the oxygen groups, which increase the specific capacitance but reduce the conductivity of HOPG-P electrodes.
- (3) This work also highlights the importance of the carbon position (edge and basal plane sites of HOPG) and oxygenated species in electroanalysis, where control of these factors has the potential to lead to the development of enhanced analytical sensors. In the case of electro-analyze of  $\text{Fe}^{3+}$  and UA, the response signal were sensitive to both carbon position and oxidation state; and in the case of AA, the redox reaction is sensitive to only carbon position but not oxidation state.

## 7.2 Future Prospects

The future supercapacitors are expected to have the same level of energy density with lithium ion battery while remaining its high power density performance and cycling property. Although a high energy density and good cycling property are achieved in this work on graphene/SWNTs composite based supercapacitor, a relatively big  $IR_{\text{drop}}$  is still exists compare to commercial supercapacitor, which will influence the power density and big current charge-discharge performance greatly.

As described in Figure 7-1, ion diffusivity plays a key factor to realize compact supercapacitors with high energy density and high power density. For activated carbon, thicker electrodes possess higher ion diffusion barriers in the inner region of the electrode, resulting in higher internal resistance and inferior high-power performance. This factor limits the practical thickness of activated carbon electrodes. Because of their high surface area, excellent conductivity and crystallinity, a supergrowth aligned SWNTs electrode has been applied to binder free supercapacitors, achieving a power density about twice of activated carbon electrode with conductive agent and binder.[1] But until now, the high cost and catalysts impurities limit its application in actual device. Compare to carbon nanotubes (CNTs), graphene has extremely high specific surface area, excellent conductivity and graphene arrays (if possible) will have as high as CNTs of ion diffusion. As discussed in Chapter 6, electrochemical exfoliation of HOPG could be a candidate for easy preparation of graphene arrays (ECE-graphene). We believe that the ECE-graphene based electrode will increase the energy density and power density of supercapacitor further.

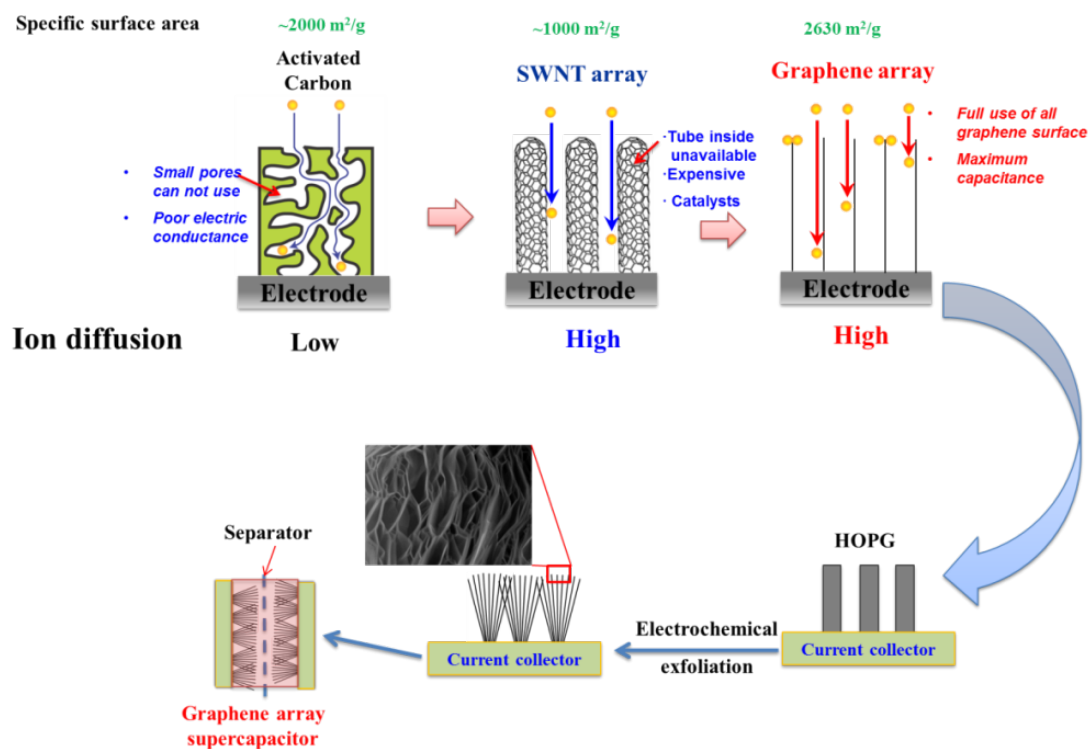


**Figure 7-1** The development of carbon based EDLC and fabrication of graphene array supercapacitors by electrochemical exfoliation.

1. Futaba DN, Hata K, Yamada T, Hiraoka T, Hayamizu Y, Kakudate Y, et al. Shape-engineerable and highly densely packed single-walled carbon nanotubes and their application as super-capacitor electrodes. *Nat Mater* 2006,5:987-994.

---

## Chapter 8

### Achievements

---

#### 8.1 List of Publications

- [1] Feifei Zhang, Jie Tang, Norio Shinya, Lu-Chang Qin, “Hybrid graphene electrodes for supercapacitors of high energy density”, *Chemical Physics Letters*, 584(2013) 124-129.
- [2] Feifei Zhang, Jie Tang, Zonghua Wang, Lu-Chang Qin, “Graphene–Carbon Nanotube Composite Aerogel for Selective Detection of Uric Acid”, *Chemical Physics Letters*, 590(2013) 121-125.
- [3] Feifei Zhang, Jie Tang, Norio Shinya, Lu-Chang Qin, “ The effect of defects and functional groups for graphene-based supercapacitors”, *Journal of Physical Chemistry C*, under review.
- [4] Zonghua Wang, Jie Tang, Feifei Zhang, Jianfei Xia, “Elimination of Ascorbic Acid and Sensitive Detection of Uric Acid at the MnO<sub>2</sub> Nanorods/Graphene-based Modified Electrode”, *Int. J. Electrochem. Sci.*, 8(2013) 9967-9976.
- [5] Guoyu Shi, Zonghua Wang, Jianfei Xia, Feifei Zhang, Jie Tang, “A Novel Architecture Intercalating Redox-Active Polymeric Groups within Graphene Frameworks to Host Platinum Nanoparticles for Methanol Oxidation”, *Int. J. Electrochem. Sci.*, 8(2013) 8764-8773.

#### 8.2 Award

2013 年 日中科学技術交流協会の「中国人留学生研究奨励賞」を受賞しました, 2013 年 12 月 20 日

#### 8.3 Patents

- [1] 唐捷、張菲菲、新谷紀雄、程騫、秦祿昌、「グラフェン電極フィルム、グラフェン電極フィルムの製造方法及びグラフェンキャパシター」、出願番号：PCT/JP2013/073841；出願日：2013 年 9 月 4 日
- [2] 唐捷、張菲菲、新谷紀雄、程騫、秦祿昌、「グラフェン積層電極フィルム、その製造方法及びグラフェンキャパシター」；出願番号：特願 2012-194833；出願日：2012 年 9 月 5 日
- [3] 唐捷、張菲菲、新谷紀雄、程騫、秦祿昌、「部分還元グラフェン階層体一連結体、その製造方法、そのに有粉末及びフィルム」；出願番号：特願 2012-194792；出願日：2012 年 9 月 5 日

[4] 唐捷、張菲菲、秦祿昌、「水熱生成グラフェン／CNT複合体エアロゲルの作成方法、水熱生成グラフェン／CNT複合体エアロゲル及びUA、DA、AA分離検出電極」；出願番号：特願2013-216801；出願日：2012年10月17日。

## 8.4 Oral Presentation

### Conference

[1] Feifei Zhang, Jie Tang, Zonghua Wang, Lu-Chang Qin. Graphene-based composite sensors for selective detection of biomolecules, *The 4<sup>th</sup> Annual Meeting of The Nanofiber Society of Japan*, 2013 July 5th, Tsukuba, Japan.

[2] Feifei Zhang, Jie Tang, Zonghua Wang, Lu-Chang Qin. Graphene-based composite sensors for selective detection of uric acid, dopamine and glucose, *The 2012 Materials Research Society (MRS) Fall Meeting*, November 26 - December 1, 2012, Boston, USA.

[3] Feifei Zhang, Jie Tang, Zonghua Wang, Lu-Chang Qin. Graphene/ Nano metal oxides composites sensors for selective detection of biomolecules, *2012 IUMRS International Conference on Electronic Materials*, September 23-28, 2012, Yokohama, Japan.

[4] Feifei Zhang, Jie Tang, Zonghua Wang, Lu-Chang Qin. Graphene/MnO<sub>2</sub> nanowire composite biosensors for selective detection of uric acid, *The 6th International Conference on the Science and Technology for Advanced Ceramics*, June 26-28, 2012, Yokohama, Japan.

[5] Feifei Zhang, Jie Tang, Zonghua Wang. A novel sensor of poly (vinyl alcohol) incorporated multiwalled carbon nanotube for voltammetric determination of Cu(II), *The 62<sup>nd</sup> Annual Meeting of the International Society of Electrochemistry*, September 11-16, 2011, Niigata, Japan.

## Acknowledgements

This thesis was accomplished under the supervision from my supervisor Professor Jie Tang. During the three years PH.D program, Prof. Tang has devoted to instructing to instructing my research and study from selecting the topic and designing the proposal to solving the problem and composing the thesis. Her expertise, innovation, and generosity has deeply affected me and greatly encouraged me for my study and life in Japan. Her scientific spirit is a model of virtue for my future career and life. It is my great honor to study and work in her group. Therefore, I am taking this opportunity to sincerely giving my millions of thanks to her.

I also like to give my great thanks to Professor Lu-Chang Qin from North Carolina University at Chapel Hill for his insight resolving many problems encountered throughout research and thesis writing, for his inspiring and encouraging way to guide me to a deeper understanding of research, and his invaluable comments during my graduate study.

Special thanks must be given to Dr. Han Zhang, Dr. Faxiang Qin and Dr. Jinshi Yuan for thesis warm support and encouragement on my doctoral study over the years. Their profound knowledge, professional skill, and modest character have deeply impressed me. It is my great pleasure to work and learn from them.

I really appreciate the valuable suggestion and assistance from all my group members: Mr. Yuexian Lin, Mr. Qingguo Shao, Mr. Soeda Daisuke, Mrs. Jing Li, and I would like to give my thanks to the secretaries of our group Mrs. Kawamura Yukiyo and Furusawa Sachiko for their kindly help during the study.

I am highly indebted to my committee members: Professor Yoshio Sakka; Professor Junichi Yanagisawa; Professor Kiyoto Matsuishi.

I would like to give my host sincere thanks and love to my parents, my husband and all friends who are always standing by me and backing my study abroad. I cannot image the life without their selfless love and support.

This work was performed at Materials Processing Unit, National Institute for Materials science and Graduate School of Pure and Applied Science of University of Tsukuba.